UC Berkeley

UC Berkeley Previously Published Works

Title

The DESI Experiment Part I: Science,Targeting, and Survey Design

Permalink

https://escholarship.org/uc/item/2nz5q3bt

Authors

Collaboration, DESI
Aghamousa, Amir
Aguilar, Jessica
et al.

Publication Date

2016-10-31

Peer reviewed

The DESI Experiment Part I: Science,Targeting, and Survey Design

DESI Collaboration: Amir Aghamousa[73], Jessica Aguilar[76], Steve Ahlen[85], Shadab Alam[41,59], Lori E. Allen[81], Carlos Allende Prieto[64], James Annis[52], Stephen Bailey[76], Christophe Balland[88], Otger Ballester[57], Charles Baltay[84], Lucas Beaufore[45], Chris Bebek[76], Timothy C. Beers[39], Eric F. Bell[28], Jos Luis Bernal[66], Robert Besuner[89], Florian Beutler[62], Chris Blake[15], Hannes Bleuler[50], Michael Blomqvist[2], Robert Blum[81], Adam S. Bolton[35,81], Cesar Briceno[18], David Brooks[33], Joel R. Brownstein[35], Elizabeth Buckley-Geer[52], Angela Burden[9], Etienne Burtin[12], Nicolas G. Busca[7], Robert N. Cahn[76], Yan-Chuan Cai[59], Laia Cardiel-Sas[57], Raymond G. Carlberg[23], Pierre-Henri Carton[12], Ricard Casas[56], Francisco J. Castander[56], Jorge L. Cervantes-Cota[11], Todd M. Claybaugh[76], Madeline Close[14], Carl T. Coker[26], Shaun Cole[60], Johan Comparat[67], Andrew P. Cooper[60], M.-C. Cousinou[4], Martin Crocce[56], Jean-Gabriel Cuby[2], Daniel P. Cunningham[1], Tamara M. Davis[86], Kyle S. Dawson[35], Axel de la Macorra[68], Juan De Vicente[19], Timothée Delubac[74], Mark Derwent[26], Arjun Dey[81], Govinda Dhungana[44], Zhejie Ding[31], Peter Doel[33], Yutong T. Duan[85], Anne Ealet[4], Jerry Edelstein[89], Sarah Eftekharzadeh[32], Daniel J. Eisenstein[53], Ann Elliott[45], Stéphanie Escoffier[4], Matthew Evatt[81], Parker Fagrelius[76], Xiaohui Fan[90], Kevin Fanning[48], Arya Farahi[40], Jay Farihi[33], Ginevra Favole[51,67], Yu Feng[47], Enrique Fernandez[57], Joseph R. Findlay[32], Douglas P. Finkbeiner[53], Michael J. Fitzpatrick[81], Brenna Flaugher[52], Samuel Flender[8], Andreu Font-Ribera[76], Jaime E. Forero-Romero[22], Pablo Fosalba[56], Carlos S. Frenk[60], Michele Fumagalli[16,60], Boris T. Gaensicke[49], Giuseppe Gallo[52], Juan Garcia-Bellido[67], Enrique Gaztanaga[56], Nicola Pietro Gentile Fusillo[49], Terry Gerard[29], Irena Gershkovich[48], Tommaso Giannantonio[70,78], Denis Gillet[50], Guillermo Gonzalez-de-Rivera[54], Violeta Gonzalez-Perez[62], Shelby Gott[81], Or Graur[6,38,53], Gaston Gutierrez[52], Julien Guy[88], Salman Habib[8], Henry Heetderks[89], Ian Heetderks[89], Katrin Heitmann[8], Wojciech A. Hellwing[60], David A. Herrera[81], Shirley Ho[41,47,76], Stephen Holland[76], Klaus Honscheid[26,45], Eric Huff[26], Eric Huff[45], Timothy A. Hutchinson[35], Dragan Huterer[48], Ho Seong Hwang[87], Joseph Maria Illa Laguna[57], Yuzo Ishikawa[89], Dianna Jacobs[76], Niall Jeffrey[33], Patrick Jelinsky[89], Elise Jennings[52], Linhua Jiang[69], Jorge Jimenez[57], Jennifer Johnson[26], Richard Joyce[81], Eric Jullo[2], Stéphanie Juneau[12,81], Sami Kama[44], Armin Karcher[76], Sonia Karkar[88], Robert Kehoe[44], Noble Kennamer[37], Stephen Kent[52], Martin Kilbinger[12], Alex G. Kim[76], David Kirkby[37], Theodore Kisner[76], Ellie Kitanidis[47], Jean-Paul Kneib[74], Sergey Koposov[61], Eve Kovacs[8], Kazuya Koyama[62], Anthony Kremin[48], Richard Kron[52], Luzius Kronig[50], Andrea Kueter-Young[34], Cedric G. Lacey[60], Robin Lafever[89], Ofer Lahav[33], Andrew Lambert[76], Michael Lampton[89], Martin Landriau[76], Dustin Lang[23], Tod R. Lauer[81], Jean-Marc Le Goff[12], Laurent Le Guillou[88], Auguste Le Van Suu[3], Jae Hyeon Lee[42], Su-Jeong Lee[45], Daniela Leitner[76], Michael Lesser[90], Michael E. Levi[76], Benjamin L'Huillier[73], Baojiu Li[60], Ming Liang[81], Huan Lin[52], Eric Linder[89], Sarah R. Loebman[28], Zarija Lukić[76], Jun Ma[72], Niall MacCrann[13,45], Christophe Magneville[12], Laleh Makarem[50], Marc Manera[17,33], Christopher J. Manser[49], Robert Marshall[81], Paul Martini[13,26], Richard Massey[16], Thomas Matheson[81], Jeremy McCauley[76], Patrick McDonald[76], Ian D. McGreer[90], Aaron Meisner[76], Nigel Metcalfe[60], Timothy N. Miller[76], Ramon Miquel[55,57], John Moustakas[34], Adam Myers[32], Milind Naik[76], Jeffrey A. Newman[30], Robert C. Nichol[62], Andrina Nicola[58], Luiz Nicolati da Costa[75,82], Jundan Nie[72], Gustavo Niz[21], Peder Norberg[16,60], Brian Nord[52], Dara Norman[81], Peter Nugent[27,76], Thomas O'Brien[26], Minji Oh[73,93], Knut A. G. Olsen[81], Cristobal Padilla[57], Hamsa Padmanabhan[58], Nikhil Padmanabhan[84], Nathalie Palanque-Delabrouille[12], Antonella Palmese[36], Daniel Pappalardo[26], Isabelle Pris[2], Changbom Park[87], Anna Patej[42,90], John A. Peacock[59], Hiranya V. Peiris[33], Xiyan Peng[72], Will J. Percival[62], Sandrine Perruchot[3], Matthew M. Pieri[2], Richard Pogge[26], Jennifer E. Pollack[62], Claire Poppett[89], Francisco Prada[63], Abhishek Prakash[30], Ronald G. Probst[81], David

Rabinowitz[84], Anand Raichoor[12,74], Chang Hee Ree[73], Alexandre Refregier[58], Xavier Regal[3], Beth Reid[76], Kevin Reil[71], Mehdi Rezaie[31], Constance M. Rockosi[24,92], Natalie Roe[76], Samuel Ronayette[3], Aaron Roodman[71], Ashley J. Ross[13,26], Nicholas P. Ross[59], Graziano Rossi[25], Eduardo Rozo[46], Vanina Ruhlmann-Kleider[12], Eli S. Rykoff[71], Cristiano Sabiu[73], Lado Samushia[43], Eusebio Sanchez[19], Javier Sanchez[37], David J. Schlegel[76], Michael Schneider[77], Michael Schubnell[48], Aurlia Secroun[4], Uros Seljak[47], Hee-Jong Seo[20], Santiago Serrano[56], Arman Shafieloo[73], Huanyuan Shan[74], Ray Sharples[14], Michael J. Sholl[5], William V. Shourt[89], Joseph H. Silber[76], David R. Silva[81], Martin M. Sirk[89], Anze Slosar[10], Alex Smith[60], George F. Smoot[47,76], Debopam Som[2], Yong-Seon Song[73], David Sprayberry[81], Ryan Staten[44], Andy Stefanik[52], Gregory Tarle[48], Suk Sien Tie[26], Jeremy L. Tinker[38], Rita Tojeiro[91], Francisco Valdes[81], Octavio Valenzuela[65], Monica Valluri[28], Mariana Vargas-Magana[68], Licia Verde[55,66], Alistair R. Walker[81], Jiali Wang[72], Yuting Wang[80], Benjamin A. Weaver[38], Curtis Weaverdyck[48], Risa H. Wechsler[71,83], David H. Weinberg[26], Martin White[47], Qian Yang[69,90], Christophe Yeche[12], Tianmeng Zhang[72], Gong-Bo Zhao[80], Yi Zheng[73], Xu Zhou[80], Zhimin Zhou[80], Yaling Zhu[89], Hu Zou[72], Ying Zu[13,79]

(Affiliations can be found after the references)

Abstract

DESI (Dark Energy Spectroscopic Instrument) is a Stage IV ground-based dark energy experiment that will study baryon acoustic oscillations (BAO) and the growth of structure through redshift-space distortions with a wide-area galaxy and quasar redshift survey. To trace the underlying dark matter distribution, spectroscopic targets will be selected in four classes from imaging data. We will measure luminous red galaxies up to $z = 1.0$. To probe the Universe out to even higher redshift, DESI will target bright [O II] emission line galaxies up to $z = 1.7$. Quasars will be targeted both as direct tracers of the underlying dark matter distribution and, at higher redshifts ($2.1 < z < 3.5$), for the Ly-α forest absorption features in their spectra, which will be used to trace the distribution of neutral hydrogen. When moonlight prevents efficient observations of the faint targets of the baseline survey, DESI will conduct a magnitude-limited Bright Galaxy Survey comprising approximately 10 million galaxies with a median $z \approx 0.2$. In total, more than 30 million galaxy and quasar redshifts will be obtained to measure the BAO feature and determine the matter power spectrum, including redshift space distortions.

Contents

1 Overview

DESI is a Stage IV ground-based dark energy experiment that will study baryon acoustic oscillations (BAO) and the growth of structure through redshift-space distortions (RSD) with a wide-area galaxy and quasar redshift survey. DESI is the successor to the successful Stage-III BOSS redshift survey and complements imaging surveys such as the Stage-III Dark Energy Survey (DES, operating 2013–2018) and the Stage-IV Large Synoptic Survey Telescope (LSST, planned start early in the next decade). DESI is an important component of the DOE Cosmic Frontier program, meeting the need for a wide-field spectroscopic survey identified in the 2011 "Rocky-III" dark energy community planning report. In addition to providing Stage IV constraints on dark energy, DESI will provide new measurements that can constrain theories of modified gravity and inflation, and that will measure the sum of neutrino masses.

The DESI instrument is a robotically-actuated, fiber-fed spectrograph capable of taking up to 5,000 simultaneous spectra over a wavelength range from 360 nm to 980 nm. The fibers feed ten three-arm spectrographs with resolution $R = \lambda/\Delta\lambda$ between 2000 and 5500, depending on wavelength. This powerful instrument will be installed at prime focus on the 4-m Mayall telescope in Kitt Peak, Arizona, along with a new optical corrector, which will provide a three-degree diameter field of view. The DESI collaboration will also deliver a spectroscopic pipeline and data management system to reduce and archive all data for eventual public use.

The DESI instrument will be used to conduct a five-year survey designed to cover 14,000 deg^2. To trace the underlying dark matter distribution, spectroscopic targets will be selected in four classes from imaging data. We will measure luminous red galaxies (LRGs) up to $z = 1.0$, extending the BOSS LRG survey in both redshift and survey area. To probe the Universe out to even higher redshift, DESI will target bright [O II] emission line galaxies (ELGs) up to $z = 1.7$. Quasars will be targeted both as direct tracers of the underlying dark matter distribution and, at higher redshifts ($2.1 < z < 3.5$), for the Ly-α forest absorption features in their spectra, which will be used to trace the distribution of neutral hydrogen. When moonlight prevents efficient observations of the faint targets of the baseline survey, DESI will conduct a magnitude-limited Bright Galaxy Survey (BGS) comprising approximately 10 million galaxies with a median $z \approx 0.2$. In total, more than 30 million galaxy and quasar redshifts will be obtained to measure the BAO feature and determine the matter power spectrum, including redshift space distortions.

In the following document, we primarily refer to this baseline survey, which would span 14,000 deg^2. We also calculate numbers for a minimum survey spanning 9,000 deg^2, which is still sufficient to meet the requirements of a Stage-IV project.

DESI provides at least an order of magnitude improvement over BOSS both in the comoving volume it probes and the number of galaxies it will map. This will significantly advance our understanding of the expansion history of the Universe, providing more than thirty sub-percent-accuracy distance measurements. Precision on the expansion history of the Universe is a powerful probe of the nature of dark energy. This can be quantified with the Dark Energy Task Force figure of merit (DETF FoM), which measures the combined precision on the dark energy equation of state today, w_0, and its evolution with redshift w_a. DESI galaxy BAO measurements achieve a DETF FoM of 133, more than a factor of three better than the DETF FoM of all Stage-III galaxy BAO measurements combined. The FoM increases to 169 with the inclusion of Ly-α forest BAO, and 332 including galaxy broadband power spectrum to $k = 0.1\ h\,\mathrm{Mpc}^{-1}$. DESI clearly satisfies the DETF criteria for a Stage-IV experiment. Moreover, the FoM grows to 704 when the galaxy broadband power spectrum data out to $k < 0.2\ h\,\mathrm{Mpc}^{-1}$ are included.

In addition, DESI will measure the sum of neutrino masses with an uncertainty of 0.020 eV (for $k_{\max} < 0.2\ h\,\mathrm{Mpc}^{-1}$), sufficient to make the first direct detection of the sum of the neutrino masses

at 3-σ significance and rule out the the inverted mass hierarchy at 99% CL, if the hierarchy is normal and the masses are minimal. DESI will also place significant constraints on theories of modified gravity and of inflation by measuring the spectral index n_s and its running with wavenumber, α_s. The BGS will enable the best ever measurements of low redshift BAO and RSD, including the use of multiple-tracer methods that exploit galaxy populations with different clustering properties, and it will yield novel tests of modified gravity theories using the velocity fields of cluster infall regions. Because the nearby galaxies of the BGS are too clustered to fill all of the targets, in parallel with the BGS, DESI will conduct a survey of Milky Way stars, that can be used to trace the dark matter halo of the Milky Way and probe the small-scale structure of ΛCDM.

DESI will provide an unprecedented multi-object spectroscopic capability for the U.S. through an existing NSF telescope facility. Many other science objectives can be addressed with the DESI wide field survey dataset and through bright time and piggy-back observation programs. Much as with SDSS, a rich variety of projects will flow from the legacy data from the DESI survey.

DESI will overlap with the DES and LSST survey areas, which are primarily in the Southern hemisphere but which will have equatorial and northern ecliptic regions. DESI will be a pathfinder instrument for the massive spectroscopic follow-up required for future large area imaging surveys such as LSST.

This portion of the Final Design Report summarizes the DESI scientific goals, the target selection, and survey design. The accompanying instrument portion of the FDR describes the instrument and optical design, integration and test plan, and the data management system. The companion Science Requirements Document provides information that guides the design. The DESI construction management plan is presented in the accompanying Project Execution Plan. Likewise, project cost and schedule are available in appropriate Project Office documents.

2 Science Motivation and Requirements

2.1 Introduction

DESI will explore some of the most fundamental questions in physical science: what is the composition of the Universe at large and what is the nature of space-time? These questions are now open to exploration because of recent discoveries. We summarize here the framework used to express these questions and the parameters used to quantify our understanding.

There are several pillars of the cosmological model that are now well established: 1) a period of rapid acceleration — *inflation* or a similar process — occurred in the early Universe, generating the primordial fluctuations, which seeded large scale structures, galaxies and galaxy clusters, which grew during the decelerating, matter dominated era 2) gravitational instabilities produced acoustic oscillations in the plasma, which were imprinted about 400,000 years after this inflation period, when photons decoupled from atoms and produced the Cosmic Microwave Background 3) this was followed by a period of matter domination, when small density fluctuations grew into large-scale structure, 4) comparatively recently, there was a transition to accelerated expansion driven by either a modification to General Relativity or a new form of energy – *dark energy* – not due to any particles known or unknown, and which contributes about 68% of the Universe's energy density, and 5) about 27% of the energy density today is due to matter outside the Standard Model of particle physics – *dark matter* – which is responsible for large-scale structure formation and accounts for galaxy rotation curves and the motions of galaxies in clusters.

That the Universe is expanding more and more rapidly was first revealed through measurements of Type Ia supernovae [1, 2], and subsequently confirmed using other techniques. Within General Relativity, accelerated expansion requires $\rho + 3p < 0$, where ρ is the total energy density and p is the total pressure of the matter, radiation, and other ingredients. The total equation of state $w = p/\rho$ must be less than $-1/3$ for accelerated expansion. The equation of state need not be a constant; in general it depends on time, or equivalently the scale size of the universe $a = 1/(1+z)$. From now on, we let w denote the equation of state of the dark energy component alone.

For ordinary non-relativistic matter, the pressure is negligible compared to the energy due to the rest mass and thus $w = 0$. For photons and other massless particles, $w = 1/3$. The cosmological constant term is equivalent to dark energy with $w = -1$. Generally, energy with an equation of state $w(a)$ evolves as $\rho(a) = \rho(a = 1)F(a)$, where $F(a) = 1$ for a cosmological constant and for a general equation of state $w(a)$ is

$$F(a) \equiv \exp\left[3 \int_a^1 \frac{da'}{a'}(1 + w(a'))\right]. \tag{2.1}$$

It is standard to parameterize the equation of state as

$$w(a) = w_0 + (1 - a)w_a, \tag{2.2}$$

which accurately reproduces distances for a wide range of models.

The contributions to the energy density of the Universe are conventionally expressed relative to the critical density

$$\rho_{\text{crit}} = \frac{3H_0^2}{8\pi G}, \tag{2.3}$$

which would be just sufficient to slow the expansion ultimately to zero in the absence of a dark energy component Ω_Λ. We write

$$\Omega_m = \frac{\rho_m}{\rho_{\text{crit}}}. \tag{2.4}$$
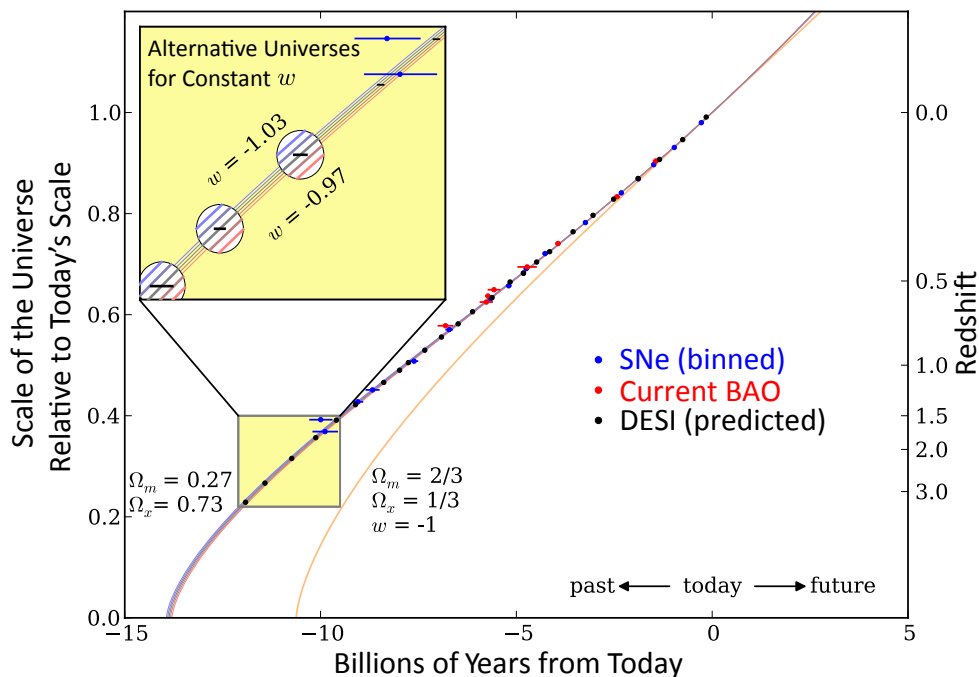
Figure 2.1: The expansion history of the Universe for different models of dark energy, holding the present-day Hubble constant fixed. The inset shows the spacing between five models with constant w ranging from -0.97 to -1.03, showing the exquisite precision required to distinguish these. Overlaid are measurements of the distance-redshift relation, translated into errors on lookback time at each redshift. Measurements from current supernovae, binned in redshift, are shown in blue; current BAO measurements from BOSS DR9, WiggleZ, and 6dF are shown in red; projections for DESI are shown in black. DESI measurements have the ability to make very tight constraints on dark energy, although we caution that this figure shows variations in only one cosmological parameter. Full forecasts, such as those presented in § 2.4.3, must marginalize over other cosmological parameters such as Ω_m and H_0.

We define $\Omega_{\rm r}$ for radiation and Ω_{DE} for dark energy analogously. The curvature term $\Omega_k = -k/H_0^2$ is defined so that General Relativity requires

$$\Omega_{\rm r} + \Omega_m + \Omega_k + \Omega_{DE} = 1 \tag{2.5}$$

for a Universe with spatial curvature k. The expansion rate of the Universe is given by

$$H(a) \equiv \frac{\dot{a}}{a} = H_0 \left[\Omega_{\rm r} a^{-4} + \Omega_m a^{-3} + \Omega_k a^{-2} + \Omega_{DE} F(a) \right]^{1/2} . \tag{2.6}$$

The contribution from radiation, $\Omega_{\rm r}$ is negligible today and inflation predicts that the curvature is zero. The Hubble constant today is $H_0 = h \times 100$ km/s/Mpc≈ 70 km/s/Mpc.

We have three possible explanations for the accelerating expansion of the Universe: a cosmological constant, equivalent to static dark energy with $w = -1$; a dynamical dark energy with $w(a) \neq -1$; or a failure of General Relativity. DESI is designed to address this fundamental question about the nature of the Universe. The challenge of distinguishing the cosmological constant solution from dark energy with w near -1 is displayed in Figure 2.1.

The Dark Energy Spectroscopic Instrument (DESI) [3] will provide precise spectroscopic redshifts of more than thirty million objects. From these will come three-dimensional maps of the

distribution of matter covering unprecedented volume. DESI will survey an enormous volume at $0.4 < z < 3.5$ using luminous red galaxies, emission line galaxies, and quasars, producing tight constraints on the large-scale clustering of the Universe. In addition, DESI will perform a Bright Galaxy Survey (BGS) of the $z < 0.4$ Universe, allowing the study of cosmic structure in the dark-energy-dominated epoch with much denser sampling. These data will help establish whether cosmic acceleration is due to a mysterious component of the Universe or a cosmic-scale modification of GR, and will constrain models of primordial inflation.

DESI will have a dramatic impact on our understanding of dark energy through its primary measurement, that of baryon acoustic oscillations. Waves that propagated in the electron-photon-baryon plasma before recombination imprint a feature at a known comoving physical scale (150 Mpc or 4.6×10^{24} m) in the distribution of separations between pairs of galaxies. Localizing this baryon acoustic oscillation (BAO) feature and comparing its apparent size to the known physical scale provides a measurement of the distance to the galaxy sample and thus the expansion history of the Universe. The BAO measurement was singled out by the Dark Energy Task Force [4] as having the fewest experimental uncertainties among the techniques for measuring dark energy; it simply depends on the galaxy locations, rather than their shapes or brightnesses. DESI's two-point correlation measurements will also detect the anisotropies in galaxy clustering — redshift space distortions (RSD) — due to the peculiar velocities of galaxies generated by density perturbations. This gives a direct measurement of the properties of gravity at each redshift, through its effect on galaxies' motions.

In addition to the constraints on dark energy, the galaxy and Ly-α flux power spectra will reflect signatures of neutrino mass, scale dependence of the primordial density fluctuations from inflation, and possible indications of modified gravity. To realize the potential of these techniques requires an enormous number of redshifts over a deep, wide volume and thus a substantial investment in a new instrument with capabilities well beyond existing facilities and for which we can utilize a substantial portion of the observing time.

The DESI survey will have considerable impact beyond these cosmological highlights on the study of galaxies, quasars, and stars. Spectroscopy is a core tool of astrophysics, and the ability to combine many millions of spectra with modern wide-field, multi-wavelength imaging surveys will yield rich opportunities. While the DESI collaboration includes members planning to work on these topics, we do not discuss these in this design report, as they are not driving requirements. We make one brief exception for the Milky Way Survey (§ 2.6), as it will involve a substantial number of targets that piggyback on the Bright Galaxy Survey, using fibers that have no suitable galaxy available within their patrol radius.

2.2 Measuring Distances with Baryon Acoustic Oscillations

DESI will measure the expansion of the Universe by observing the imprint of baryon acoustic oscillations set down in the first 380,000 years of its existence. This pattern has the same source as the pattern seen in the cosmic microwave background, but DESI will map it as a function of cosmic time, while the CMB can see it only at one instant. The pattern is imprinted on all matter at large scales and can be viewed by observing galaxies of various kinds or by observing the distribution of neutral hydrogen across the cosmos, and shows up as excess correlations at the characteristic distance of the sound horizon at decoupling.

2.2.1 Theory

Initial fluctuations in density and pressure provided sources for sound waves that propagated in the photon-electron-baryon plasma of the early Universe (see, for example, [5]). These sound waves propagated with a speed approximately $c/\sqrt{3}$ until the Universe cooled sufficiently for electrons and ions to recombine to neutral atoms, causing the sound speed to drop dramatically. An excess of matter was left both at the source of the wave and at the surface where these waves terminated. The matter excesses at these locations left their imprint on the large-scale structure of galaxies and hydrogen gas. Before a wave stopped, it traveled a co-moving distance $s \approx 150$ Mpc, which can be computed to precision 0.3% from cosmological parameters extremely well measured in CMB.

Viewed transversely, the 150-Mpc ruler subtends an angle θ such that

$$s = (1+z)D_A(z)\theta = \theta \int_0^z \frac{c\,dz'}{H(z')} \tag{2.7}$$

where $D_A(z)$ is the angular-diameter distance to an object at redshift z. The final equality holds only if the curvature is zero.

While the CMB gives us a purely angular correlation function, the characteristic scale is present in the three-dimensional distribution of large-scale structure. Viewed along the line of sight, correlations are enhanced for galaxy pairs separated by Δz such that

$$\frac{c\Delta z}{H(z)} \approx s \tag{2.8}$$

This latter measurement requires a spectroscopic survey to resolve the full three-dimensional density distribution of galaxies.

The observation of the peak in the two-point correlation function thus provides a means of measuring both the angular diameter distance, $D_A(z)$ and the Hubble expansion rate, $H(z)$. The ability of the BAO method to directly probe $H(z)$ is unique among dark energy probes. This becomes progressively more important at higher redshifts since H measures the instantaneous expansion rate (and through it, the total energy density of the Universe) while D_A measures the integrated expansion history. Measuring both improves our ability to distinguish between different cosmological models.

2.2.2 BAO in Galaxies

The best developed application of the BAO technique uses galaxies as tracers of the matter distribution; the BAO feature appears in the two-point correlation function of galaxies, the probability, in excess of random, that two galaxies are separated by a distance r. This has been achieved with high statistical significance in several measurements spanning the redshift range from $z = 0$ to $z = 1$.
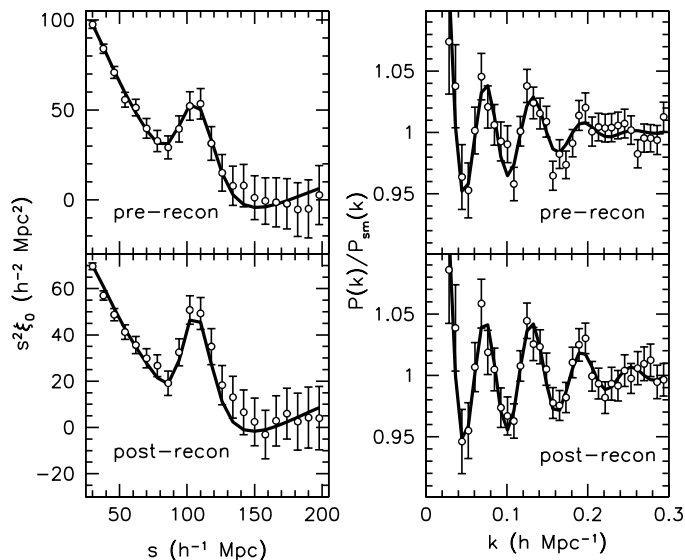
Figure 2.2: The angle-averaged correlation functions [left] and power spectra [right], before [top] and after [bottom] reconstruction measured using the BOSS DR11 CMASS galaxy sample [6]. The BAO feature is clearly detected at over 7σ as a peak in the correlation function and a corresponding set of oscillations in the power spectrum.

The highest significance detection ($> 7\sigma$) is currently that of the Baryon Oscillation Spectroscopic Survey (BOSS) using the $z > 0.45$ sample [6, 7]. We show representative data in Figure 2.2. These data measured the distance-like quantity $D_V(z) \equiv ((1 + z)D_A)^{2/3}(cz/H(z))^{1/3}$ to a redshift of 0.57 to 1.0%, the most precise measurement using the BAO technique. The lower redshift $z < 0.45$ sample in BOSS constrained the same combination of distances to 2%. At still lower redshifts, the 6-Degree Field Galaxy Redshift Survey [8] measured the distance to $z = 0.106$ with 4.5% accuracy At a somewhat higher redshift, the WiggleZ galaxy survey measured the distance to a redshift of 0.7 to 4% [9]. This combination of these measurements has for the first time enabled mapping the distance-redshift relation purely from BAO measurements.

Most of these measurements used the galaxy correlation function averaged over the orientation of the pair to the line of sight to measure D_V, a combination of D_A and H. More recent work has also measured the correlation functions transverse and parallel to the line of sight, allowing one to break the degeneracy between D_A and H that exists in purely angle averaged measurements.

The current generation of surveys is an excellent proving ground for analysis techniques. For instance, the BOSS experiment compared analyses done in Fourier and in configuration space and used different algorithms for estimating distances from the resulting two-point functions. All these yielded consistent distance measurements, given the statistical precision of the measurements. While the level of consistency is not at the level required by DESI, ongoing surveys provide a clear roadmap for developing and validating improvements to these analysis techniques. The current measurements provide an important validation of our forecasts for DESI presented below.

The non-linear evolution of the matter density field broadens the acoustic peak, potentially decreasing the precision on the distance measurement, and causes a small shift in the peak location, thereby biasing the distance. Ref. [10] pointed out that because this broadening is caused by the large-scale velocity flows resulting from gravitational forces, the effect may be substantially reversed by estimating the velocity fields from the large-scale structure map and moving the galaxies back

to their initial positions. In addition to a notable improvement in the recovered statistical errors, this reconstruction also mitigates the shifts in the distance scale due to nonlinear evolution, with numerical tests showing suppression to below 0.1%. Reconstruction was first applied to the SDSS-II galaxy survey [11], improving the statistical precision by a factor of 1.7. Galaxy samples from more recent SDSS results, DR11, yield similar improvements after reconstruction. See Figure 2.2. As with the other analysis methods, we expect improvements to reconstruction algorithms before the DESI measurements become available. We however choose to be conservative and assume a reconstruction performance similar to what has already been demonstrated with current data.

Observational Systematics

The BAO method is simple in principle — all one requires are the three-dimensional positions of galaxies. The need to preserve the BAO feature along the line of sight sets the requirement on redshift precision. This precision, as stated in the Level 2 Survey Data Set Requirements is $\sigma_z/(1+z) \sim 0.0005$ per galaxy, which is easily within the state-of-the-art and achieved throughout our wavelength range in the spectrograph design.

The angular and radial selection functions of the survey can induce systematic uncertainties. The angular selection function is determined by the imaging survey used for targeting, and may be spuriously modulated by photometric calibrations, seeing and extinction variations, and image deblending. All of these effects are intrinsically angular effects and therefore may be separated from the BAO feature, which is a feature in three-dimensional physical space (not isolated to the angular degrees of freedom). A similar separation is possible for systematics in the radial selection function of the survey. The impact of these is therefore expected to be small. In addition, there has been considerable work [12, 13] developing techniques to further mitigate these effects.

The ongoing BAO surveys provide the opportunity to identify and quantify observational systematics. DESI will benefit greatly from this work, but it also faces some unique challenges. The most important of these arise from the fiber positioning system and from the forest of sky lines, which impinge on the radial selection function. The limited patrol radius of the fiber positioners causes the highest density regions to be sampled less completely than lower density regions. This particularly affects the observer's line of sight and can skew the anisotropic correlation pattern. High sky brightness at certain wavelengths makes it difficult to find [O II] emission lines, thereby reducing the spectroscopic completeness at specific redshifts. Initial studies have shown that these survey artifacts can influence the measured clustering, but we expect both to be correctable to good accuracy, as the source of the variations can be tracked with high fidelity. Finding the optimal method to achieve the full statistical precision inherent in the data is an ongoing project of the science team.

Theoretical Systematics

The robustness and accuracy of the BAO method derive from the simplicity of the early Universe and the precision with which we know the speed and time of propagation of sound waves in the primordial plasma. The evolution of density fluctuations in the Universe is very well described by linear perturbation theory and is now exquisitely tested by the recent measurements of temperature fluctuations in the Cosmic Microwave Background radiation by the *Planck* satellite [14, 15, 16]. The current CMB measurements constrain the size of the BAO standard ruler to 0.3%. This uncertainty is folded into our forecasts for DESI. Furthermore, any miscalibrations in the acoustic scale would affect principally the determination of the Hubble constant, not the dark energy constraints [17].

The sound waves travel a comoving distance of 150 Mpc, setting the BAO scale to be much larger

than the scale of gravitational collapse even in the present Universe (about 10 Mpc). Analytical calculations, verified by direct numerical simulations, have found the nonlinear evolution of the density field alters the BAO scale by 0.3% at the present epoch, and even less at the higher redshifts probed by DESI.

Galaxy formation may result in an additional shift in the BAO scale due to mismatched weighting of high and low density regions. Initial perturbative and numerical studies [18, 19, 20, 21, 22, 23, 24] also find these shifts to be small, with the most extreme shifts of order 0.5%. As mentioned above, density-field reconstruction applied to simulations reduces these shifts to the 0.1% level without the need for further modeling. We expect that further modeling from theory and simulations will allow us to robustly limit these uncertainties to well below the DESI statistical limits. In addition, the DESI target samples are designed to overlap in multiple redshift ranges, allowing empirical tests of the robustness of the BAO measurements to different tracer populations.

A recently discovered astrophysical effect that could affect the BAO feature arises from the relative velocities of the baryons and the dark matter at the recombination epoch [25, 26]. This modulates the formation of the earliest protogalaxies and potentially could persist to their descendants (some of which would be measured by DESI). This modulation is due to the same pressure forces that create the BAO, and the impact could shift the measured acoustic scale. While this effect is expected to be negligible for the galaxies probed by DESI, the possibility of a systematic bias in the inferred distance scale can not be ruled out on theoretical grounds. Fortunately, [27] demonstrate that this effect would also create a distinctive three-point function signal measurable in DESI that would diagnose any contamination from this effect (also [28]).

All of the above strongly argue that the theoretical systematic effects associated with the BAO-scale measurements are either intrinsically or correctable to below the 0.1% level required by DESI.

2.2.3   BAO in the Ly-α Forest

Measuring BAO with galaxies as tracers is a mature method [29, 9]. Such measurements become much more difficult for $z \gtrsim 2.0$ where galaxy redshifts are harder to get. However, measuring dark energy properties at this high redshift allows us to probe the Universe well before the advent of accelerated expansion. An interesting possibility is that dark energy density does not become completely negligible at high redshift, as predicted by the cosmological constant or other models with $w \simeq -1$, but rather remains at a level predicted by some particle-physics models and detectable by future surveys [30, 31, 32, 33, 34, 35]. Such a component can only be measured or excluded by a technique sensitive to the expansion history at high redshift.

The Ly-α forest provides the means to measure BAO at redshifts larger than 2. The forest is a collection of absorption features in the spectra of distant quasars blue-ward of the Ly-α emission line [36]. These features arise because the light from a quasar is absorbed by neutral hydrogen in the intergalactic medium. Since the quasar light is constantly red-shifting, hydrogen at different redshifts absorbs at different observed wavelengths in the quasar spectrum. The amount of absorption reflects the local density of neutral hydrogen, which in turn traces the dark matter field on sufficiently large scales. Numerical simulations and analytical work show that for plausible scenarios, the Ly-α forest is well within the linear biasing regime of scales relevant for BAO [37, 38, 39]. Therefore, measuring three-dimensional correlations in the flux fluctuations of the Ly-α forest provides an accurate method for detecting BAO correlations [37, 40, 41, 42]

Using the Ly-α forest to measure the three-dimensional structure of the Universe became possible with the advent of BOSS, which was the first survey to have a sufficiently high density of quasars to measure correlations on truly cosmological scales. This was done in 2011 [43]. At the beginning of 2013, the first detection of BAO in the Ly-α forest was published in a series of papers
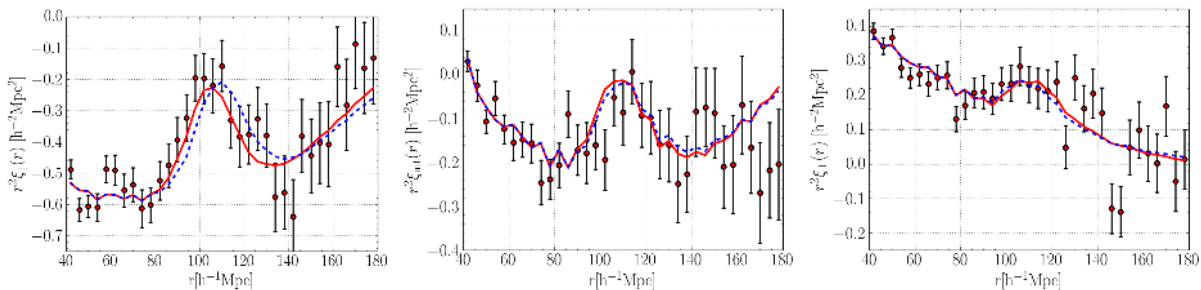
Figure 2.3: Correlation functions of Ly-α forest flux fluctuations based on the BOSS DR11 quasars [47], binned in the cosine of the angle to the line of sight, μ ($\mu = 1$ is along the line of sight, $\mu = 0$ is perpendicular to the line of sight). From left to right, the bins are $\mu > 0.8$, $0.5 < \mu < 0.8$ and $\mu < 0.5$. The points are the measured correlation function, the solid line is the best fit model, while the dashed line is the best fit assuming a fiducial cosmology. These results measure the optimal combination $D_A^{0.3} H^{-0.7}$ to 2%.

[44, 45, 46]. These were recently updated to the almost complete BOSS sample in [47] (Figure 2.3) yielding a 5σ detection of the BAO feature.

The redshift-space distortions in the Ly-α forest are larger than in galaxy-based measurements [43, 37]. Thus the signal-to-noise for the radial modes is considerably higher than for transverse modes. Consequently, in contrast to the galaxy measurements, the Ly-α forest BAO measurements measure the Hubble parameter $H(z)$ with greater precision than the angular diameter distance $D_A(z)$. For instance, [47] find that the combination $D_A^{0.3} H^{-0.7}$ is optimally constrained to $\sim 2\%$.

Systematics

Inevitably, there will be systematic effects that could distort the Ly-α measurements, but these should produce broadband contamination and would not affect our ability to measure an isolated feature in the data, such as the BAO peak. However, unless carefully accounted for, these systematics could contaminate secondary science, such as Ly-α broadband power measurements, neutrino masses and warm dark matter constraints.

Astrophysical contaminants include sources of non-gravitational large scale fluctuations, such as He II reionization and fluctuations in the photo-ionization background [48, 49, 50, 51, 52]. There are also targeting systematics – quasars with significant absorption in the forest region are considerably easier to target, since they are easier to distinguish from stars. As a result, observed Ly-α forest regions are not sampling the Universe randomly, but prefer overdense lines of sight. Back-of-the-envelope calculations show that this effect is small, although more work should be done to confirm this[1]. Finally, there are metal contaminations. For example, Si III that tracks the hydrogen fluctuations produces a line that contaminates the Ly-α forest flux measurements at separation of 2271 km/s. The cross-correlation between Ly-α forest absorption and Si III absorption, if misinterpreted as Ly-α-to-Ly-α correlations could bias the BAO measurements [43, 47]. Further contamination arises where the metal absorption traces large scale structures at a significantly different redshift. For example C IV traces structure at $z = 1.7$ at wavelengths which probe the Ly-α forest at $z = 2.4$ [53]. For BAO measurements these can be reliably corrected by including them as a part of the model. For other uses, such as broadband power spectrum measurements, a combination of nuisance modeling, accurate mock spectra and numerical simulations should remove

---

[1]There is an additional effect because Ly-α quasar lines of sight terminate in quasars, which are themselves tracers of the underlying structure, but this can be explicitly shown to be a small effect.

any potential biases associated with these complications.

Perhaps the most important systematic effects will come from imperfections in the instrument and data reduction. For example, artificial features in the mean transmission at the position of galactic Balmer transitions were noticed in BOSS data [44]. These were tracked down to the imperfect interpolation in calibration vectors when these features were masked in calibration stars. Although such effects are on average calibrated out, they can in principle produce sharp features in correlation at certain pairs of wavelengths that could potentially contaminate the BAO measurements. Other effects include noise calibration and its Poisson nature, imperfect sky subtraction, etc. Fortunately, there are no fundamental obstacles to modeling the listed systematics with a carefully executed pipeline. The sheer amount of data that will be available and the relatively high signal-to-noise of true small scale fluctuations in the forest will allow us to check the data in many different ways and validate the data reduction pipeline.

2.3 Measuring Growth of Structure with Redshift Space Distortions

DESI will observe redshifts, which reflect the velocities due to expansion, but also the peculiar velocities due to gravitational attraction by large scale structure. Peculiar velocities are observable in redshift surveys because they alter the correlations between galaxies along the line of sight, resulting in an anisotropy in the observed clustering. Comparing the expansion history and the growth of large scale structure from redshift space distortions will allow DESI to test General Relativity.

2.3.1 Theory

Galaxies and quasars are point tracers of the underlying cosmic structure. The physics of how they trace the dark matter fluctuations is well understood based on arguments about locality of galaxy formation [54, 55, 56]. On very large scales bias is scale independent and redshift-space distortions are described by linear perturbation theory. Beyond-linear perturbative corrections can be used on intermediate scales before perturbation theory breaks down entirely on small scales [57, 58, 59].

The measurement of the growth of structure relies on redshift-space distortions seen in galaxy surveys. Even though we expect the clustering of galaxies in real space to have no preferred direction, galaxy maps produced by estimating distances from redshifts obtained in spectroscopic surveys reveal an anisotropic galaxy distribution. The anisotropies arise because galaxy redshifts, from which distances are inferred, include components from both the Hubble flow and peculiar velocities driven by the clustering of matter. Measurements of the anisotropies allow constraints to be placed on the rate of growth of clustering [60, 61].

On large scales, the observed large-scale structure is basically described by a small fractional perturbation $\delta(\mathbf{x}) = \delta\rho(\mathbf{x})/\overline{\rho} = (\rho(\mathbf{x}) - \overline{\rho})/\overline{\rho}$ to the uniform density. Ignoring the higher-order contributions, the perturbation in redshift space (δ_s) is related to the real space perturbation at directional cosine μ between line-of-sight direction and the wave-number $\mathbf{k}$, by the Kaiser relation [62],

$$\delta_s(\mathbf{k}) = \delta(\mathbf{k})(1 + \beta\mu^2) \tag{2.9}$$

Here $\beta = f/b$, where b is the galaxy bias and f is related to the linear growth function $D(a)$ by

$$f = \frac{d\ln D(a)}{d\ln a} . \tag{2.10}$$

In the linear regime, density perturbations grow proportional to $D(z)$ which increases with decreasing z.

In GR, $D(z)$ is completely specified by the expansion history even in the presence of dark energy; this is no longer generically true in alternative theories of gravity. The behavior of f in GR is given, to a good approximation, by

$$f \simeq \Omega_m(z)^\gamma, \tag{2.11}$$

where γ is the growth index, approximately 0.55 in GR, and where $\Omega_m(z)$ is the fraction of the total energy density in the form of matter at redshift z. In alternative gravity theories, a common simple parameterization of the modified growth rate is to alter the growth index γ. [63] demonstrated that a DESI-like survey could constrain γ to 0.04 (7%). More general modifications might involve modifying (in a time- and scale-dependent manner) the potentials that enter the metric. Precise growth measurements over a wide range of redshifts and scales, combined with constraints from overlapping CMB and weak lensing surveys, make large galaxy surveys like DESI excellent probes of gravity (see [64] for a recent review). Here, we focus on scale-independent growth rates for large-scale structure, but the DESI data set will allow more complicated investigations.

As an important example of extensions, we highlight the Bright Galaxy Survey, where we will be mapping a smaller volume ($z < 0.4$) at substantially higher number density and with more diversity of galaxies. This redshift range is crucial because it is when dark energy dominates and any associated modifications of gravity would be expected to be strongest. Getting the best precision out of this limited volume requires spectroscopy to produce a 3-D map of the density field. The BGS will test for modifications of gravity directly via the redshift-distortion method, including the novel methods of using multiple tracers in order to suppress sample variance [65]. But the search can be extended via spectroscopic detection of clusters and groups, along with galaxy halo occupation modeling, to measure the amplitude of clustering by halo abundances [66, 67]. The maps can also be correlated with weak lensing maps (e.g., from DES, LSST, Euclid, or CMB-S4) to measure the amplitude of clustering [68, 69]. Comparing the observed velocity field to the expected velocity field sourced from the lensing matter overdensities enables further tests of modified gravity models of cosmic acceleration [60]. Finally, the more detailed map will allow tests of screening theories on smaller scales [70, 71], in which one considers the response of individual galaxies to the predicted gravitational field.

In the Kaiser approximation, the redshift space power spectrum, P_s, is given by

$$P_s(\mathbf{k}) = (b + f\mu^2)^2 P_m(k) \tag{2.12}$$

where P_m is the linear theory mass power spectrum. In principle, this prescribed anisotropy provides a means of measuring f, and through it the growth of gravitational structures. However, in the above, the measurements of f are degenerate with the amplitude of the matter power spectrum. Therefore the combination $f(z)\sigma_8(z)$ is the actual observable, where the normalization of the power spectrum $P(k)$ is proportional to $\sigma_8^2(z)$ [2].

2.3.2   Systematics

Galaxies are expected to follow the same gravitational potential as the dark matter and hence have the same velocities. The main theoretical systematic uncertainty in RSD is that nonlinear velocity effects extend to rather large scales and give rise to a scale-dependent and angle-dependent clustering signal. It is easy to see these effects in any real redshift survey: one sees elongated features along the line of sight, called the Fingers of God (FoG). The FoG are caused by random velocities inside virialized objects such as clusters, which scatter galaxies along the radial direction in redshift space, even if they have a localized spatial position in real space. This is just an extreme example and other related effects, such as nonlinear infall streaming motions, also cause nonlinear corrections. In addition, RSD measure velocities as sampled at the galaxy positions. One is thus probing not the velocity field, but rather the momentum density field. Galaxies are a biased tracer of the dark matter and this introduces scale dependent effects into RSD statistics even if galaxies are simply a linear tracer of the dark matter.

There are a plethora of approaches [72, 73, 74, 57, 58, 59] to modeling redshift space distortions in the literature, and the analyses in Table 2.1 make use of many of them. It has been firmly established that the Kaiser formula is inadequate to recover information faithfully on the quasilinear scales of interest, and so most analyses now adopt some form of perturbative corrections. However, because these corrections depend strongly on the halo bias [75, 76], methods calibrated on purely the dark matter power spectrum are of limited utility. Moreover, the details of the mapping between galaxies and dark matter halos also strongly modify the correlation function, mostly through FoG

---

[2] σ_8^2 is defined to be the variance of the matter density field averaged in spheres of 8 h^{-1}Mpc and traditionally used to parametrize the amplitude of the power spectrum.

Table 2.1: Compilation of RSD-based $f\sigma_8$ measurements from [89]. For the BOSS DR11 galaxy sample we cite the measurement of [85]. Other analyses of DR11 find consistent results [87, 84]

z	$f\sigma_8$	survey	reference
0.067	0.42 ± 0.06	6dFGRS	[80]
0.17	0.51 ± 0.06	2dFGRS	[90]
0.22	0.42 ± 0.07	WiggleZ	[82]
0.25	0.35 ± 0.06	SDSS LRG	[77]
0.37	0.46 ± 0.04	SDSS LRG	[77]
0.41	0.45 ± 0.04	WiggleZ	[82]
0.57	0.45 ± 0.03	BOSS CMASS	[85]
0.6	0.43 ± 0.04	WiggleZ	[82]
0.77	0.49 ± 0.18	VVDS	[91]
0.78	0.38 ± 0.04	WiggleZ	[82]
0.80	0.47 ± 0.08	VIPERS	[92]
1.4	0.48 ± 0.12	FastSound	[93]

effects. All of these effects can induce 10% effects on RSD at $k \sim 0.1\ h/\mathrm{Mpc}$. Current models of RSD are able to reproduce these nonlinear effects at the percent level for $k < 0.05$–$0.1\ h/\mathrm{Mpc}$. Extending this to smaller scales would increase the power of the DESI RSD survey. This will require us to improve our bias models and the realism of our simulations.

Most of the observational systematics examined in detail in the SDSS-III BOSS [see 12] primarily affect clustering on the largest scales; currently these are of little concern for RSD measurements, for which the signal comes primarily from the smallest scales included in the measurements. The most important systematic effect is the estimate of a survey's radial selection function [77, 12]. Since the redshift distribution of targets cannot be predicted precisely a priori, it must be measured directly from the observed galaxies' redshift distribution. Doing so removes some cosmological radial modes from the observed galaxy overdensity field, resulting in a bias in the monopole-quadrupole amplitudes at the $< 0.2\sigma$ level. The ratio of systematic to statistical uncertainty should remain relatively constant with survey area for a given redshift distribution, since the statistical errors on the correlation function and $n(z)$ shrink at the same rate.

2.3.3 Current Status of RSD Measurements

Redshift-space-distortion measurements have now been performed on a host of surveys, which we summarize in Table 2.1 and show in the left panel of Figure 2.4; taken together, these surveys provide a measure of the growth rate of cosmic structure good to about 3% in the low redshift Universe. Almost all of these measurements of $f\sigma_8$ are derived from the anisotropy in the two-point correlations of the observed galaxy density field. The anisotropic correlation from SDSS-III BOSS DR11 CMASS sample is shown in Figure 2.5. While there have been some analyses directly on the two-dimensional correlation function $\xi(r_p, r_\pi)$ [e.g., 78, 79, 80, 81], most authors further compress the data into multipoles [e.g., 82, 77, 83, 84, 85] or wedges [86, 87]. Efficient information compression is necessary when the covariance matrix of the observables are estimated from a finite number of mock surveys [88].

Most of these measurements assume a flat ΛCDM cosmology to model the redshift-distance relation (see [81] for an exception); dropping this assumption degrades the measurement of $f\sigma_8$. However, the combination of geometric and dynamical constraints available from the analysis of
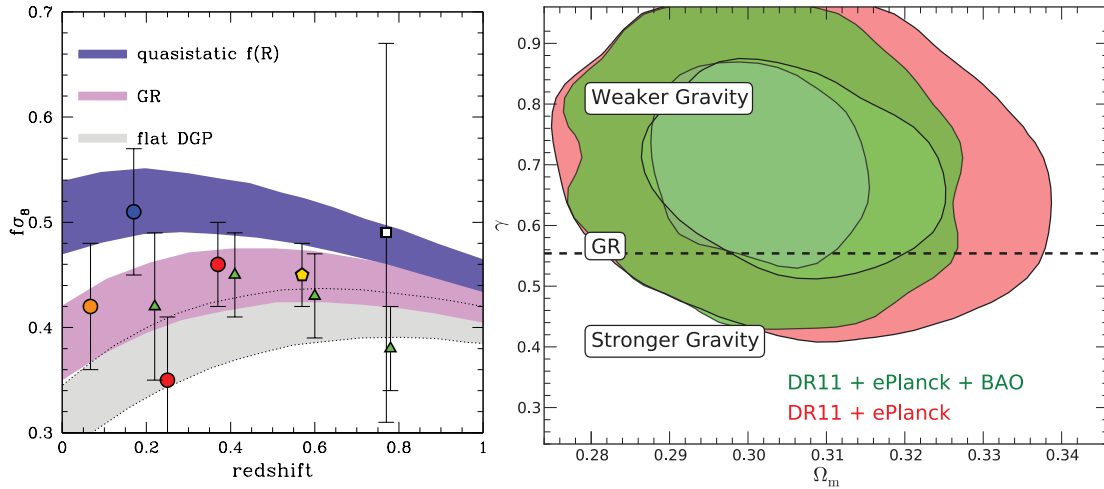
Figure 2.4: *Left:* The data points show the CMASS DR11 measurement of $f\sigma_8$ (gold pentagon; [85]) along with similar, low redshift, measurements and 1σ error bars as presented in Table 2.1. The three stripes show theoretical predictions for different gravity models allowing for uncertainty in the background cosmological parameters, constrained using only the WMAP 7 data [94]. Figure adapted from [89]. *Right:* Joint constraints in the Ω_m-γ plane from BOSS DR11, where γ is the growth index of structure, as defined in Eq. (2.11). Figure taken from [85].
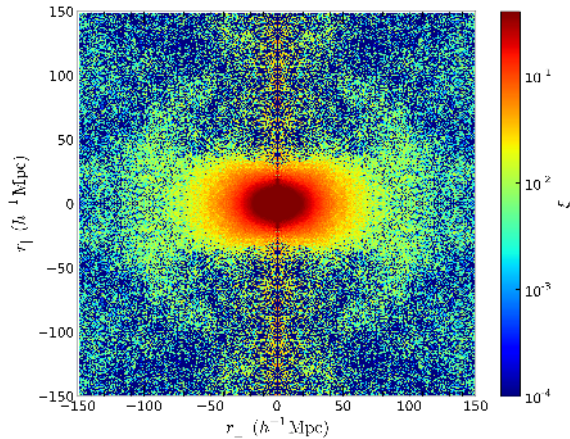
Figure 2.5: The two-dimensional correlation function of the BOSS DR11 CMASS galaxies, measured perpendicular (x-axis) and parallel (y-axis) to the line of sight. The BAO ring, distorted by redshift space distortions is clearly visible, as is the characteristic squashing of the correlation function on large scales.

anisotropic galaxy clustering is quite complementary to isotropic BAO measurements for constraining dark energy. For instance, in the case of SDSS-III BOSS DR11 for a flat wCDM cosmology, the combination of Planck and the BOSS BAO measurements constrain $w = -1.01 \pm 0.08$ [6], while including the geometric and dynamical information in the quadrupole correlation function (term proportional to μ^2) yields $w = -0.993 \pm 0.056$ [85].

Considering instead tests of gravity given a "known" expansion history, Figure 2.4 shows that for a flat ΛCDM cosmology in general relativity, the predicted redshift evolution of the observable

$f\sigma_8$ is quite mild in the redshift range that has been studied observationally. These observations can begin to distinguish between gravity models ($f(R)$ and DGP are shown), though there is still substantial uncertainty in the theoretical predictions simply due to uncertainties in both the matter density Ω_m and overall matter power spectrum normalization, σ_8. The right-hand side of Figure 2.4 shows constraints in the Ω_m-γ plane from BOSS DR11 [85]. These data yield a 16% constraint on the growth index. DESI will improve on the precision of the growth constraint from all previous measurements by a factor of $\sim$4–10 [95], depending on advances in analysis and theoretical modeling. In addition, it will provide measurements to significantly higher redshifts.

Two surveys in particular are pathfinders for DESI targets: WiggleZ [96] analyzed emission line galaxies with bias b near 1, while SDSS-II and SDSS-III BOSS study luminous red galaxies (LRGs) with a bias near 2. WiggleZ included much smaller scales in their RSD analysis, which led to impressive constraints given the number of galaxies in the survey. However, they were not able to generate easily a large N-body simulation volume capable of resolving the halos expected to host emission line galaxies, and so their theoretical modeling is necessarily less well-tested. By comparison, LRGs are hosted by massive halos that can easily be simulated. The perturbation-based model of [83] was carefully calibrated against N-body-based mock-galaxy catalog and included realistic effects like the "Fingers-of-God" (the elongated structure in the right panel of Figure 2.5). However, because these effects are so strong, their analysis was restricted to relatively large scales.

Ongoing progress in combining the perturbative analytic results with those of N-body simulations should pave way for the increased theoretical prediction accuracy necessary to extract RSD information at small spatial scales

2.4 Distance, Growth, Dark Energy, and Curvature Constraint Forecasts

DESI's observational program defined in the Requirements Document and described in this Report specifies the numbers of galaxies and Ly-α forest sources and their distribution that will be measured. Using the specified quality of those observations, we can predict the precision with which cosmological parameters will be determined by DESI. Thanks to the unprecedented scope of DESI's spectroscopic measurements, these measurements will take us to a new level — Stage-IV — in cosmological exploration.

2.4.1 Forecasting Overview

We use the Fisher matrix formalism to estimate the parameter constraining power of the finished survey, largely following [95]. Our baseline cosmological model is flat ΛCDM. This model is specified by seven parameters, which are listed together with their fiducial values in Table 2.2. Parameter symbols have their conventional meanings. Our standard fiducial parameter values follow the *Planck* 2013 results, specifically the P+WP+highL+BAO (P from *Planck*, WP from *WMAP*, highL from high resolution CMB experiments like ACT and SPT) column of Table 5 of [14]. The difference from the *Planck* 2015 is negligible for these purposes. In addition to the conventional six parameters of the minimal cosmological model, we also always vary the amount of tensor modes; however this is largely irrelevant because the T/S measurement is completely dominated by *Planck* and essentially uncorrelated with other parameters.

Isolating the BAO feature gives the most robust, but also most pessimistic, view of the information that one can recover from galaxy clustering measurements, since BAO can be measured even in the presence of large unknown systematic effects (very generally, these will not change the BAO scale [22]). We quote errors on the transverse and radial BAO scales as errors on $D_A(z)/s$ and $H(z)s$, respectively, where s is the BAO length scale. For galaxy and quasar clustering, these measurements are correlated at each redshift with a correlation coefficient of 0.4.

We also quote errors on an isotropic dilation factor R/s, defined as the error one would measure on a single parameter that rescales radial and transverse directions by equal amounts. In this case, for a small change in R, the corresponding variations in the model values of D_A and H are

$$D_A = \left(1 + \frac{\delta R}{R_{\text{fid}}}\right) D_{A,\text{fid}} \tag{2.13}$$

and

$$H = \left(1 + \frac{\delta R}{R_{\text{fid}}}\right)^{-1} H_{\text{fid}} \tag{2.14}$$

where $D_{A,\text{fid}}(z)$ and $H_{\text{fid}}(z)$ are the angular diameter distance and Hubble parameter in a fiducial Universe. An explicit definition of R in terms of the measured H and D_A is generally not needed and depends on the experimental scenario. The simplest cases are easy to understand: for a purely transverse measurement (e.g., photometric survey) $R = D_A$, while for a purely radial measurement (e.g., something closer to the Ly-α forest, although it is not purely radial) $R = H^{-1}$ (or $R = H^{-1}H_{\text{fid}}D_{A,\text{fid}}$, if one is concerned about inequivalent units). For intermediate cases like typical galaxy clustering, the appropriate combination of H and D_A can always be determined given the covariance matrix between them. For example, it is approximately proportional to $D_V(z) \equiv ((1+z)D_A)^{2/3}(cz/H(z))^{1/3}$ in analyses of spherically averaged clustering, such as from 6dF, BOSS, and WiggleZ.

Going beyond BAO, we use "broadband" galaxy power, i.e. measurements of the power spectrum as a function of redshift, wavenumber and angle with respect to the line of sight. This

Table 2.2: Parameterization of the cosmological model and parameter values for the fiducial model. The seven parameters in the upper part of the table are always free. Parameters in the second half of the table are extensions of the simplest model discussed below.

Parameter	Value	Description
ω_b	0.02214	Physical baryon density $\omega_b = \Omega_b h^2$ $h = H_0/(100 \text{ km s}^{-1}\text{Mpc}^{-1}))$
ω_m	0.1414	Physical matter density $\omega_m = \Omega_m h^2$ (including neutrinos which are non-relativistic at $z = 0$)
θ_s	0.59680 degrees	Angular size of sound horizon at the surface of last scattering acting as a proxy for Hubble's constant
A_s	2.198×10^{-9}	Amplitude of the primordial power spectrum at $k = 0.05 \text{ Mpc}^{-1}$ (for the numerical Fisher matrix we actually use $\log_{10} A_s$)
n_s	0.9608	Spectral index of primordial matter fluctuations with $P(k) \propto k^{n_s}$
τ	0.092	Optical depth to the last scattering surface assuming instantaneous reionization.
T/S	0	Ratio of tensor to scalar perturbations (we assume inflationary tensor fluctuation's spectral index $n_t = -\frac{1}{8}T/S$)
w_0	-1	Equation of state of dark-energy $p = w\rho$
w_a	0	Variable equation of state of dark energy of the form $w = w_0 + (1-a)w_a$
Ω_k	0	Curvature of the homogeneous model
α_s	0	Running of the spectral index $\alpha_s = d\log n_s/d\log k$ with pivot scale $k = 0.05 \text{ Mpc}^{-1}$
Σm_ν	0.06 eV	Sum of neutrino masses (we assume they are degenerate)
$N_{\nu,\text{eff}}$	3.04	Effective number of neutrino species ($N_{\nu,\text{eff}} > 3.04 \rightarrow$ dark radiation).

treatment automatically recovers all available information from the two-point clustering, i.e. not just the shape of the isotropic power spectrum, but also redshift-space distortions, Alcock-Paczynski [97], and the BAO information.

The broadband Fisher matrix is calculated by combining the inverse variance of the power spectrum $P(\mathbf{k})$ of each Fourier mode with the derivative of power in each mode with respect to set of cosmological parameters. We divide the survey into a set of redshift slices and coadd the resulting matrices. The model for the three-dimensional power spectrum of the galaxy or Ly-α distribution is

$$\tilde{P}(k, \mu, z) = b(z)^2 (1 + \beta(z)\mu^2)^2 P_{mass}(k, z) D(k, \mu, z) , \qquad (2.15)$$

where μ is the angle of the wavevector to the line of sight, k is the wavenumber, b is the linear bias parameter, β the redshift space distortion parameter and $D(k, \mu, z)$ is a non-linear correction calibrated from simulations (for the Ly-α forest this is given by [98] and for galaxies it is based on the information damping factors of [99]). The Fisher matrix calculation will integrate over all μ and a suitable range of k. The inverse variance of the power spectrum of each mode gets contributions from both the intrinsic sample variance and the shot noise. This results in an effective volume $V_{\text{eff}}(\tilde{P})$ of each redshift slice that is given by $V_{\text{eff}}(\tilde{P}) = [1 + 1/(n\tilde{P})]^{-2} V_{\text{survey}}$ [100]. The value nP represents the ratio of true clustering power to that from shot noise. Alternatively, it can be seen

as the signal-to-noise ratio per mode (redshift, wavenumber, and orientation slice): if $nP > 1$ then roughly the signal exceeds the sample variance uncertainty for that mode.

For the galaxy survey, we use large-scale broadband power up to some quoted k_{max}. At small scales, $k > k_{max}$, we continue to use BAO information. We use two simple choices of k_{max}: 0.1 $h\,\mathrm{Mpc}^{-1}$ and 0.2 $h\,\mathrm{Mpc}^{-1}$. These cutoffs are intended to indicate sensitivity of results to the effective scale where information is recovered after making corrections for non-linearity, after marginalization over suitable non-linear bias parameters. It will be a major program of the next decade to figure out exactly how to do this fitting in practice for a high precision survey like DESI; how well we can do this will determine how well we can measure parameters. As discussed in [95], $k_{max} \sim 0.1$ $h\,\mathrm{Mpc}^{-1}$ corresponds roughly to the performance of current analyses, while $k_{max} \sim 0.2$ $h\,\mathrm{Mpc}^{-1}$ is more of a stretch goal for the DESI era (some improvement over current analysis can be expected simply by going to higher redshift where the non-linear scale is smaller).

The redshift-space distortions can effectively constrain two parameter combinations, $b(z)\sigma(z)$ and $f(z)\sigma(z)$, where $\sigma(z) \propto P_{\mathrm{mass}}^{1/2}(z, k)$ is the RMS normalization of the linear mass density fluctuations as a function of z. In Table 2.3, we quote projected constraints on $f\sigma$ for different maximum k assumptions e.g., $f\sigma_{0.1}$ means the error calculation included information up to $k_{max} = 0.1$ $h\,\mathrm{Mpc}^{-1}$. These fractional errors are equivalent to what one usually sees quoted as an error on "$f\sigma_8$". The $f\sigma_k$ precision we project for DESI, aggregated over all redshifts, is $\sim 0.74\%$ for $k_{max} = 0.1 h\,\mathrm{Mpc}^{-1}$, or $\sim 0.38\%$ for $k_{max} = 0.2 h\,\mathrm{Mpc}^{-1}$.

2.4.2 Baseline Survey

Our baseline assumption for science projections is that DESI runs over an approximately five-year period covering 14,000 deg^2 in area. DESI will target four types of objects: Bright Galaxies (BGS), Luminous Red Galaxies (LRGs), Emission Line Galaxies (ELGs) [101], and quasars. Details on how these objects are targeted can be found in Section 3. In what follows, most calculations are done for this baseline survey. We additionally provide several relevant calculations for the required minimum survey with the same target number densities over 9,000 instead of 14,000 deg^2 in area.

The number densities used here, plotted in Figure 2.6, are based on the selection criteria for each object type described in the following chapter.

We assume fiducial biases follow constant $b(z)D(z)$, where $D(z)$ is the linear growth factor normalized by $D(z = 0) \equiv 1$. For LRGs we use $b_{\mathrm{LRG}}(z)D(z) = 1.7$. For ELGs we use $b_{\mathrm{ELG}}(z)D(z) = 0.84$ [101]. For quasars we use $b_{\mathrm{QSO}}(z)D(z) = 1.2$ (loosely based on [102]). For the BGS, we use $b_{\mathrm{BGS}}(z)D(z) = 1.34$, but the results are insensitive to this value because of the much higher number density in most of the BGS volume. Note that these forms keep the observed clustering amplitude of each individual tracer constant with redshift, in agreement with observations (more detailed references for bias evolution are given below, in sections 3.1, 3.2, 3.3.1, and 3.4.1 for BGS, LRGs, ELGs, and QSOs, respectively).

The signal-to-noise for typical BAO-scale modes in redshift space is shown in Figure 2.7, along with the same quantity computed for several other experiments for comparison [95].

We evaluate $\bar{n}P$ at $k = 0.14$ $h\,\mathrm{Mpc}^{-1}$, $\mu = 0.6$, an approximate center-of-weight point for BAO measurements. We chose these values by looking for the point where $\bar{n}P = 1$ corresponded to the optimum in a trade-off between area and number density at fixed total number of objects (specifically, for the full range of parameters covered by DESI LRGs and ELGs). This definition reflects the origin of the idea that $\bar{n}P = 1$ is a special point, but it should be kept in mind that achieving $\bar{n}P$ by this definition does leave a survey significantly farther away from the sample variance limit than the traditional definition $k = 0.2$ $h\,\mathrm{Mpc}^{-1}$, $\mu = 0$.
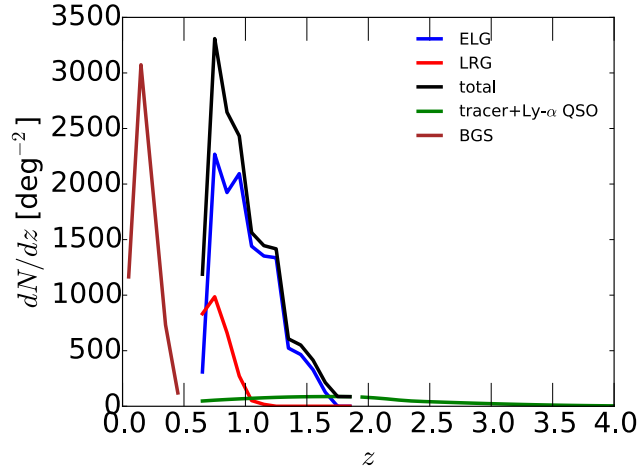
Figure 2.6: DESI number densities, per unit z, per square degree, used in cosmology projections (Table 2.3 and 2.7).
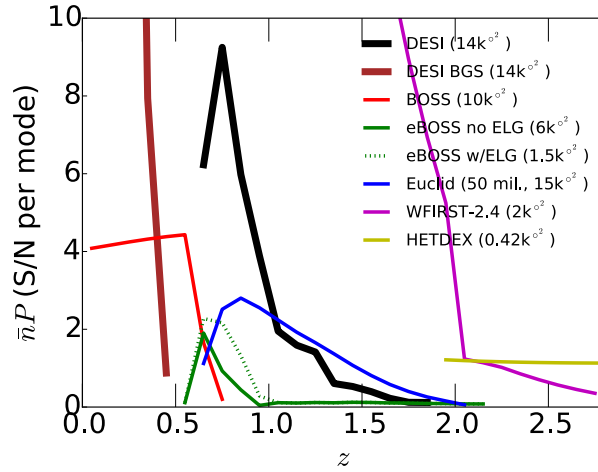
Figure 2.7: Signal to noise comparison of the DESI galaxy survey against other precursor (Stage II and Stage III) and upcoming (Stage IV) spectroscopic surveys. Shown is $\bar{n}P(k = 0.14\,h\,\mathrm{Mpc}^{-1}, \mu = 0.6)$. The DESI forecasts do not include the Ly-α forest contribution. Including this would give an effective $\bar{n}P \sim 0.3$ at $z \sim 2.5$. Note that the large area covered by DESI provides an advantage reflected in Figure 2.9.
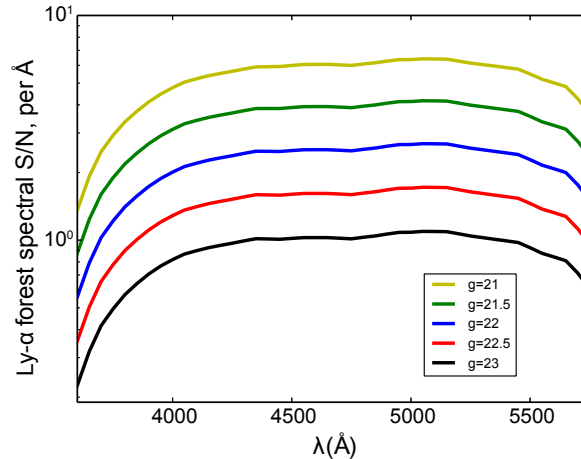
Figure 2.8: Signal-to-noise ratio per Å used for DESI quasar spectra (detector noise, not absorption noise), for different g magnitudes, accounting for mean Ly-α forest absorption.
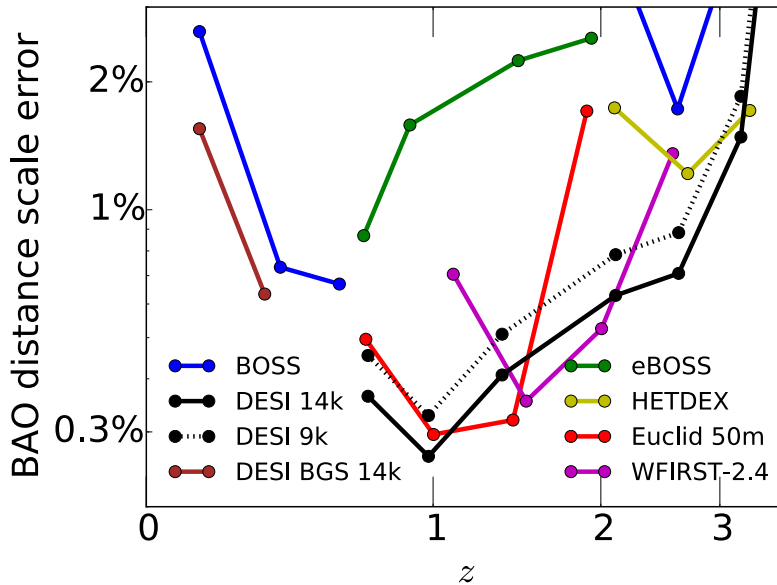
Figure 2.9: The fractional error on the dilation factor, R, as a function of redshift presented in comparable bins for DESI, BOSS, *Euclid*, *WFIRST*, HETDEX, and eBOSS. This gives an indicative error on distance measurements to each redshift. The forecasts for a 14,000 deg^2 DESI Bright Galaxy Survey (BGS) are also shown. DESI will provide the best measurements over much of the region and is competitive with space-based missions, which will come later. We use 50 million total galaxies for Euclid, following their Definition Study Report [104], although it has been suggested that this may be optimistic [105].

The spectral signal-to-noise ratio that we use, computed using the `bbspecsim` code [103], is shown in Figure 2.8.

2.4.3   Summary of Forecasts

Table 2.3 lists the basic galaxy and quasar BAO distance measurement projections, and RSD $f(z)\sigma_8(z)$ error projections for two different k_{max} values for our baseline 14K survey. We provide the same set of calculations in Table 2.4 for our threshold 9K survey. Tables 2.5 and 2.6 shows the projections for the Bright Galaxy Survey for 14K and 9K square degrees, respectively. Table 2.7 lists the Ly-α forest BAO distance measurement projections, including cross-correlations with quasars in the same redshift range for a $z > 1.9$ Ly-α forest survey; Table 2.8 presents the same calculations for the threshold 9K survey. The BAO errors are also shown in Figure 2.9, along with those from other experiments for comparison (see [95] for a description of the other experiments).

DESI will provide high precision measurements of the Universe's expansion rate over billions of years. Using the Ly-α forest technique, coverage will include the early times when the expansion rate was decreasing (when the matter density, not the dark energy density, was controlling the rate). In Figure 2.10 we show how DESI will improve these measurements over those existing today.

Table 2.9 shows Dark Energy Task Force (DETF) Figures of Merit (FoMs) [4]. For the common normalization convention that we follow, the FoM is simply $\left(\sigma_{w_p}\sigma_{w'}\right)^{-1}$ where $w(z) = w_p+(a_p-a)w'$ and a_p is chosen to make the errors on w_p and w' independent. Because the DETF FoM model is defined to include the possibility of curvature, we include curvature projections in Table 2.9. The figure of merit results are reflected in Figure 2.11.

Importantly, Table 2.9 shows that these surveys exceed the Stage IV FoM threshold. We take this to be a value of 110, based on a 10-fold improvement of the value of 11 from [109]. This

Table 2.3: Summary of forecasted constraints achievable by DESI, covering 14,000 deg^2. Indications of signal to noise, nP, are given at two values of $k, \mu = \{0.2\ h\,\mathrm{Mpc}^{-1}, 0\}$ and $\{1.4\ h\,\mathrm{Mpc}^{-1}, 0.6\}$. The fractional error on the normalization of $f(z)P^{1/2}(k, z)$ is $\sigma_{f\sigma_k}/f\sigma_k$, assuming known shape of the power spectrum and known geometry, using $k_{\max} = k\ h\,\mathrm{Mpc}^{-1}$. The dilation factor R is defined to be a parameter rescaling the radial and transverse distances by equal factors.

z	$\frac{\sigma_{R/s}}{R/s}$ %	$\frac{\sigma_{D_A/s}}{D_A/s}$ %	$\frac{\sigma_{Hs}}{Hs}$ %	$\bar{n}P_{0.2,0}$	$\bar{n}P_{0.14,0.6}$	V $[h^{-1}\mathrm{Gpc}^3]$	$\frac{dN_{ELG}}{dz\ d\mathrm{deg}^2}$	$\frac{dN_{LRG}}{dz\ d\mathrm{deg}^2}$	$\frac{dN_{QSO}}{dz\ d\mathrm{deg}^2}$	$\frac{\sigma_{f\sigma_{0.1}}}{f\sigma_{0.1}}$ %	$\frac{\sigma_{f\sigma_{0.2}}}{f\sigma_{0.2}}$ %
0.65	0.57	0.82	1.50	2.59	6.23	2.63	309	832	47	3.31	1.57
0.75	0.48	0.69	1.27	3.63	9.25	3.15	2269	986	55	2.10	1.01
0.85	0.47	0.69	1.22	2.33	5.98	3.65	1923	662	61	2.12	1.01
0.95	0.49	0.73	1.22	1.45	3.88	4.10	2094	272	67	2.09	0.99
1.05	0.58	0.89	1.37	0.71	1.95	4.52	1441	51	72	2.23	1.11
1.15	0.60	0.94	1.39	0.58	1.59	4.89	1353	17	76	2.25	1.14
1.25	0.61	0.96	1.39	0.51	1.41	5.22	1337	0	80	2.25	1.16
1.35	0.92	1.50	2.02	0.22	0.61	5.50	523	0	83	2.90	1.73
1.45	0.98	1.59	2.13	0.20	0.53	5.75	466	0	85	3.06	1.87
1.55	1.16	1.90	2.52	0.15	0.40	5.97	329	0	87	3.53	2.27
1.65	1.76	2.88	3.80	0.09	0.22	6.15	126	0	87	5.10	3.61
1.75	2.88	4.64	6.30	0.05	0.12	6.30	0	0	87	8.91	6.81
1.85	2.92	4.71	6.39	0.05	0.12	6.43	0	0	86	9.25	7.07

Table 2.4: Like Table 2.3, except with DESI covering only 9,000 deg^2.

z	$\frac{\sigma_{R/s}}{R/s}$ %	$\frac{\sigma_{D_A/s}}{D_A/s}$ %	$\frac{\sigma_{Hs}}{Hs}$ %	$\bar{n}P_{0.2,0}$	$\bar{n}P_{0.14,0.6}$	V $h^{-1}\mathrm{Gpc}^3$	$\frac{dN_{ELG}}{dz\ d\mathrm{deg}^2}$	$\frac{dN_{LRG}}{dz\ d\mathrm{deg}^2}$	$\frac{dN_{QSO}}{dz\ d\mathrm{deg}^2}$	$\frac{\sigma_{f\sigma_{0.1}}}{f\sigma_{0.1}}$ %	$\frac{\sigma_{f\sigma_{0.2}}}{f\sigma_{0.2}}$ %
0.65	0.71	1.02	1.87	2.59	6.23	1.69	309	832	47	4.12	1.96
0.75	0.59	0.86	1.58	3.63	9.25	2.03	2269	986	55	2.62	1.26
0.85	0.59	0.86	1.53	2.33	5.98	2.34	1923	662	61	2.64	1.26
0.95	0.61	0.91	1.52	1.45	3.88	2.64	2094	272	67	2.61	1.24
1.05	0.72	1.12	1.70	0.71	1.95	2.90	1441	51	72	2.79	1.39
1.15	0.75	1.17	1.74	0.58	1.59	3.14	1353	17	76	2.80	1.42
1.25	0.76	1.19	1.74	0.51	1.41	3.35	1337	0	80	2.81	1.44
1.35	1.15	1.87	2.52	0.22	0.61	3.54	523	0	83	3.62	2.16
1.45	1.22	1.99	2.66	0.20	0.53	3.70	466	0	85	3.82	2.34
1.55	1.45	2.37	3.14	0.15	0.40	3.84	329	0	87	4.40	2.84
1.65	2.20	3.59	4.74	0.09	0.22	3.95	126	0	87	6.36	4.50
1.75	3.59	5.79	7.86	0.05	0.12	4.05	0	0	87	11.11	8.49
1.85	3.64	5.87	7.97	0.05	0.12	4.13	0	0	86	11.53	8.82

Table 2.5: Like Table 2.3, except for the DESI Bright Galaxy Survey, covering 14,000 deg^2.

z	$\frac{\sigma_{R/s}}{R/s}$ %	$\frac{\sigma_{D_A/s}}{D_A/s}$ %	$\frac{\sigma_{Hs}}{Hs}$ %	$\bar{n}P_{0.2,0}$	$\bar{n}P_{0.14,0.6}$	V $[h^{-1}\mathrm{Gpc}^3]$	$\frac{dN_{BGS}}{dz\ d\mathrm{deg}^2}$	$\frac{\sigma_{f\sigma_{0.1}}}{f\sigma_{0.1}}$ %	$\frac{\sigma_{f\sigma_{0.2}}}{f\sigma_{0.2}}$ %
0.05	4.33	6.12	12.10	146.60	352.91	0.04	1165	33.24	14.08
0.15	1.66	2.35	4.66	59.47	144.69	0.23	3074	12.47	5.25
0.25	1.07	1.51	2.97	14.84	36.43	0.58	1909	7.69	3.25
0.35	0.91	1.32	2.44	3.21	7.94	1.04	732	5.83	2.60
0.45	1.56	2.39	3.69	0.35	0.87	1.55	120	6.35	3.77

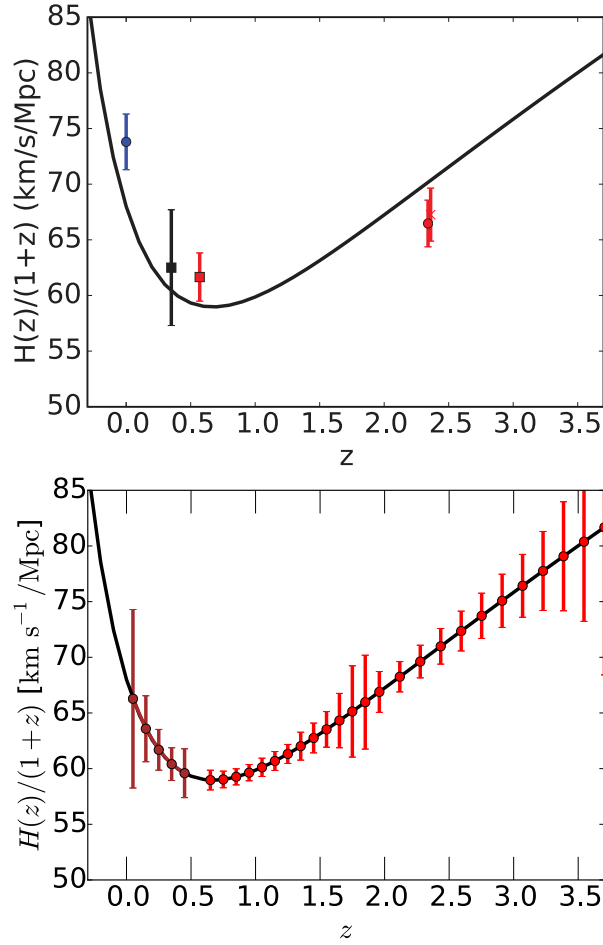**Table 2.6:** Like Table 2.5, but for a 9,000 deg^2 Bright Galaxy Survey.

z	$\frac{\sigma_{R/s}}{R/s}$ %	$\frac{\sigma_{D_A/s}}{D_A/s}$ %	$\frac{\sigma_{Hs}}{Hs}$ %	$\bar{n}P_{0.2,0}$	$\bar{n}P_{0.14,0.6}$	V $[h^{-1}\mathrm{Gpc}^3]$	$\frac{dN_{BGS}}{dz\ d\mathrm{deg}^2}$	$\frac{\sigma_{f\sigma_{0.1}}}{f\sigma_{0.1}}$ %	$\frac{\sigma_{f\sigma_{0.2}}}{f\sigma_{0.2}}$ %
0.05	5.39	7.63	15.09	146.60	352.91	0.02	1165	41.46	17.56
0.15	2.07	2.93	5.81	59.47	144.69	0.15	3074	15.55	6.54
0.25	1.33	1.89	3.70	14.84	36.43	0.38	1909	9.59	4.05
0.35	1.14	1.64	3.04	3.21	7.94	0.67	732	7.27	3.24
0.45	1.94	2.98	4.60	0.35	0.87	1.00	120	7.92	4.71

Table 2.7: $z > 1.9$ Ly-α forest quasar survey, over 14000 sq. deg. Parameter errors are in percent relative to the BAO scale, s.

z	$\frac{\sigma_{R/s}}{R/s}$ (%)	$\frac{\sigma_{D_A/s}}{D_A/s}$ (%)	$\frac{\sigma_{Hs}}{Hs}$ (%)	$\frac{dN_{QSO}}{dz\ d\mathrm{deg}^2}$
1.96	1.43	2.69	2.74	82
2.12	1.02	1.95	1.99	69
2.28	1.09	2.18	2.11	53
2.43	1.20	2.46	2.26	43
2.59	1.34	2.86	2.47	37
2.75	1.53	3.40	2.76	31
2.91	1.81	4.21	3.18	26
3.07	2.16	5.29	3.70	21
3.23	2.75	7.10	4.57	16
3.39	3.86	10.46	6.19	13
3.55	5.72	15.91	8.89	9
3.70	-	-	-	7
3.86	-	-	-	5
4.02	-	-	-	3

Table 2.8: Like Table 2.7, except with DESI covering only 9,000 deg^2.

z	$\frac{\sigma_{R/s}}{R/s}$ (%)	$\frac{\sigma_{D_A/s}}{D_A/s}$ (%)	$\frac{\sigma_{Hs}}{Hs}$ (%)	$\frac{dN_{QSO}}{dz\ d\mathrm{deg}^2}$
1.96	1.78	3.35	3.42	82
2.12	1.27	2.43	2.48	69
2.28	1.37	2.72	2.63	53
2.43	1.49	3.07	2.82	43
2.59	1.67	3.57	3.08	37
2.75	1.91	4.24	3.44	31
2.91	2.25	5.26	3.96	26
3.07	2.69	6.60	4.62	21
3.23	3.43	8.86	5.70	16
3.39	4.81	13.05	7.72	13
3.55	7.14	19.85	11.09	9
3.70	-	-	-	7
3.86	-	-	-	5
4.02	-	-	-	3

Figure 2.10: Expansion rate of the Universe as a function of redshift. In the upper plot, the filled blue circle is the H_0 measurement of [106], the solid black square shows the SDSS BAO measurement of [107], the red square shows the BOSS galaxy BAO measurement of [6], the red circle shows the BOSS Ly-α forest BAO measurement of [47], and the red x shows the BOSS Ly-α forest BAO-quasar cross-correlation measurement of [108]. The lower plot shows projected DESI points.
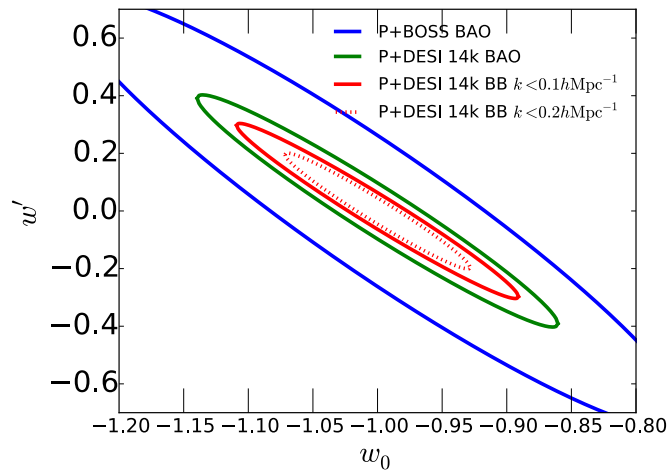
Figure 2.11: The $w_0 - w_a$ plane showing projected limits (68%) from DESI using just BAO and using the broadband (BB) power spectrum. Also shown is the limit from BOSS BAO. *Planck* priors are included in all cases, and DESI includes the BGS and non-redundant part of BOSS. The figure of merit of the surveys is inversely proportional to the areas of the error ellipses.

Table 2.9: DETF Figures of Merit and uncertainties σ_{w_p} and σ_{Ω_k}. σ_{w_p} is the error on w at the pivot redshift, which also equal to the error on a constant w holding $w_a = 0$. σ_{Ω_k} is the error on the curvature of the Universe, Ω_k. All DESI lines contain the BGS, and BOSS in the range $0.45 < z < 0.6$ that does not substantially overlap with DESI. All cases include *Planck* CMB constraints. The pivot point, where $w(a)$ has minimal uncertainty is indicated by a_p. We note that a FoM of 110 is 10 times the Stage II level of [109], which we take to be the definition of Stage IV. DESI BAO galaxy exceeds this threshold even with a 9,000 square degree survey.

Surveys	FoM	a_p	σ_{w_p}	σ_{Ω_k}
BOSS BAO	37	0.65	0.055	0.0026
DESI 14k galaxy BAO	133	0.69	0.023	0.0013
DESI 14k galaxy and Ly-α forest BAO	169	0.71	0.022	0.0011
DESI 14k BAO + gal. broadband to $k < 0.1\ h\ \mathrm{Mpc}^{-1}$	332	0.74	0.015	0.0009
DESI 14k BAO + gal. broadband to $k < 0.2\ h\ \mathrm{Mpc}^{-1}$	704	0.73	0.011	0.0007
DESI 9k galaxy BAO	95	0.69	0.027	0.0015
DESI 9k galaxy and Ly-α forest BAO	121	0.71	0.026	0.0012
DESI 9k BAO + gal. broadband to $k < 0.1\ h\ \mathrm{Mpc}^{-1}$	229	0.73	0.018	0.0011
DESI 9k BAO + gal. broadband to $k < 0.2\ h\ \mathrm{Mpc}^{-1}$	502	0.73	0.013	0.0009

is the same Stage IV definition that LSST used in their Conceptual Design Report. The 9,000 square degrees DESI survey achieves 121 with galaxies and Ly-α forest BAO. We note that these computations include only BAO and CMB, without even the Stage II Supernovae Ia results from [109]. Including DESI galaxy broadband clustering or other dark energy probes boost the Figure of Merit well above 110.

As this 9000 square degree survey forecast meets the Stage IV threshold and hence the Mission Need, we have adopted it as the quantitative basis for the Level 1 Science Requirement for the DESI project. We aggregate the BAO performance into three redshift ranges, R in $0.0 < z < 1.1$ and $1.1 < z < 1.9$ and H in $1.9 < z < 3.7$, for the L1 requirements, so as to leave flexibility in the exact redshift distribution of targets. An extensive discussion of how the FOM depends on variation in survey parameters was presented in the DESI Conceptual Design Review.

The measurements of $f\sigma_8$ from redshift-space distortion provide the means for testing General Relativity. Figure 2.12 shows the rate of growth of structure, f, as a function of the redshift. Forecasted DESI errors, assuming information at $k < 0.2\ h\,\mathrm{Mpc}^{-1}$, are shown on the ΛCDM curve. Alternative gravity models generically predict scale-dependent growth, and here we show theoretical expectations for the $f(R)$ modified theory of gravity evaluated at two scales (two values of k), as well as predictions for the DGP braneworld theory. DESI can clearly distinguish between these models.

2.4.4 Forecasting Details

Galaxy and Quasar Clustering

Our treatment of isolated galaxy BAO follows [99], assuming 50% reconstruction, i.e., reduction of the BAO damping scale of [99] by a factor 0.5, except at very low number density, where we degrade reconstruction based on [110].

Bias uncertainty is modeled by a free parameter in each redshift bin, generally of width $\Delta z = 0.1$, for each type of galaxy. Our results are not sensitive to the redshift bin width [95]. For the broadband signal, we use the same information damping factors from [99] as we use for BAO. This is well-motivated from a theoretical point of view as the non-linear clustering suppresses all linear
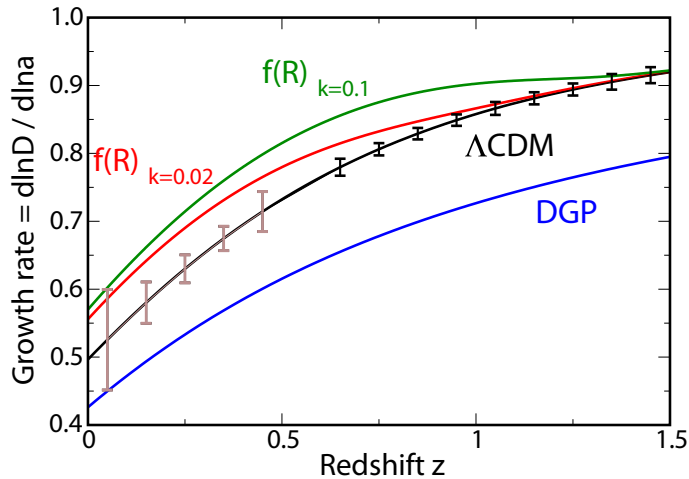
Figure 2.12: Growth of structure, f, as a function of redshift, showing projected DESI measurements and their ability to discriminate against alternative gravity models, $f(R)$ (whose scale-dependent growth we show evaluated at two different scales) and DGP. The brown (light) error bars at $z < 0.5$ correspond to DESI Bright Galaxy Survey; these are expected to improve when information from the multiple tracers in the BGS is included. Adopted from the Snowmass report on the growth of cosmic structure [64].

theory information, not just BAO [19]. We also include the reconstruction factor (50% reduction in damping length), assuming that reconstruction will recover non-BAO information as well. See [95] for more discussion.

Ly-α Forest

DESI will also probe large-scale structure using the Ly-α forest [111, 43], i.e., the Ly-α absorption by neutral gas in the intergalactic medium in the spectra of high redshift quasars (it may be possible to do even better at faint magnitudes using Lyman-break galaxies [41]). The distribution of intergalactic gas can be used as a complementary tracer to galaxies of the underlying matter distribution for BAO and broadband power spectrum characteristics.

The constraints from the Ly-α forest are difficult to predict accurately, because they require careful simulation [112, 113]. The forecasts described below we believe are a conservative assessment. We limit the application of Ly-β forest data to BAO only (see below), and do not include cross-correlations with quasar density, nor statistics beyond the power spectrum, such as the bispectrum, which are known to be powerful for breaking IGM model degeneracies (e.g., [114]). Finally, we only use the redshift range $z = 2 - 2.7$.

We model the three dimensional power spectrum of Ly-α using Eq. (2.15) and, except as otherwise noted, we use the method of [41] to estimate the errors obtainable by DESI. We use Table I of [37] to model the dependence of b, β, and fitting parameters of D. While these are primarily valid near $z \approx 2.25$, for BAO the model dependence is not significant. For broadband spectra constraints the bias and damping parameters depend on the amplitude and slope of the linear power spectrum, temperature-density relation [115], and mean level of absorption [116], all of which are varied in our Fisher matrix calculations. To help constrain these parameters, we include the one-dimensional power spectrum, which could be measured from the hundreds of existing high resolution spectra [116, 117].

While past projections used the rest wavelength range $1041 < \lambda < 1185$ Å (following [111]), for the BAO constraints only, we expand the range to include the Ly-β forest and move slightly closer to the quasar, $985 < \lambda < 1200$ Å, reflecting our increasing confidence that we understand the relevant issues well enough to measure BAO across this range [118]. (The Ly-β forest is the wavelength range $\sim 973 - 1026$Å where there is Ly-β absorption on top of the Ly-α absorption. This Ly-β absorption corresponds to the same gas we see in the standard Ly-α forest and should provide some extra information, but we simply assume it can be mostly removed as a source of noise and the underlying Ly-α used to measure BAO to shorter wavelengths in each quasar spectrum.) Gains from this enhancement of effective number density (and cross-correlations with quasars) are substantial because the measurement is quite sparse, i.e., in what for galaxies we would call the shot-noise limited regime.

The cross-correlation of quasars with the Ly-α forest [119] provides a complementary measurement of BAO at high redshift. We combine the two probes of structure in the same volume as described in [95]. The correlation of Ly-α absorption in quasar spectra can also provide other cosmological information, beyond BAO: cosmological parameter constraints from the line of sight power spectrum [111, 120, 121, 122], and from the full shape of the three-dimensional clustering [37]. In the projections below we distinguish between Ly-α forest BAO measurements and broadband measurements that include the one-dimensional power spectrum measurement.

2.5 Cosmology Beyond Dark Energy

While the fundamental goal of DESI is the measurement of the expansion rate of the Universe through BAO and RSD, the enormous spectroscopic survey will measure the two-point correlation function and power-spectrum over a broad range of scales and redshifts. These data will open up broader investigations into cosmology and particle physics.

The broadband power spectrum will provide tests of inflation through its scale dependence. Inflation can also be tested through the scale dependence of the bias of dark matter halos, which constrains the primordial non-Gaussianity. The power spectrum will also reflect the damping of structure by free-streaming neutrinos and thereby give a measure of the sum of the neutrino masses, and possibly reveal previously unknown nearly massless species.

2.5.1 Inflation

The inflationary paradigm is the leading explanation for the origin of the fluctuations of primordial density, which in turn seeded the large-scale structure we observe today. In its simplest formulation, inflation predicts perturbations in the initial distribution that are very nearly scale-independent and Gaussian-distributed about the mean. Inflation has been tested primarily with the CMB observations — starting with *COBE* measurements on large scales in the early 1990s and continuing with the increasingly precise *WMAP* and *Planck* measurements in this millennium. However the CMB temperature measurements are not expected to improve greatly after *Planck* (though CMB polarization has a lot to offer, in particular in testing for signatures of inflationary gravity waves). Large-scale structure measurements have become increasingly precise thanks to 2dF, SDSS, and WiggleZ. These complement the CMB measurements in temporal and spatial scales. The next frontier for tests of inflation is large-scale structure. DESI's unparalleled three-dimensional picture of the evolution of structure will contribute powerfully.

Spectral Index and Its Running

Inflation predicts that the primordial spectrum of density fluctuations is nearly a power law in wavenumber k. The power law is specified by the spectral index defined as

$$n_{\rm s}(k_0) = \left. \frac{d \ln P}{d \ln k} \right|_{k_0} \tag{2.16}$$

where k_0 is some reference scale, typically chosen to be $k_0 = 0.05 \, {\rm Mpc}^{-1}$. A perfect power law would correspond to a constant n_s; in reality, inflation also predicts a small "running" with wavenumber parameterized with the parameter $\alpha = dn_{\rm s}/d \ln k$, again defined at k_0. The primordial power spectrum can therefore be written as [123]

$$P(k) = P(k_0)(k/k_0)^{n_{\rm S}(k_0) + \frac{1}{2} \alpha \ln(k/k_0)}. \tag{2.17}$$

The exact Harrison-Zel'dovich primordial spectrum has $n_{\rm s} = 1$, while inflation predicts slight deviations from unity. Ruling out $n_{\rm s} = 1$ at a significant level of confidence would strengthen the case for inflation [124]. Recent *Planck* data currently favor $n_{\rm s} < 1$ at 5σ; $n_{\rm s} = 0.968 \pm 0.006$ [125]. The current limit on running of the spectral index obtained by *Planck* is $dn_{\rm s}/d \ln k = -0.003 \pm 0.007$ (95% CL). Because it is in the regime of linearity for a wide range of k, the Ly-α forest is an excellent complementary probe of α_s.

In Table. 2.10 we present forecasts on inflationary observables obtained with the Fisher-matrix formalism described in Section 2.4.1, applied to the power spectrum obtained from DESI galaxies,

Table 2.10: Projected constraints on inflationary observables obtained by DESI. In all cases, we include constraints from the *Planck* satellite and BAO information from DESI galaxies, quasars and the Ly-α forest. We show the result of including information from the broadband galaxy power spectrum ("Gal") out to $k_{\max} = 0.1$ and $0.2\ h\,\mathrm{Mpc}^{-1}$, and from the Ly-$\alpha$ forest. The numbers in parentheses show the relative improvement over *Planck*. Broadband Ly-α forest constraints include ~ 100 existing high resolution spectra to constrain the IGM model. n_s constraints assume fixed α_s. Both constraints are marginalized over Σm_ν, and the fiducial values are $n_s = 0.963$, $\alpha_s = 0$.

Data	$\sigma_{n_{\mathrm{s}}}$	$\sigma_{\alpha_{\mathrm{s}}}$
Gal ($k_{\max} = 0.1 h\,\mathrm{Mpc}^{-1}$)	0.0025 (1.3)	0.005 (1)
Gal ($k_{\max} = 0.2 h\,\mathrm{Mpc}^{-1}$)	0.0022 (1.5)	0.004 (1.3)
Ly-α forest	0.0029 (1.1)	0.0027 (1.9)
Ly-α forest + Gal ($k_{\max} = 0.2$)	0.0019 (1.7)	0.0019 (2.7)

quasars, and Ly-α forest, combined with CMB data from the *Planck* satellite. The table shows strong constraints on n_{s}, and improvements up to a factor of three over *Planck* alone, under the assumption that there is no significant running in the spectral index. Achieving these constraints will require excellent control of broad-band systematics in the Ly-α forest and galaxy analyses. But the effort is worthwhile, as these measurements can have far-reaching implications on our understanding of the very early Universe, as we now describe.

For the spectral index, the increased accuracy implies much better constraints on models of inflation. With the DESI+*Planck* constraints, excellent constraints on the spectral index will effectively reduce the allowed region in the plane of n_{s} and r, the ratio of tensor to scalar modes, to a vertical line pinned at the measured value of n_{s}. Combining these results with better measurements of the r from the small-scale CMB experiments will lead to much better constraints on inflationary models. Even without the accompanying r measurements, better determination of the spectral index is important: for example, for inflationary potentials $V(\phi) \propto \phi^m$, where ϕ is the inflaton field, the spectral index and the total number of e-folds of inflation N are related via $1 - n_{\mathrm{s}} = (m+2)/(2N)$ [126]. Hence, for this class of models the duration of the inflationary phase would be determined by DESI very precisely.

Implications of the precise measurements of the running of the spectral index α_{s} are even more impressive. In standard single-field slow-rolling inflationary models, the running of the spectral index is of the order $O((1 - n_s)^2) \sim 1 \times 10^{-3}$ if $n_s \sim 0.96$. This means that DESI will start to approach the region of expected detection in minimal inflationary models. More importantly, a detection of running *larger* than the slow-roll prediction would imply either that inflation involves multiple fields, or a breakdown of the slow roll approximation [127], or else that a non-canonical kinetic term is controlling inflationary dynamics [128]. *Any* detection of the running of the spectral index would represent a significant advance in our understanding of the physics of inflation.

Primordial non-Gaussianity

One of the fundamental predictions of the simplest inflationary models is that the density fluctuations in the early Universe that seeded large-scale structure were nearly Gaussian distributed. A single field slow-roll inflation with canonical kinetic energy and adiabatic vacuum predicts very small amount of non-Gaussianity. A violation of any of these conditions, however, may lead to large non-Gaussianity. A simple, frequently studied model is that of non-Gaussianity of the local type, $\Phi = \phi_G + f_{\mathrm{NL}}(\phi_G^2 - \langle \phi_G^2 \rangle)$, where Φ is the primordial curvature fluctuation and ϕ_G is a Gaussian random field. A detection of nonzero f_{NL} would rule out the simplest model of inflation, while a

non-detection at a level of $f_{\rm NL} < O(1)$ would rule out many of its alternatives.

The tightest existing upper limits on non-Gaussianity have been obtained from observations of the cosmic microwave background by the *Planck* experiment[129]. Recently, a number of inflationary models have been proposed which predict a potentially observable level of non-Gaussianity, these include those from fast-roll inflation [130, 131, 132, 133, 134], quasi-single field inflation [135, 136], warm inflation [137, 138], and non-Bunch-Davies or excited initial states [130, 139, 140, 141]. There are also hybrids of multi-field and non-slow-roll models [142, 143, 144], and the inclusion of isocurvature modes in the non-Gaussian correlations [145, 146, 147]. Improved limits on non-Gaussianity would rule out some of these models. Conversely, a robust detection of primordial non-Gaussianity would dramatically overturn the simplest model of inflationary cosmology, and provide information that would help us significantly improve our understanding of the nature of physical processes in the early Universe.

Until recently, the most powerful methods to place limits on $f_{\rm NL}$ were based on the bispectrum of the CMB. The constraints from CMB data have improved starting from $\sigma(f_{\rm NL}) \simeq 3000$ with *COBE* [148] to $\sigma(f_{\rm NL}) \simeq 20$ with *WMAP* [149], to the tight constraint of $\sigma(f_{\rm NL}) \simeq 5.8$ with *Planck*'s first year data [150] and finally to $\sigma(f_{\rm NL}) \simeq 5.0$ with the 2015 data from Planck [129]. It is therefore impressive and maybe even surprising that a powerful LSS survey such as DESI can provide comparable but highly complementary constraints to *Planck*. Moreover, as we now show, DESI and *Planck* in combination can provide very tight constraints on distinct *classes* of physically motivated inflationary models.
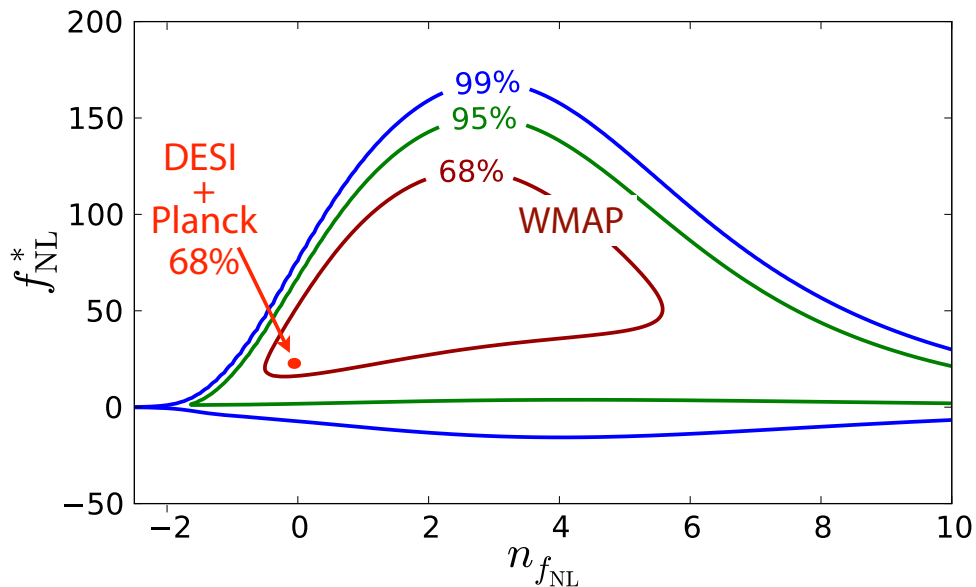
Powerful constraints on non-Gaussianity can come from the effect that it has on the clustering of dense regions on very large scales [151]. Essentially, the bias of dark matter halos assumes a unique, scale-dependent form at large spatial scales in the presence of primordial non-Gaussianity of local type

$$b(k) \equiv b_0 + \Delta b(k) = b_0 + f_{\rm NL}(b_0 - 1)\delta_c \, \frac{3\Omega_M H_0^2}{a \, g(a)T(k)c^2 k^2}, \qquad (2.18)$$

where b_0 is the usual Gaussian bias (on large scales, where it is constant), $f_{\rm NL}$ is the parameter that indicates departures from Gaussianity (when $f_{\rm NL} \neq 0$), $\delta_c \approx 1.686$ is the collapse threshold, $T(k)$ is the transfer function and $g(a)$ is the growth suppression factor. Notice the unique k^{-2} scale dependence in the presence of primordial non-Gaussianity. Since the bias $b(k)$ is readily measured from the correlation function of galaxies or quasars, classes of inflationary models can be tightly constrained. A first application of this method has been presented using the large-scale clustering of quasar and luminous red galaxies (LRG) galaxy data from the Sloan Digital Sky Survey (SDSS) [152]. The result, a non-detection with one sigma error $\sigma(f_{\rm NL}) \simeq 25$, was (at the time) comparable to the CMB constraints from *WMAP*. DESI will provide constraints competitive, and very complementary, to those from *Planck*, provided that we have systematics under control [153, 154, 155]

Forecasts for DESI indicate that the 1σ error on the local model from DESI alone will be $\sigma(f_{\rm NL}) \simeq 5$, and about a factor of two better when combined with the final *Planck* temperature and polarization data. From the fundamental physics point of view, these constraints are very exciting, as they probe not only primordial non-Gaussianity but are likely to detect the additional non-Gaussian signal due to late-time nonlinear interactions of the photon-baryon fluid with gravity (with $f_{\rm NL}{}^{\rm late} \simeq$ few [156, 157]), and thus provide an additional test of cosmology.

More generally, inflationary models predict a range of possibilities for the scaling of the bias $\Delta b \propto k^{-m}$. For example, $m = 2$ for the local model parameterized by $f_{\rm NL}$ as in Eq. (2.18); multi-field inflationary models generically produce $0 < m \lesssim 2$, and models with modifications to the initial quantum state can produce an even stronger scaling with $m = 3$. Because many of these

Figure 2.13: Constraints on the models of primordial non-Gaussianity with "running", where the usual parameter f_{NL} is promoted to a power-law function of wavenumber, $f_{NL}(k) = f_{NL}^*(k/k_*)^{n_{f_{NL}}}$. The larger contours show constraints on f_{NL}^* and $n_{f_{NL}}$ from a first analysis that was applied to WMAP 7 data [158]. The size of the red dot shows the 68% C.L. forecast on the joint constraint expected from the combination of the DESI and full *Planck* data sets, based on projections in Ref. [159].

models therefore leave a strong imprint in the clustering of galaxies and quasars, DESI will be able to strongly constrain whole classes of inflationary models. We show an illustration in Figure 2.13, where we present constraints on the models with "running" of non-Gaussianity, where the usual parameter f_{NL} now runs with wavenumber, $f_{NL}(k) = f_{NL}^*(k/k_*)^{n_{f_{NL}}}$. The larger contours show constraints on f_{NL}^* and $n_{f_{NL}}$ from a first analysis that was applied to WMAP 7 data [158], while the small, red contour shows the 68% C.L. forecast on the joint constraint expected from the combination of the DESI and full Planck data sets, based on projections in Ref. [159]. The latter constraint will shrink the area in the $f_{NL}^* - n_{f_{NL}}$ plane by about a factor of 100.

To achieve such excellent constraints, the galaxies measured in DESI must have sufficiently large bias, since only for biased tracers is the non-Gaussian scale-dependent clustering revealed. One way to further improve the errors is by combining two tracers of LSS, one with a high bias and one with a low bias. In this case it may possible to cancel sampling variance, which is the dominant source of error on large scales [160, 161], but due to low number density this will have to include an additional tracer of structure, potentially combining with the LSST and DES data.

More detailed studies of halo mass distribution of BOSS galaxies, combined with numerical simulations of non-Gaussian models [162] as well as studies of how to mitigate the large-angle systematic errors [163, 164, 155] are needed to provide a better definition of the ultimate reach of DESI for non-Gaussianity studies. However it seems certain that DESI constraints will be at least comparable to the best limits from CMB and that they will provide an excellent temporal and spatial complement to the latter.

Table 2.11: Constraints on the sum of neutrino masses from DESI forecasts in combination with constraints from the *Planck* satellite. The experiment combinations are identified as described in the caption of Table 2.10. The last four cases include the information from *Planck* and DESI BAO measurements. Fiducial values are $\Sigma m_\nu = 0.06$ eV, $N_{\nu,\text{eff}} = 3.04$. Σm_ν constraints assume fixed N_ν, while N_ν is marginalized over Σm_ν.

Data	$\sigma_{\Sigma m_\nu}$ [eV]	$\sigma_{N_{\nu,\text{eff}}}$
Planck	0.56	0.19
Planck + BAO	0.087	0.18
Gal ($k_{\max} = 0.1h\,\text{Mpc}^{-1}$)	0.030	0.13
Gal ($k_{\max} = 0.2h\,\text{Mpc}^{-1}$)	0.021	0.083
Ly-α forest	0.041	0.11
Ly-α forest + Gal ($k_{\max} = 0.2$)	0.020	0.062

2.5.2 Neutrinos

The effects of neutrinos in cosmology are well understood (for a review, see [165]). They decouple from the cosmic plasma when the temperature of the Universe is about 1 MeV, just before electron-positron annihilation. While ultra-relativistic, they behave as extra radiation (albeit not electromagnetically coupled) with a temperature equal to $(4/11)^{1/3}$ of the temperature of the cosmic microwave background. As the Universe expands and cools, they become non-relativistic and ultimately behave as additional dark matter.
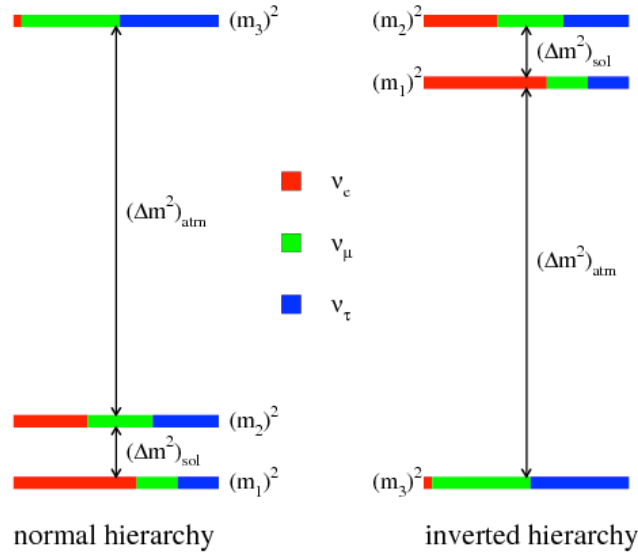
Neutrino Mass

The mass of neutrinos has two important effects in the Universe [165]. First, as the neutrinos become non-relativistic after the time of CMB decoupling they contribute to the background evolution in the same way as baryons or dark matter, instead of becoming completely negligible as they would if massless (like photons). This affects anything sensitive to the background expansion rate, e.g., BAO distance measurements. Second, the process of neutrinos becoming non-relativistic imprints a characteristic scale in the power spectra of fluctuations. This is termed the 'free-streaming scale' and is roughly equal to the distance a typical neutrino has traveled while it is relativistic. Fluctuations on smaller scales are suppressed by a non-negligible amount, of the order of a few percent. This allows us to put limits on the neutrino masses.

From neutrino mixing experiments we know the differences of the squares of masses of the neutrino mass eigenstates. The splitting between the two states with similar masses is $\Delta m_{21}^2 = (7.50 \pm 0.20) \times 10^{-5}$ eV^2, while the splitting between the highest and lowest masses squared is $\Delta m_{32}^2 = 2.32^{+0.12}_{0.08} \times 10^{-3}$ eV^2. Two things are not known: the absolute mass scale, and whether the two states close together are more or less massive than the third state. In what is called the normal hierarchy, the close states are less massive. In this configuration, the lowest possible masses in eV are 0, 0.009, and 0.048, so the minimal sum of neutrino masses is 0.057 eV. In the inverted hierarchy, the minimal masses are 0, 0.048, and 0.049, for a total of 0.097 eV. This is shown in Figure 2.14.

Table 2.11 shows our projected Σm_ν constraints, obtained through Fisher matrix calculations as discussed above and in [95].

With a projected resolution of 0.020 eV, DESI will make a precision measurement of the sum of the neutrino masses independent of the hierarchy and therefore determine the absolute mass scale for neutrinos, a measurement that is otherwise very challenging. Furthermore, if the masses were

Figure 2.14: The two possible neutrino mass hierarchies. Also shown is what fraction of each mass eigenstate corresponds to a neutrino flavor eigenstate. DESI will be sensitive to the sum of the neutrino masses and possibly to the mass hierarchy.

minimal and the hierarchy normal, DESI would be able to exclude the inverted hierarchy at 2σ.

Dark Radiation (e.g., sterile neutrinos)

The other parameter relevant for neutrino physics is the effective number of neutrino species $N_{\nu,\text{eff}}$, which parameterizes the energy density attributed to any non-electromagnetically interacting ultrarelativistic species (including e.g. axions) in units of the equivalent of one neutrino species that fully decouples before electron-positron annihilation. Extra radiation shifts the redshift of matter radiation equality and changes the expansion rate during the CMB epoch, although it does not significantly affect the Universe at the epoch probed by DESI. The value for the standard cosmological model is $N_{\nu,\text{eff}} = 3.04^3$ [166]. The detection of any discrepancy from the expected value would be a truly major result, as it would indicate a sterile neutrino [167], a decaying particle [168], a nonstandard thermal history [169], or perhaps that dark energy does not fade away to $\sim 10^{-9}$ at the time of recombination as expected for the cosmological-constant model [170]. All of these possibilities represent important extensions of the standard cosmological model, and uncovering them would present a major advance of our understanding of the Universe. Our forecasts for this parameter are also shown in Table 2.11. Again we see that the effective number of neutrino species will be measured to $\sim 10\%$ or better, providing strong constraints on the alternative models involving extra sterile neutrinos, axions or partly thermalized species.

In Figure 2.15 we show the improvement in the measurement of several fundamental parameters from cosmology and neutrino physics. The standard is taken to be the results from BOSS together with *Planck*. Displayed is the ratio of the uncertainty from BOSS over the uncertainty from DESI, with *Planck* always included.

---

[3]The small increase with respect to $N_\nu = 3$ is due to the fact that some neutrinos are still coupled at the onset of electron-positron annihilation.
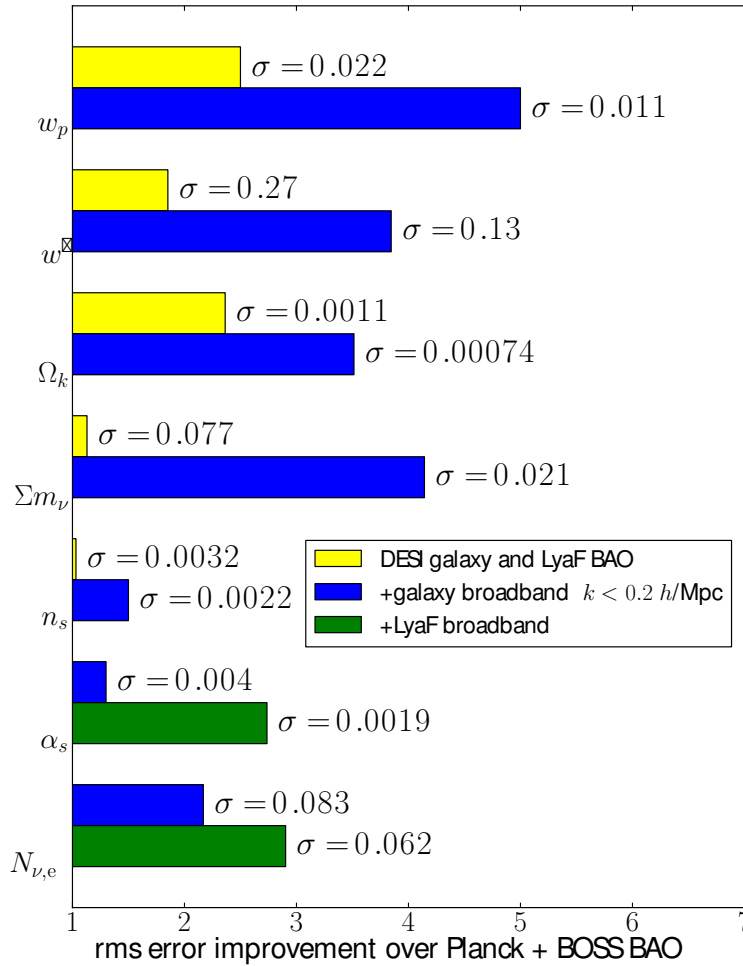
Figure 2.15: Improvement in the measurements of w_p, $w' = w_a$, Ω_k, $\sum m_\nu$ the sum of the neutrino masses, n_s the spectral index, α_s the running of the spectral index, and $N_{\nu,\text{eff}}$ the number of neutrino-like (relativistic) species.

2.6 The Milky Way Survey: Near-Field Cosmology from Stellar Spectroscopy

During conditions unusable for faint galaxy work, DESI will pursue the Bright Galaxy Survey, mapping 10 million galaxies to $z \sim 0.4$ in pursuit of the clustering analyses, such as from BAO and RSD, as described earlier in this chapter. As detailed in section 3.1, the areal density of these bright galaxies is comparable to the fiber density of DESI. Achieving a high completeness in the face of clustering and Poisson fluctuations requires multiple visits, leading to an excess of fibers compared to targets. Indeed, some fibers will be unable to reach a viable galaxy target even on the first pass, and this fraction increases on subsequent passes.

Bright stars are the natural secondary target, and we expect that any bright galaxy survey with the DESI fiber positioner will produce a very large sample of stars as a by-product. This sample is also of high science interest, leading to the definition of the Milky Way Survey. At 17th magnitude, even a short (8-10 min) DESI exposure measures an excellent spectrum with $S/N = 25$ per pixel, which will yield the radial velocity to a few km/s precision and the metallicity. We expect the BGS to generate at least 10 million such spectra. Spectroscopy of individual stars provides radial velocity, effective temperature, surface gravity, chemical abundance distribution, and approximate age. The assembly history of the Milky Way is encoded in the spatial distributions, kinematics, and chemical composition of the various distinct Galactic stellar populations. This information can test cosmological predictions for how galaxies like the Milky Way form and evolve on small scales that are difficult or impossible to test elsewhere in the Universe, and provide a critical test of the small-scale predictions of the ΛCDM model.

The European Space Agency *GAIA* satellite has been successfully launched and will provide a catalog of parallaxes, proper motions, and spectrophotometry for a billion point sources down to $V \sim 20$ over the whole sky. The satellite's RVS spectrograph will supplement those data with radial velocities for millions of brighter stars, although the flux limit is still under investigation due to higher than expected scattered light. DESI can substantially enhance the science return from *GAIA* by providing radial velocities and metallicities for stars much fainter than what the *GAIA* spectrograph can provide. While other projects are planned for spectroscopic follow-up of *GAIA* stars, DESI's higher multiplex, wide field of view, and extremely rapid reconfiguration give it a clear advantage.

The stellar program will put exceptional new constraints on the distribution of dark matter in the Milky Way, a vital measurement that links Galactic science, galaxy formation and cosmology. The Milky Way gravitational potential can be probed via the rotation of the Milky Way beyond 15 kiloparsecs, the motions of newly discovered tidal streams, and the kinematics of bright stars in the distant stellar halo. The uncertainty in the Milky Way mass, density profile, and internal structure currently are critically important systematics in the interpretation of direct and indirect dark matter searches, and the measurements possible with the stellar program will substantially reduce these uncertainties.

Joint metallicity and velocity distribution functions for stars far beyond the solar neighborhood will reveal the recent assembly history of the outer disk and vastly improve our understanding of the structure and formation of the thick disk. The first-ever deep spectroscopic survey of halo main-sequence turn-off stars to 30 kiloparsecs can be used to reconstruct the history of the Galaxy in its first two billion years and its interaction with other galaxies, shedding new light on enigmatic halo substructures like the Virgo overdensity and Hercules–Aquila cloud. Moreover, a survey of millions of stars will have huge potential for the discovery of kinematically and chemically peculiar stars in as-yet unexplored regions of the Galaxy.

2.7 Complementarity with Other Surveys

While DESI's spectroscopic survey will by itself yield incisive results in cosmology, its power is increased when combined with other experiments. DESI's BAO results are directly connected to CMB measurements via its dependence on the acoustic scale, but additional information can be obtained by directly cross-correlating the CMB with the density distribution and redshift space distortions from DESI. Large imaging surveys, including DES and LSST, will provide vast amounts of complementary data, allowing increased precision for both cosmological and neutrino measurements. This combination of imaging and spectroscopic surveys is particularly powerful for distinguishing dark energy from modified gravity models for cosmic acceleration.

2.7.1 Synergies with *Planck* and Future CMB Experiments

The cross-correlation of Planck and potential future CMB experiments, such as Advanced ACTPol and CMB-S4, with DESI enables cosmological measurements not possible with either individually, and opens up new opportunities to constrain fundamental physics, in the properties of dark energy and gravity discussed in 2.4 and the nature of neutrinos and inflation summarized in 2.5.

On large scales, cross-correlating CMB temperature fluctuations with the galaxy density field measures the Integrated Sachs-Wolfe effect, probing the time evolution of the gravitational potential and independently constraining dark energy [171]. The combination of CMB lensing and the foreground galaxies or quasars will also improve not only the signal-to-noise of CMB lensing leading to stronger cosmological constraints on the matter content, but also our understanding of the foreground tracers in large-scale structure, as lensing allows a clean measurement of the bias of the foreground sources.

The combination of CMB lensing and the RSD measurements from DESI will allow a probe of the two relativistic gravitational potentials independently (see e.g. [60] for an application of this test but for the case of gravitational lensing of background galaxies, not the CMB), testing the GR prediction of their equality over a wide redshift range [172]. CMB lensing and RSD measurements will also provide complementary constraints on the sum and differences of the neutrino masses, that in combination could help infer the neutrino hierarchy.

DESI will provide highly complementary constraints on inflation to those from *Planck* and a number of upcoming CMB small scale temperature and polarization experiments. An exciting realization in inflationary theory is that discerning the scale-dependence, or 'shape', of the bispectrum (the 3-point function) could provide a direct insight into the inflationary mechanism, through how non-Gaussianity is generated [173, 174]. CMB 3-point correlation measurements constrain a wide range of primordial bispectrum configurations, while DESI will provide more detailed information about the properties in the squeezed limit, a regime that could provide characteristic information about the underlying mechanism driving inflation e.g. whether it is multi-field, sourced from a non-Bunch Davies vacuum state, or includes non-trivial kinetic terms in the inflationary action.

Cross correlating the galaxy velocity field (inferred from the 3D density distribution) with the CMB will measure the kinetic Sunyaev-Zeldovich (kSZ) effect at the percent level. These measurements provide constraints on more exotic deviations from our standard cosmological models [175, 176, 177]. In addition, these measurements are astrophysically important since the kSZ effect is an unbiased probe of electrons and can be used to inventory the baryons in the Universe [178].

2.7.2 Synergies of DESI with DES and LSST

The massive spectroscopic survey provided by DESI will provide a unique and important complement to direct-imaging science projects currently being planned. We focus here on the Dark

Energy Survey (DES) and the Large Synoptic Survey Telescope (LSST), but DESI will complement other future imaging surveys in similar ways. Although both DES and LSST are located in the Southern Hemisphere, their planned surveys have overlap of a few thousand square degrees with the baseline DESI survey. In addition, only some of the cosmological tests described below rely on overlap between the photometric and spectroscopic surveys.

DESI can provide critical input into photometric redshifts which can help control the systematic uncertainty associated with cosmological measurements from photometric surveys like DES and LSST. For instance, cross correlation of photometric lensing sources with spectroscopic galaxy samples enable the reconstruction of the redshift distribution of the lensing sources [179, 171, 180, 181] providing a critical consistency test on the photometric redshifts used for cosmic shear and/or calibrating the mass of galaxy clusters for cluster abundance tests. Likewise, magnification-based lensing measurements of spectroscopic sources [182] can provide a consistency test for shape systematics and/or photometric redshift systematics in shear-based calibration of cluster masses.

Just as importantly, the combination of photometric and spectroscopic surveys is significantly more powerful than either set of surveys alone. An example is the utility of using galaxy-galaxy lensing, in which one uses the lensing of background galaxies by galaxies from the spectroscopic sample to measure the galaxy-mass cross-correlation of the spectroscopic sample. On small scales, this measures the properties of the host dark matter halo, testing galaxy bias models; on larger scales, it can be used to measure the mass-mass auto-correlation and hence the amplitude of structure [68, 183]. Several studies have forecast cosmological constraints from a combination of DES-like and DESI-like experiments [184, 185, 186, 187], and while the range of assumptions and forecasts varies from work to work, there is agreement that the combination of DES and DESI/LSST gives substantial benefits in terms of measured cosmological and non-cosmological parameters. This is particularly true within the context of modified gravity models, where the combination of surveys enables entirely new types of measurements that are ideally suited for addressing such questions. For instance, recent theoretical work suggests that comparing the shear field generated by galaxy clusters to the corresponding galaxy velocity can significantly improve current modified gravity constraints [188].

As an example of improvement in another type of constraint that can be achieved through the combination of DESI with imaging surveys, Figure 2.16 shows the joint constraint on the sum of the neutrino masses in eV against the dark energy density $\omega_{DE} = \Omega_{DE}h^2$ obtained by combining anticipated results for DESI BAO with LSST weak lensing. Similarly, Figure 2.17 shows prospective constraints in the Ω_m–Ω_Λ plane obtained by combining anticipated results for DESI BAO with LSST weak lensing (these forecasts assume the surveys are not overlapping on the sky, although it makes practically no difference [95, 189]).

Finally, DES and LSST will provide world-leading samples for supernova cosmology. The BAO and SNe Ia methods for measuring the cosmic distance scale are highly complementary: supernovae excel at low redshifts, where the SNe are brighter and where the BAO is more limited by cosmic variance due to the small cosmic volume. The combination of DESI with ground-based supernovae samples spanning from $z = 0$ to $z \approx 0.8$ will be a powerful view of the distance-redshift relation and the expansion history of the Universe. While we have focused on Figure of Merits drawn only from BAO and the DESI clustering samples, the inclusion of low to intermediate-redshift supernovae provides a notable improvement to current BAO constraints, as highlighted in numerous papers, such as [6, 190]. Essentially one is using BAO to calibrate the relative distance scale provided by the SNe. The redshift overlap of the two methods provides a further systematic cross-check. The exquisite precision of DESI at $z > 0.6$ will find an excellent partner in the DES and LSST supernova samples.

DESI will directly support the coming decade of supernova cosmology by providing spectroscopic
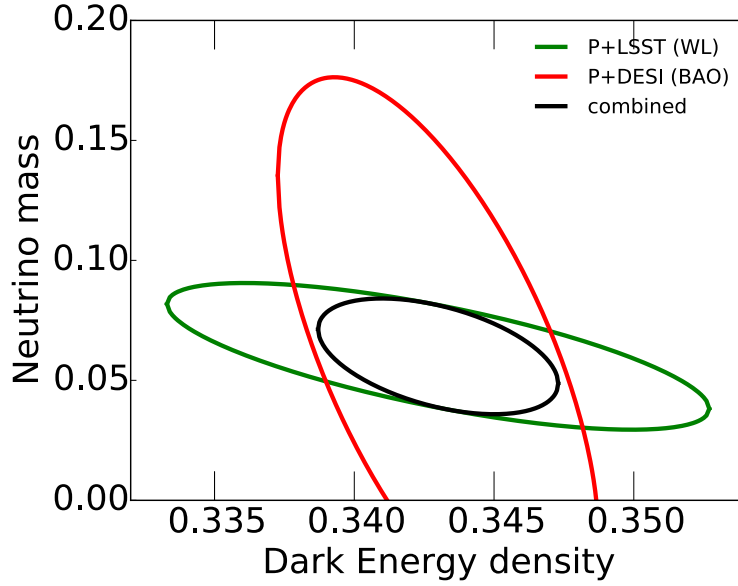
Figure 2.16: Constraint on the sum of the neutrino masses in eV against the dark energy density $\omega_{DE} = \Omega_{DE}h^2$ obtained by combining DESI BAO with LSST weak lensing, in each case including Planck CMB constraints. More powerful constraints are obtained when the full power spectrum from DESI is used. See Table 2.11.
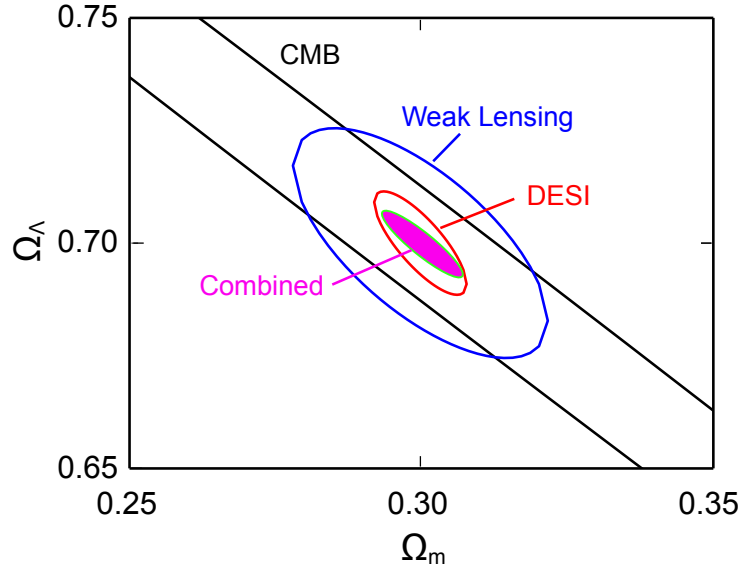
Figure 2.17: Prospective constraints in the Ω_m–Ω_Λ plane obtained by combining DESI BAO with LSST weak lensing. More powerful constraints are obtained when the full power spectrum from DESI is used. See Table 2.9.

redshifts for many tens of thousands of SNe host galaxies. This will happen both for the faint galaxy survey out to $z \sim 1$, but also with the BGS at $z < 0.4$. Over a 10-year period, a typical (L^*) galaxy has at least a 1% probability of having a detectable SN Ia. This means that the BGS will contain of order 10^5 supernova host galaxies, and the LRG sample of more massive galaxies could produce a comparable number at higher redshift. While photometric redshifts are planned for the large LSST and DES supernova samples, spectroscopic redshifts allow more precision, particularly at

low redshift where the uncertainty in the redshift and resulting luminosity distance overwhelm the intrinsic precision of the standard candle. Samples of many tens of thousands of hosts can only be achieved with multi-object wide-field surveys. We note that with DESI there is no need to wait to select the host galaxies after the explosion: at $z < 0.2$, the BGS will include more than half of all SN Ia host galaxies in the survey footprint. Having a pre-existing redshift will also enable better allocation of follow-up resources for rare transients from surveys such as LSST.

2.7.3 Synergies of DESI with *Euclid/WFIRST*

Euclid is a medium class European Space Agency survey mission designed to measure Dark Energy [104]. Recently, NASA has become a partner, enabling a group of 40 US astronomers to join the international consortium. *Euclid* will perform a $15,000 \deg^2$ survey jointly undertaking visible imaging to measure weak lensing and simultaneous near- infrared observations split into sequential imaging (for photometric redshift measurement) and slitless spectroscopy. Two Deep Fields about 2 magnitudes deeper than the wide survey and covering around $20 \deg^2$ each will be also observed, primarily for calibrations of the wide survey data but also extending the scientific scope of the mission to faint high redshift galaxies, quasars and AGNs. The spectroscopic survey is focused on Hα emitting galaxies and is most powerful at high redshifts $1 < z < 2$.

The timeline for DESI is prior to *Euclid* (which is scheduled to launch in December 2020 for 6 scheduled years of data collection), but even in the era of *Euclid*, at redshifts $z < 1$ the combination of LRGs and ELGs that DESI will observe will remain the world-leading data set for spectroscopically confirmed galaxies with good redshift measurements. At $z > 2$ the DESI measurements from Ly-α will also remain unique. Euclid may surpass DESI in the redshift range $1 < z < 2$ provided the slitless spectroscopy is as effective as hoped. DESI could help *Euclid* clustering measurements by providing important information on the potential confusion of the *Euclid* slitless spectroscopy in this redshift range. The combination of Euclid space-based weak lensing with the large spectroscopic samples from DESI will be a strong opportunity for galaxy-galaxy weak lensing, similar to what was discussed in the DES/LSST context in the previous subsection. DESI's contribution of $z < 1$ lenses is particularly important in this regard.

WFIRST-AFTA is an envisaged NASA mission using a 2.4 m diameter primary mirror satellite being designed to perform a $2000 \deg^2$ near-infrared survey, including a slitless spectroscopic component [105]. The current narrow/deep *WFIRST-AFTA* concept is highly complementary to the wide/shallow *Euclid* strategy, and will provide deeper, denser galaxy samples. However, the smaller area covered compared to either *Euclid* or DESI means that the direct expansion rate and growth rate measurements would be weaker.

Comparisons of the precision of the BAO measurement projected for DESI, *Euclid*, and *WFIRST* are shown in Figure 2.9.

DESI will be highly complementary to the weak lensing surveys to be performed for *Euclid* and *WFIRST-AFTA*, providing spectroscopic galaxy samples at the same redshifts as the matter that is causing the lensing, thus enabling many innovative analyses from these combined datasets. DESI will help in the calibration of photometric redshifts - which are essential for these lensing experiments - and aid in investigating systematic issues such as intrinsic alignments. Likewise, *Euclid* and *WFIRST-AFTA* will greatly enhance the legacy value of DESI, providing high resolution optical and NIR imaging of all DESI targets, greatly improving the prospects for non-dark energy science, e.g., the morphology–density relationship at $z > 1$.

3   Target Selection

The DESI survey will measure with high precision the baryon acoustic feature imprinted on the large-scale structure of the Universe, as well as the distortions of galaxy clustering due to redshift-space effects. To achieve these goals, the survey will make spectroscopic observations of four distinct classes of extragalactic sources – the bright galaxy sample (BGS), luminous red galaxies (LRGs), star-forming emission line galaxies (ELGs), and quasi-stellar objects (QSOs). Each of these categories requires a different set of selection techniques to acquire sufficiently large samples of spectroscopic targets from photometric data. To ensure high efficiency and spectroscopic completeness, we select objects with spectral features expected to produce a reliable redshift determination or a Ly-α forest measurement within the DESI wavelength range.

The characteristics of our baseline samples for each of these target classes are summarized in Table 3.1. This Table specifies the primary redshift range, the photometric bands for targeting, the projected areal density (in terms of number of targets, number of fibers allocated across all pointings accounting for multiple exposures, and the number of useful redshifts resulting per square degree), as well as the total number of objects in the desired class for which redshifts are expected to be obtained for each of these samples. This table may be compared to Table 1 in the Science Requirements Document (SRD). The SRD considers both a threshold survey of 9,000 deg^2 and a baseline survey of 14,000 deg^2. Throughout this chapter, we consider only the latter scenario; simulations for reduced focal planes indicate that we would achieve essentially the same sample surface densities as for the baseline scenario, so that sample sizes would simply scale with survey area. In the following sections, we will describe the basis of these numbers in more detail.

Summary of Target Samples

The lowest-redshift sample of DESI targets will be the Bright Galaxy Sample (BGS). These galaxies will be observed during the time when the moon is significantly above the horizon, and the sky is too bright to allow efficient observation of fainter targets. Approximately the 10 million brightest galaxies within the DESI footprint will be observed over the course of the survey, sampling the redshift range $0.05 < z < 0.4$ at high density. This sample alone will be ten times larger than the SDSS-I and SDSS-II "main sample" of 1 million bright galaxies observed from 1999-2008.

Above redshift $z = 0.4$, DESI will observe luminous red galaxies (LRGs). These luminous,

Table 3.1: Summary of the properties for each DESI target class. The bands listed are for the target selection, where g, r, and z are optical photometry and $W1$ and $W2$ denote are *WISE* infrared photometry. The exposure densities are increased over the target densities due to some objects being observed on multiple passes. The number of good redshifts and baseline sample sizes (in millions) are for successful redshifts.

Galaxy type	Redshift range	Bands used	Targets per deg^2	Exposures per deg^2	Good z's per deg^2	Baseline sample
LRG	0.4–1.0	$r,z,W1$	350	580	285	4.0 M
ELG	0.6–1.6	g,r,z	2400	1870	1220	17.1 M
QSO (tracers)	< 2.1	$g,r,z,W1,W2$	170	170	120	1.7 M
QSO (Ly-α)	> 2.1	$g,r,z,W1,W2$	90	250	50	0.7 M
Total in dark time			**3010**	**2870**	**1675**	**23.6 M**
BGS	0.05–0.4	r	700	700	700	9.8 M
Total in bright time			**700**	**700**	**700**	**9.8 M**

massive galaxies have long since ceased star formation and therefore exhibit evolved, red composite spectral energy distributions (SEDs). The BOSS survey targeted these objects to $z \approx 0.6$ using SDSS gri colors and measured spectroscopic redshifts using the prominent 4000 Å break continuum feature. While DESI will aim to achieve 350 LRGs/deg^2 over 14,000 square degrees, the BOSS sample of 119 LRGs/deg^2 will contribute significantly to our science analyses over the 10,000 deg^2 footprint in which it exists; DESI may extend this low-redshift sample over a larger footprint, but this is not in the current baseline plan. DESI will target LRGs to $z \approx 1.0$, where they may be most efficiently selected using the prominent 1.6 μm (rest frame) "bump," which causes a strong correlation between optical/near-infrared (NIR) color and redshift in this regime. We will use 3.4 μm photometry from the space-based Wide-Field Infrared Survey Explorer (*WISE*) to select LRGs efficiently in the redshift range of $0.6 < z < 1.0$. DESI can exploit the 4000 Å break to obtain secure redshifts for LRGs over this full redshift range.

The majority of the spectroscopic redshift measurements for DESI will come from ELGs at redshifts $0.6 < z < 1.6$. These galaxies possess high star formation rates, and therefore exhibit strong emission lines from ionized H II regions around massive stars, as well as SEDs with a relatively blue continuum, which allows their selection from optical grz-band photometry. The prominent [O II] $\lambda\lambda 3726, 29$ doublet in ELG spectra consists of a pair of emission lines separated in rest-frame wavelength by 2.783 Å. This wavelength separation of the doublet provides a unique signature, allowing definitive line identification and secure redshift measurements. The goal of the DESI ELG target selection will be to provide a large sample of ELGs with sufficient [O II] line flux to obtain a detection and redshift measurement to $z = 1.6$.

The highest-redshift target sample will consist of QSOs. We will measure large-scale structure using QSOs as direct tracers of dark matter in the redshift range $0.9 < z < 2.1$. At higher redshifts, we will utilize the foreground neutral-hydrogen absorption systems that make up the Ly-α forest; DESI spectra cover the Ly-α transition at $\lambda = 1216$ Å for objects at $z > 2.1$. We will use optical photometry combined with *WISE* infrared photometry in the W1 and W2 bands to select our primary sample of QSOs. QSOs are ~ 2 mag brighter in the near-infrared at all redshifts compared to stars of similar optical magnitude and color, providing a powerful method for discriminating against contaminating stars. QSOs at $z > 2.1$ used for Ly-α forest measurements do not require homogeneous selection on the sky for cosmological measurements, as we do not rely on the clustering of the QSOs themselves. As a result, DESI may exploit optical variability and additional passbands where available to enhance this sample. Those $z > 2.1$ QSOs which are selected via uniform methods across the sky may also be used to enhance clustering measurements. DESI will obtain additional exposures on the confirmed $z > 2.1$ quasars to measure the Ly-α forest to the required S/N.

Summary of Required Imaging

All DESI target samples will be selected using optical grz-band photometry from ground-based telescopes and near-infrared photometry from the *WISE* satellite. The observations assumed in our baseline targeting plan are summarized in Table 3.2. This imaging plan has been developed through a detailed analysis of alternative telescope/instrument combinations. The imaging depths will be at least 24.0, 23.4, 22.5 AB (5σ for an exponential profile $r_3 = 0.45''$) in g,r,z and 20.0, 19.3 AB (5σ) in *WISE* W1,W2. All sample magnitude limits quoted in this section are total (model-like) magnitudes for the BGS and for LRGs and ELGs, or PSF magnitudes for QSOs.

The optical imaging for the DESI targets will be provided from three telescopes at two sites, Cerro Tololo and Kitt Peak. The DECam camera on the Blanco 4-m telescope will provide grz imaging over 9000 deg^2 in the DESI footprint at Dec $\leq +34$ deg. The first 6700 deg^2 of this

**Table 3.2:** Summary of telescopes being used for targeting.

Telescope	Bands	Area deg^2	Location	Status
Blanco DECam	g,r,z	9k	NGC+SGC (Dec $\leq$ +34 deg)	Begun 2014B
Bok 90Prime	g,r	5k	NGC (Dec $\geq$ +34 deg)	Begun 2015A
Mayall MOSAIC-3	z	5k	NGC (Dec $\geq$ +34 deg)	To begin 2016A
WISE-W1	3.4 μm	all sky	all-sky	Completed
WISE-W2	4.6 μm	all sky	all-sky	Completed

footprint (DECaLS) has been approved as a 64-night NOAO "Large Survey" program during the period August 2014 through July 2017 and is 40% completed. An 8-night extension of this program (DECaLS+) has been approved for the 2016A semester to obtain another 800 deg^2 in the Northern Galactic Cap. A proposal to observer the remainder of the DESI footprint in the South Galactic Sky will be submitted in future semesters. The Bok 2.3-m telescope is providing gr imaging over the 5000 deg^2 region of the North Galactic Cap (NGC) that lies at Dec $\geq$ +34 deg with the existing 90Prime camera. The 220 nights necessary for these observations are guaranteed via an MOU with the University of Arizona / Steward Observatory. Observations were taken in Spring 2015 which identified electronics problems in the camera that were corrected in September 2015. The Bok observations re-started in January 2016 and are now 15% complete. The Mayall 4-m telescope will provide z-band imaging over the same NGC footprint using the existing MOSAIC-2 camera upgraded with 4 red-sensitive CCDs. Those observations will be conducted over 220 nights in 2016 and 2017. The Mayall observations began in February 2016 and are now 15% complete. All imaging data are planned to be completed by August 2017, where the Mayall observations must be complete as that telescope will being taken off-line for DESI installation.

The *WISE* satellite is obtaining infrared imaging to sufficient depths for DESI target selection over the full sky. An initial 13-month survey is being supplemented with a 3-year extended mission known as *NEOWISE* that began 1 December 2013 and will complete in December 2016. The initial *WISE* survey and first year of *NEOWISE* data are publicly available, with the final two data releases scheduled for March 2016 and March 2017.

The DESI analyses will be performed separately in each of the three regions of the DESI footprint: the NGC at DEC > +34 deg, the NGC at DEC < +34 deg, and the South Galactic Cap (SGC). Based on SDSS-III/BOSS experience with separately-calibrated regions, we expect to analyze these separately and combine the cosmological constraints downstream. The DECam and Bok/MOSAIC coverage will have some overlap (at the DEC $\approx$ +34° strip and by targeting specific calibration fields like COSMOS, Boötes, and DEEP-2) in order to tie together calibrations and understand the subtle variations in target selection resulting from differences in filter+telescope response between the two datasets.

In the remainder of this Section, we demonstrate that our baseline optical/infrared color selections can select the targets listed in Table 3.1, and summarize the key properties of each sample. The accompanying instrument volume of the FDR details the design of the DESI instrument, which informs a spectral simulator presented in that volume. The spectral simulator aids in the design of the targeting strategy (such as magnitude limits), calculates exposure times, and estimates redshift measurement efficiencies. Given the expected target densities and exposure times, the overall survey strategy is developed in Section 4. Included in the survey strategy is an optimized method to tile the sky that maximizes the area covered and number of target redshifts obtained, while minimizing the overall time required for the survey. The outlines for a strategy for fiber allocation
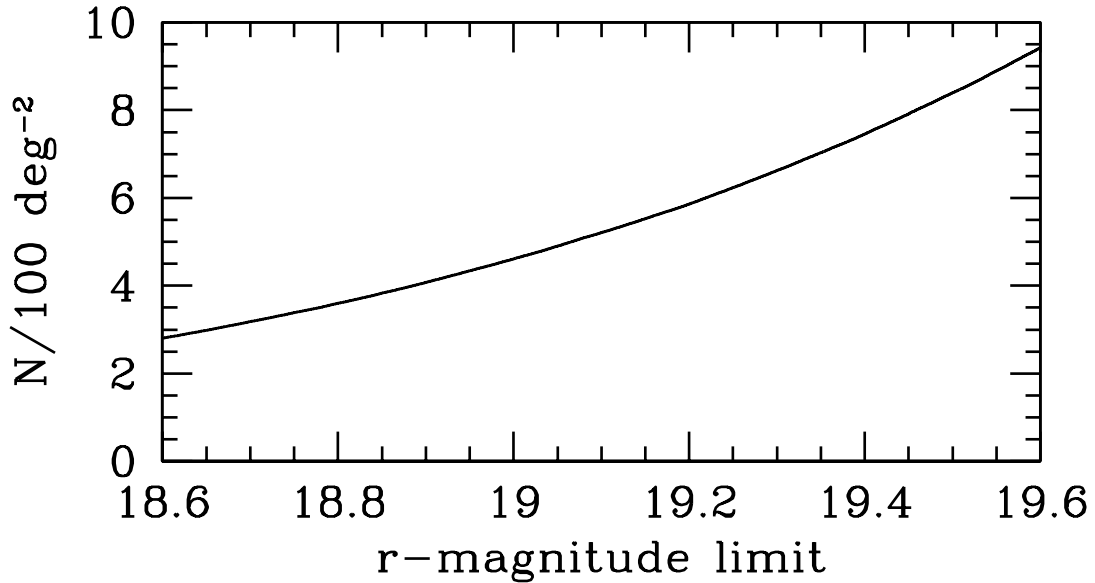
Figure 3.1: Surface density of BGS targets as a function of r-band magnitude from a numerical simulation. This mock is calibrated to match low-redshift data from SDSS.

are given in the accompanying FDR. This strategy leads to the values given in Table 3.1.

3.1 Targets: Bright Galaxy Sample

3.1.1 Overview of the Sample

The galaxy sample for the BGS will be a flux-limited, r-band selected sample of galaxies. The magnitude limit is determined by the total amount of observing bright time and the exposure times required to achieve our desired redshift efficiency. This target selection is, in essence, a deeper version of the galaxy target selection for the SDSS main galaxy sample (MGS). We explore the properties of the BGS target sample through mock catalogs created from numerical simulations. These mocks have identical properties to the MGS at low redshift, including the luminosity function, color distribution, and clustering properties. At higher redshifts, the mock BGS is calibrated using data from the much smaller areas of the GAMA ($z \sim 0.3$) and DEEP2 ($z \lesssim 1.0$) surveys.

3.1.2 Sample Properties

Surface Density

Figure 3.1 shows the surface density of targets as a function of limiting magnitude. We expect to have a density of just over 800 deg^{-2} for an r-band limit of 19.5, somewhat higher than the goal of 700 targets per deg^{-2}.

Redshift Distribution

Figure 3.2 shows the estimated redshift distribution and space density of galaxies. The upper panel shows the redshift distribution dN/dz in units of 10^3 deg^{-2} per unit redshift. The area under the curve is 800 targets/deg^{-2}. The redshift distribution peaks at $z \sim 0.2$, a factor of 2 higher than the MGS, with a tail out past $z = 0.4$. For comparison, results from GAMA at $r < 19.45$ are shown with the filled circles. The lower panel shows the space density of galaxies in units of comoving
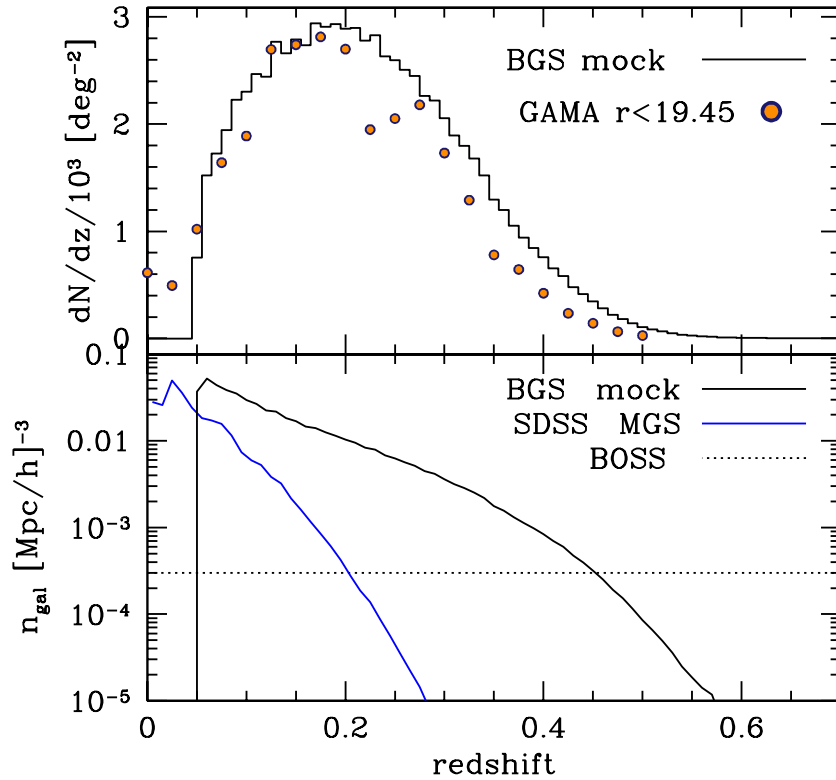
Figure 3.2: *Upper panel*: The redshift distribution of the mock BGS sample. The distribution peaks at $z = 0.18$ with a median redshift of $z = 0.204$. *Lower panel:* The space density of BGS galaxies as a function of redshift. For comparison, the space density of the MGS is shown with the blue curve, and the approximate space density of the full BOSS LRG sample (LOWZ+CMASS) is shown with the dotted line. The space density of the BGS sample is larger than the MGS+BOSS samples up to $z \sim 0.4$.

$(\mathrm{Mpc}/h)^{-3}$. For reference, the space density of the MGS is shown, as well as the density of BOSS LOWZ+CMASS objects, which is roughly constant at 3×10^{-4} $(\mathrm{Mpc}/h)^{-3}$. The BGS sample has a significantly higher density than either the MGS or BOSS out to a redshift of $z = 0.4$. At $z = 0.3$, the sampling of the density field is over an over of magnitude higher in the BGS than in the sum of all SDSS targets.

Redshift measurement method

As a simple flux-limited sample, the BGS will target both star-forming and quiescent galaxies. Redshifts will be obtained from template fits over the full DESI spectral range, with the significance of the fits dominated by the emission lines for star-forming galaxies and by the 4000Å break and Mg absorption features for quiescent galaxies. Figure 3.3 shows the redshift efficiency as a function of both exposure time and lunar phase for a test sample of galaxies. The test sample is constructed by taking random MGS galaxies and 'moving' them further away from the observer by a factor of 2 in redshift. Because the median redshift of the MGS is $z \sim 0.1$, this process creates a test sample with the same median redshift as the BGS sample. We take into account the change in the fraction of light from the galaxy that enters the fiber aperture through redshifting, the change in the angular diameter distance, the change in the point spread function from SDSS to DESI, and the different fiber diameters. `desi_quicksim` is used to create DESI spectra for each test galaxy
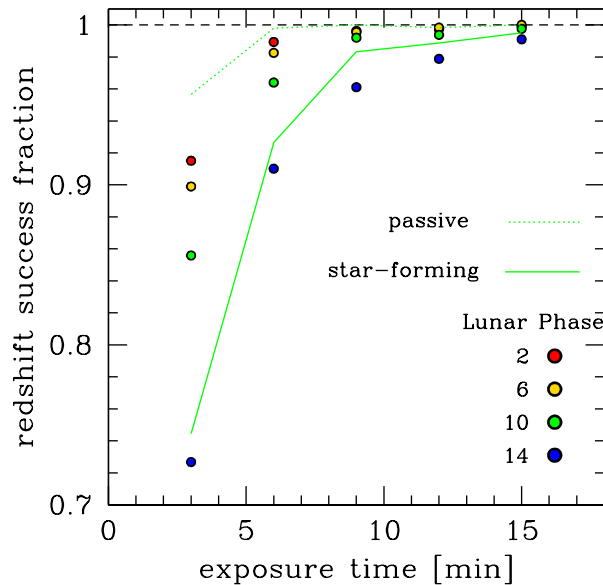
Figure 3.3: The redshift success rate for BGS-like targets. Test targets are created by 'observing' MGS galaxies at twice the true redshift of the galaxies. Test spectra are created using `desi_quicksim`, incorporating a lunar model that incorporates the phase, zenith angle of the moon, zenith of the target, and the angle between the target and the moon. Results are shown as a function of exposure time and lunar phase. The green curves show the results for a 10-day lunar phase for passive and star-forming galaxies.

at a variety of exposure times and lunar phases. Redshifts are obtained using the BOSS redshift code `zfind`, and compared to the true redshift ($2 \times z_{SDSS}$). Phase, as indicated in the key, is in units of days, with maximum illumination at 14 days and zero illumination at 0 days. Typical BGS observing conditions will be at 10 days, on average. At this phase, the overall redshift success rate is 96% at $t_{\exp} = 6$min, increasing to $\gtrsim 99\%$ at 9 min. Success fraction decreases monotonically with increasing moon illumination. An additional factor in the degree to which the moon affects observations is the angular separation between the moon and the target. All results here are for a separation of 60 degrees.

The results for star-forming and passive galaxies for 10-day phase are shown as well. Galaxies are classified as star forming or passive by their $D_n(4000)$ value, with $D_n(4000) > 1.5$ being passive. At fixed observing conditions, the redshift success rate for star-forming galaxies is lower than for the passive galaxies, indicating that the 4000Å break is more efficient as a redshift indicator given the spectral noise imparted by the observing conditions. But the redshift success rate for star-forming galaxies is still $\sim 98\%$ for 9 minute exposure times.

Large-scale-structure bias

Estimating the bias of the BGS sample is straightforward due to its completeness in magnitude. We use the abundance matching technique (e.g., [191]) to match galaxies to halos as a function of their luminosity. The bias is then estimated by integrating over the halo mass function, weighted by the number of galaxies per halo. The upper panel in Figure 3.4 shows the bias as a function of redshift obtained with this technique. At low redshift, where the magnitude-limited nature of the survey spans a wide range of absolute magnitudes, the bias is near unity. As redshift increases, the bias monotonically increases. This is for two reasons: for a flux-limited sample, the objects
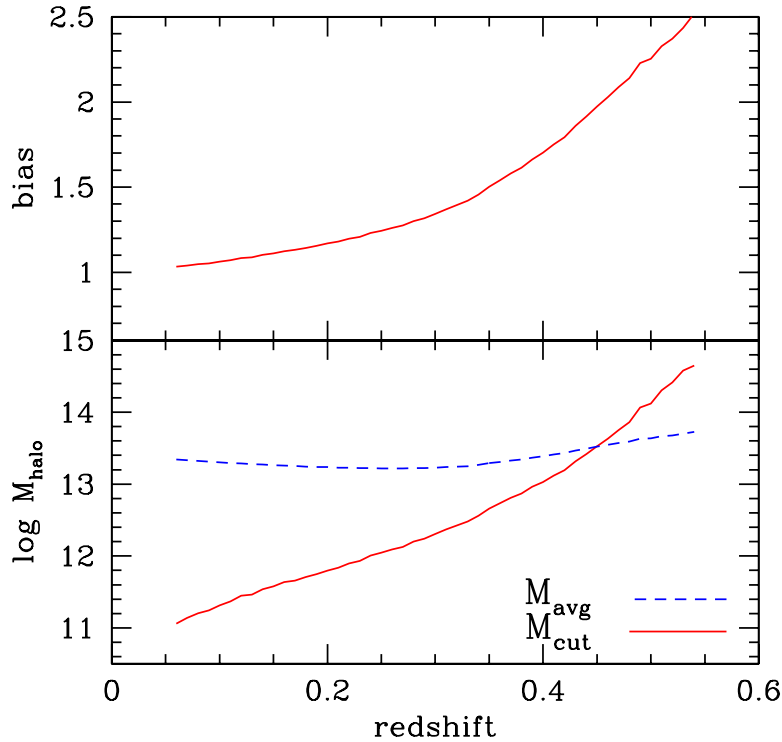
Figure 3.4: *Upper panel*: The bias of the BGS sample as a function of redshift. The bias is calculated using the abundance matching model and the space density from Figure 3.2. *Lower panel:* The halo mass scales probed in the BGS sample. M_{avg} is the mean halo mass of the sample. M_{cut} is a cutoff mass scale where halos have 50% probability of containing a galaxy in the sample. The scatter in halo mass at fixed luminosity increases with luminosity, thus increases with redshift. This causes the inversion between M_{avg} and M_{cut} when the number density drops below the BOSS value.

at higher redshift are intrinsically brighter and therefore have higher clustering amplitude, and at higher redshift the bias increases because the amplitude of dark matter clustering is decreasing.

The bottom panel shows the halo masses probed by the BGS target selection as a function of redshift. M_{cut} is a cutoff mass scale: halos of this mass have a 50% probability of having galaxies in the sample. Significantly above M_{cut}, this probability asymptotes to 100%, but the width of this transition is reflective of the scatter of halo mass at fixed luminosity. This scatter increases with luminosity, which causes the mean halo mass, M_{avg}, to vary more slowly than M_{cut}. For the brightest galaxies, this scatter is so large that M_{avg} is actually below M_{cut}.

Target selection efficiency

The dominant loss of targets is due to fiber assignment inefficiencies. Low-redshift galaxies have higher angular clustering on the sky, which can lead to more contention for fibers in high density regions. However, as described in §4.5, the BGS is being observed in 3 layers to achieve fairly high completeness.

A few percent of galaxies will be lost by deblending errors, superpositions with bright stars, and other artifacts that typically affect imaging catalogs.

Areas of risk

Given the straightforward nature of the target selection, the BGS has minimal risks. There are two possible sources of low-level risk. As shown in Figure 3.3, the redshift efficiency for star-forming objects lags behind that of passive galaxies at fixed observing conditions. The majority of these redshift failures lie in the green valley, in between the main star-forming sequence and the red sequence. These objects have low star formation rates and thus weak emission lines, but do not have stellar populations evolved enough to have strong $D_n(4000)$ values. Dependent on the integration time and observing conditions, the BGS may be incomplete for green-valley objects.

Another possible source of incompleteness is low surface brightness objects, which become more difficult to observe under bright time conditions.

3.2 Targets: Luminous Red Galaxies

3.2.1 Overview of the Sample

The lowest-redshift dark-time sample for DESI will come from targeting 350 candidate luminous red galaxies (LRGs) per square degree [192]. These objects are both high in luminosity and red in rest-frame optical wavelengths due to their high stellar mass and lack of ongoing star formation. They exhibit strong clustering and a relatively high large-scale-structure bias, which enhances the amplitude of their power spectrum, and hence the BAO signal ([193], [194], [195]). Because of their strong 4000 Å breaks and their well-behaved red spectral energy distributions, low-redshift LRGs at $z < 0.6$ can be selected efficiently and their redshifts estimated based on SDSS-depth photometry [196]. The BOSS survey has targeted 119 LRGs per deg^2 with $z \lesssim 0.6$ using SDSS imaging.

DESI science analyses will incorporate existing BOSS spectroscopic samples (which cover 10,000 deg^2 of the DESI footprint) where available, as well as applying BOSS-like target selection algorithms (in regions not yet covered) to target LRGs at low z. Because the BOSS target selection is well understood and documented in SDSS papers, we will not discuss it further here. Extending the LRG sample to redshifts $z > 0.6$, where the 4000 Å break passes beyond the r band and the optical colors of LRGs overlap with those of red stars, requires different selection techniques, taking advantage of available near-infrared imaging from space. The remainder of this section will focus on the strategy we will use in that domain.

### 3.2.2 Selection Technique for $z > 0.6$ LRGs

The spectral energy distributions of cool stars exhibit a local maximum around a wavelength of 1.6 μm, corresponding to a local minimum in the opacity of H$^-$ ions [197]. This feature, commonly referred to as the "1.6 μm bump", represents the global peak in the flux density (f_ν) for stellar populations older than about 500 Myr [198], such as those in LRGs. In Figure 3.5 we plot an example LRG template spectrum from [199], illustrating both the strength of this peak and the depth of the 4000 Å break. The lowest-wavelength channel in *WISE*, the W1 band centered at 3.4 μm, is nearly optimal for selecting luminous red galaxies; it overlaps the bump at redshift near $z = 1$, so that higher-redshift LRGs will be bright in *WISE* photometry but comparatively faint in the optical. As may be seen in Figure 3.6, a simple cut in r - $W1$ color can therefore select LRGs effectively, while adding in information on $r - z$ color can help in rejecting non-LRGs. *WISE* data are particularly well suited for this application, as the survey depth was designed specifically for detection of L_* red-sequence galaxies to $z = 1$; LRGs are generally significantly brighter than this limit. In addition, we currently apply an $i_{SDSS} > 19.9$ cut to emulate rejection of previous BOSS-like targets.
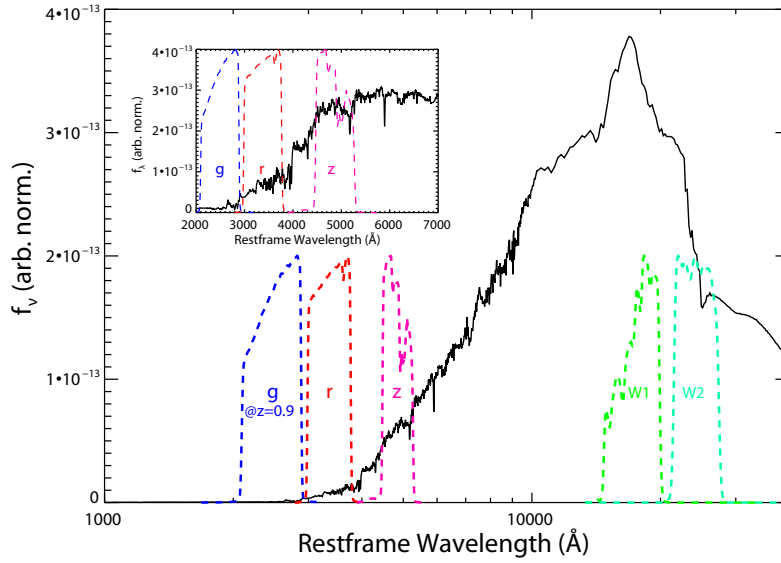
Figure 3.5: A template spectrum based upon observations of the nearby elliptical galaxy NGC 4552, drawn from the work of [199]. The spectrum f_ν is plotted as a function of rest-frame wavelength; we overplot the total (telescope + instrument + detector) response curves for DECam grz and *WISE* $W1$ and $W2$ imaging at the appropriate rest frame wavelengths for an LRG at $z = 0.9$. The 1.6 micron bump, the key spectral feature that enables our LRG selection method, corresponds to the peak in this spectrum. In the inset, we plot flux f_λ over a limited wavelength range in order to illustrate clearly the 4000 Å break and the abundance of spectral absorption features in this vicinity, which will be exploited by DESI to measure redshifts for LRGs.
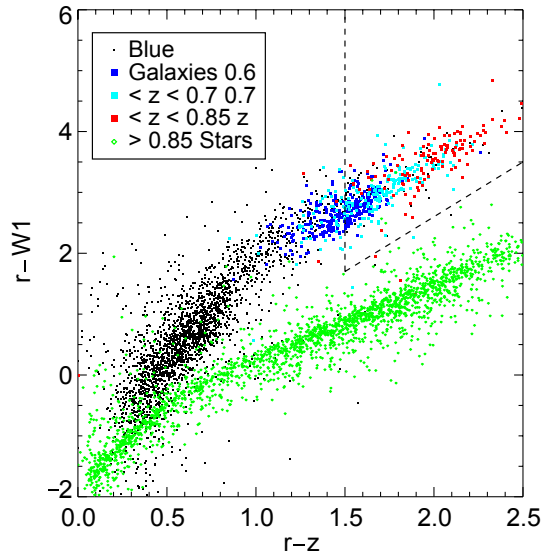
Figure 3.6: An optical/near-infrared color-color diagram for galaxies observed by both DECam and WISE in the COSMOS field, where highly accurate 30-band photometric redshifts are available and used to label points the points shown. In this and subsequent figures, r indicates DECam r-band AB magnitude, z indicates DECam z_{AB}, and W1 indicates *WISE* 3.4 μm AB magnitude. Galaxies with LRG-like spectral energy distributions also having $z > 0.6$ are indicated by points color-coded according to their redshift, whereas small black points indicate blue galaxies at all redshifts. The dashed lines indicate the borders of our LRG selection box; our baseline sample assumes that objects above and to the right of these lines that also have magnitude $z_{AB} < 20.46$ will be targeted by DESI as high-redshift LRGs.
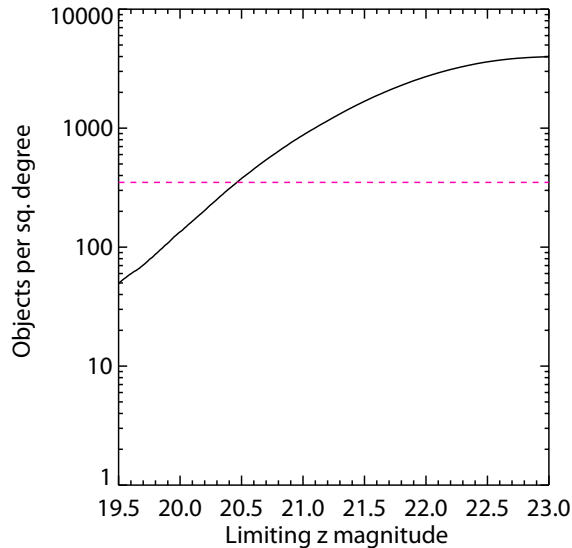
Figure 3.7: Surface densities of targeted candidate $z > 0.6$ LRGs as a function of limiting z-band magnitude. We plot here the surface density of objects that lie within the target selection box shown in Figure 3.6 as a function of their z_{AB} magnitude, as determined from DECam data in the 35 square degree DECaLS Early Data Release region. We also indicate our goal density of 350 targets per square degree via the magenta dashed line. Our baseline LRG sample size is attained at a depth of $z_{AB} < 20.46$. At this limit, an average of roughly two spectroscopic measurements per LRG will be required to attain secure redshifts for $> 98\%$ of targets.

We have tested selection techniques using optical grz catalogs derived from CFHT Legacy Survey [200], SDSS Stripe 82 data, or DECam grz imaging; NIR imaging from *WISE*; and redshifts and rest-frame colors derived from DEEP2 spectra [201] or accurate 30-band COSMOS photometric [202] redshifts. A BOSS ancillary program has obtained roughly $10,000$ redshifts of magnitude $z_{SDSS} < 20$ LRG candidates selected using SDSS and *WISE* photometry with somewhat broader color cuts than DESI will likely use, which provide additional tests of our basic techniques.

3.2.3   Sample Properties

The baseline LRG selection cuts for DESI are shown by the solid lines in Figure 3.6. This selection, applied to a sample with a total DECam z-band magnitude limit of $z_{AB} = 20.46$, relies on optical photometry in the r and z bands and infrared photometry in the *WISE* W1 band. DESI target LRGs will often not be detected in the anticipated g band imaging, but are well above the depth limits in the r, z, and $W1$ bands, having $r < 23$ and $W1 < 19.5$.

This selection is already sufficient to meet all DESI design requirements, though we anticipate further improvements in the future. The major properties of this sample are:

Surface Density

Figure 3.7 shows the effect of changing the limiting magnitude on the surface density of selected targets using the color cuts shown in Figure 3.6. Based upon tests with DECam grz data in the Early Data Release field, we find that the baseline sample density of 350 LRG targets/deg^2 is achieved when selecting objects down to a magnitude limit $z_{AB} = 20.46$.

Based on the results of the BOSS ancillary *WISE* LRG program, we can expect high ($> 98\%$)

redshift completeness for $z_{AB} < 20$ LRGs with one DESI visit, for $z_{SDSS} < 20.38$ with two visits, or for $z_{SDSS} < 20.57$ with three visits. For our baseline sample, a mean of two visits per object will thus be required (given the fractions of the sample with $z_{SDSS} < 20$ or $z_{SDSS} > 20.38$). We note, however, that redshift completeness has been somewhat lower than this for the eBOSS LRG sample, due to a combination of a bright i magnitude limit applied to exclude CMASS galaxies, instrumental issues, and limitations of the BOSS data pipelines when handling low-S/N objects; improvements are underway to address the latter issues. A more conservative estimate of anticipated completeness based on the eBOSS experience may be 90–95%; however, adopting these lower completeness numbers would have negligible effect on cosmological constraint forecasts.

Redshift Distribution

We have estimated the redshift distributions resulting from the DESI baseline target selection (see Figure 3.8) by using both COSMOS photometric redshifts and spectroscopic redshifts from our SDSS-III/BOSS ancillary program. Specifically, for the latter we applied an SDSS-passband-optimized version of the DESI selection cuts to SDSS Stripe 82 + *WISE* photometry, and then assigned the selected galaxies the spectroscopic redshift of the nearest-color object from our BOSS ancillary program. The larger noise in the SDSS imaging over the ancillary program's footprint causes the redshift assignment to be contaminated by lower-redshift objects, while the high-redshift tail is suppressed by the lack of redshifts at $20 < z_{\mathrm{SDSS}} < 20.46$, making the resulting redshift distribution somewhat more weighted toward low redshift than DESI's should be. In contrast, in the COSMOS field we can use DECam imaging for selection and photo-z's are available to much fainter than $z = 20.46$, but due to the small area of the field sample/cosmic variance yields strong fluctuations in the redshift distribution. Even given these limitations, we find that our sample selection meets or exceeds all requirements for the DESI baseline LRG sample.

As this figure shows, we have a particularly large density of objects at $z < 0.8$ and will likely down-sample at those redshifts accordingly (e.g., by using a brighter magnitude limit for objects with blue $r - z$ colors). The apparent magnitude of LRGs is strongly correlated with their redshift, allowing us to sculpt the LRG redshift distribution efficiently.

Redshift measurement method

LRGs exhibit a prominent break in their spectral energy distribution around 4000 Å (rest-frame), associated with multiple strong absorption-line features. This feature will be covered by the DESI spectrograph at redshifts up to $z = 1.45$. Our exposure times per target are set to achieve equivalent signal-to-noise at the wavelengths of interest as our BOSS ancillary program targeting $z_{SDSS} < 20$, $z > 0.6$ LRGs attained in one hour of SDSS exposure time. We therefore expect to obtain highly-secure redshifts for a comparable fraction of targets ($> 98\%$) as in that ancillary program.

Large-scale-structure bias

In order to predict the strength of the BAO feature in galaxy clustering measurements, we must assume a value for the ratio of galaxy clustering to dark matter clustering, commonly referred to as the large-scale structure bias. On large scales this may be approximated as a function of redshift that is independent of scale, $b(z)$. We can anticipate that the bias for $z > 0.6$ luminous red galaxies should be at least as large as that of BOSS LRGs, as only the most extreme objects will be able to assemble a large amount of mass and cease star formation by this earlier epoch. We therefore assume a bias of the form $b(z) = 1.7/D(z)$, where $D(z)$ is the growth factor; this matches the value
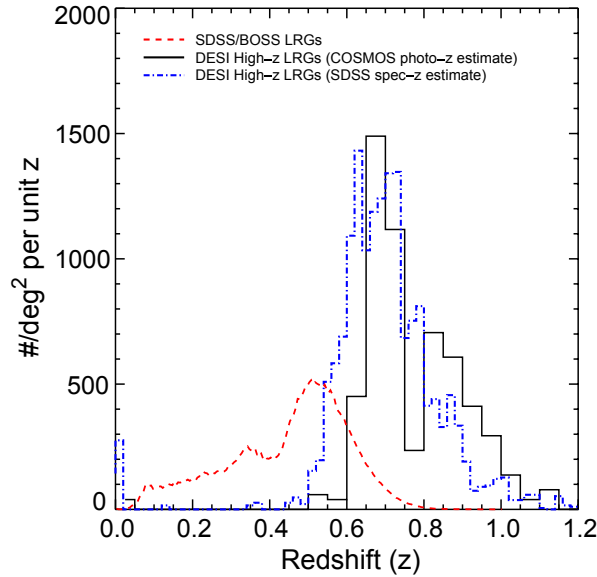
Figure 3.8: DESI LRG redshift distribution for our candidate sample from two studies: *(black)* Photometric redshift distribution for a sample selected using DECam imaging in the COSMOS field, which has full redshift coverage but suffers from high sample variance (as seen from the feature at $z \approx 0.77$). *(blue)* Spectroscopic redshift distribution for galaxies selected using SDSS Stripe 82 photometry and assigned the redshift of the object with the nearest color from a BOSS ancillary program. The latter sample has low sample variance, but the high-redshift tail is suppressed by the lack of redshifts at $20 < z_{\mathrm{SDSS}} < 20.46$. Shown in red is the redshift distribution of low-z LRGs, many of them already observed by SDSS-I/II and SDSS-III/BOSS, which will be included in the DESI analysis.

measured by SDSS-I at $z = 0.34$ [193] and by SDSS-III at $z = 0.57$ [203]. We have extrapolated this trend to $z = 1$ for the DESI LRGs.

Target selection efficiency

Targets selected as LRGs could fall short in several ways: they could fail to yield redshifts entirely; they could prove to be stars rather than galaxies; they could be outside of the desired redshift range; or they could turn out to be blue (i.e., star forming and less highly biased). Based on results from the BOSS ancillary program, we expect to obtain redshifts for $> 98\%$ of LRGs targets, as described above. Roughly 2% of the objects targeted via the baseline selection box (which could be further optimized) are stars. 98% of the galaxies selected are at $z > 0.6$, while 98% of the galaxies selected prove to have red-sequence rest frame colors. If we treat all failure modes as independent (the worst-case scenario), this yields a net target selection efficiency of 92%; i.e., more than 92% of all DESI LRG targets will be luminous red galaxies in the correct redshift range with a secure redshift measurements.

Areas of risk

There are few sources of risk in our LRG selection, the most important of which is the possibility that the COSMOS field is unrepresentative of the overall survey and instead contains (due to Poisson statistics or cosmic variance) an unusually large fraction of galaxies with red colors at $z > 0.6$. At worst, this would degrade the target selection efficiency to near 90%. The second

potential source of risk is that the redshift success rate for LRGs is not simply a function of the signal-to-noise ratio, in which case we can not map our BOSS ancillary experience to DESI. These risks will be reduced with the continuation of the spectroscopic eBOSS program.

To summarize, the luminous red galaxy selection methods used for our baseline plan will yield a high-bias sample of about 315 LRGs/deg^2 (assuming 90% efficiency net) from a sample of 350 targets/deg^2; almost all will be galaxies at $z > 0.6$. To be conservative, our projections assume that only 86% of the targeted LRGs (i.e., 300 per square degree) will in fact be $z > 0.6$ luminous red galaxies. Combined with BOSS LRGs and the Bright Galaxy Sample at lower redshift, this will allow us to measure the BAO scale from $0 < z < 1$. This sample allows direct comparisons to cosmological results provided by the ELG sample in overlapping redshift ranges, providing a key test for systematic effects.

3.3 Targets: Emission Line Galaxies

3.3.1 Overview of the sample

Emission-line galaxies (ELGs) constitute the largest sample of objects that DESI will observe. The galaxies exhibit strong nebular emission lines originating in the ionized ("H II") regions surrounding short-lived but luminous, massive stars. ELGs are typically late-type spiral and irregular galaxies, although any galaxy actively forming new stars at a sufficiently high rate will qualify as an ELG. Because of their vigorous ongoing star formation, the integrated rest-frame colors of ELGs are dominated by massive stars, and hence will typically be bluer than galaxies with evolved stellar populations such as LRGs. The optical colors of ELGs at a given redshift will also span a larger range than LRGs due to the greater diversity of their star formation histories and dust properties.

DESI leverages the fact that the cosmic star formation rate was roughly an order of magnitude higher at $z \sim 1$ than today, which causes galaxies with strong line-emission to be very common at that epoch [204, 205, 206]. Figure 3.9 shows an example rest-frame spectrum of an ELG, which is characterized by a blue stellar continuum dominated by massive stars, a Balmer break at ~ 3700 Å (whose strength depends on the age of the stellar population), and numerous nebular emission lines, the most prominent of which are Hα $\lambda 6563$, Hβ $\lambda 4861$, the higher-order Balmer lines, and the forbidden [O III] $\lambda\lambda 4959, 5007$ and [O II] $\lambda\lambda 3726, 3729$ nebular emission-line doublets. The inset provides a zoomed-in view of the [O II] doublet (assuming an intrinsic line-width of 70 km s^{-1}), which the DESI instrument is designed to resolve over the full redshift range, $0.6 < z < 1.6$. By resolving the [O II] doublet, DESI will avoid the ambiguity of lower-resolution spectroscopic observations, which cannot differentiate between this doublet and other single emission lines [207].

### 3.3.2 Selection Technique for $z > 0.6$ ELGs

The DESI/ELG targeting strategy builds upon the success of the DEEP2 galaxy redshift survey, which used cuts in optical color-color space to effectively isolate the population of $z \gtrsim 0.7$ galaxies for follow-up high-resolution spectroscopy using the Keck/DEIMOS spectrograph [209, 201]. More recently, several SDSS-III/BOSS and SDSS-IV/eBOSS ancillary programs have confirmed that optical color-selection techniques can be used to optimally select bright ELGs at $0.6 < z < 1.7$ [210, 211, 212].
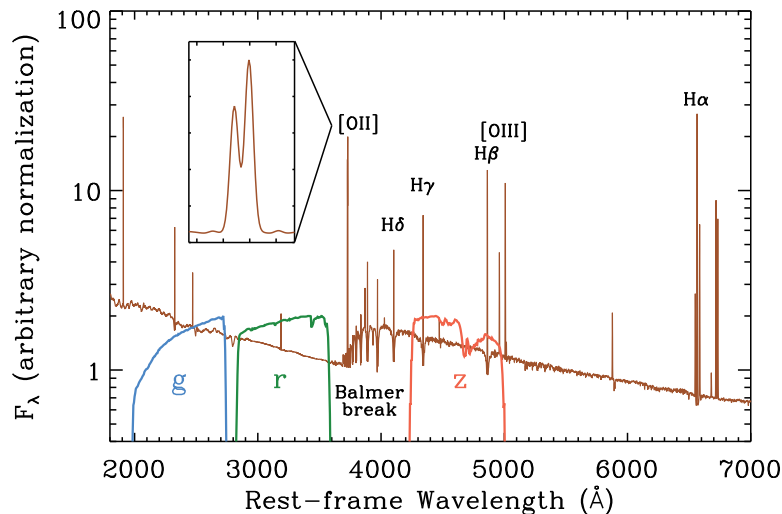
Figure 3.9: Example rest-frame spectrum of an ELG showing the blue stellar continuum, the prominent Balmer break, and the numerous strong nebular emission lines. The inset shows a zoomed-in view of the [O II] doublet, which DESI is designed to resolve over the full redshift range of interest, $0.6 < z < 1.6$. The figure also shows the portion of the rest-frame spectrum the DECam grz optical filters would sample for such an object at redshift $z = 1$.

In Figure 3.10 we plot the $g - r$ vs $r - z$ color-color diagram for those galaxies with both highly-secure spectroscopic redshifts and well-measured [O II] emission-line strengths from the DEEP2 survey of the Extended Groth Strip (EGS) [201]. The grz photometry of these objects is drawn from CFHTLS-Deep observations of this field [208], transformed and degraded to the anticipated depth of our DECam imaging (see §3.6.1). As discussed in the next section, we expect to achieve a very high redshift success rate for ELGs with integrated [O II] emission-line strengths in excess of approximately 8×10^{-17} erg s^{-1} cm^{-2}. This integrated [O II] flux corresponds to a limiting star-formation rate of approximately 1.5, 5, and 15 $M_\odot$ yr^{-1} at $z \sim 0.6$, 1, and 1.6, respectively, which lies below the 'knee' of the star formation rate function of galaxies at these redshifts [213, 214].

Figure 3.10 shows that strong [O II]-emitting galaxies at $z > 0.6$ (blue points) are well-isolated from the population of lower-redshift galaxies (pink diamonds) and the stellar locus (grey contours). The separation between galaxies above and below $z \simeq 0.6$ occurs due to the spectrum blueward of the Balmer break ($\lambda_{\rm rest} \sim 3700$ Å; cf. Figure 3.9) shifting into the r-band filter, which rapidly reddens the $r - z$ color. Similarly, at $z \gtrsim 1.2$ the Balmer break moves into the z-band filter, causing both the $g - r$ and $r - z$ colors to be relatively blue at higher redshifts. The black polygon in Figure 3.10 delineates the target selection box to isolate the population of strong [O II]-emitting ELGs at $0.6 < z < 1.6$. By targeting galaxies in this box to a depth of $r_{AB} = 23.4$, we strike a balance between maximizing the number of $z \sim 1$ ELGs with significant [O II] flux while simultaneously minimizing contamination from stars and lower-redshift galaxies. ELGs galaxies with the very bluest colors are not included in the selection box, as their "flat" spectra exhibit similar colors at all redshifts and are therefore difficult to select in our redshift range.
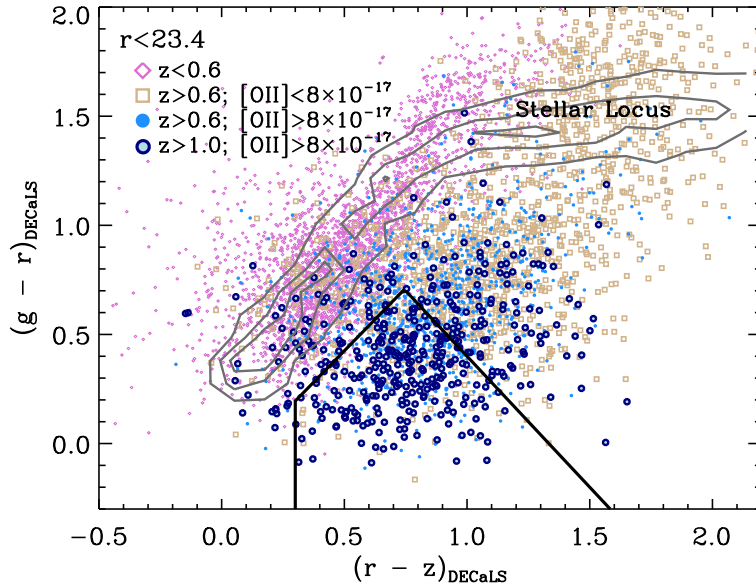
Figure 3.10: Optical $g - r$ vs. $r - z$ color-color diagram based on spectroscopy from the DEEP2 Galaxy Redshift Survey, illustrating our preliminary selection for ELGs at $z > 0.6$ with significant [O II] emission-line flux. Although the galaxy photometry is based on deep CFHTLS imaging [208], the colors have been transformed and degraded to the expected depth of the DECaLS imaging. This plot shows that strong [O II]-emitting galaxies at $z > 0.6$ (blue points) are in general well-separated from both the population of lower-redshift galaxies (pink diamonds) and from the locus of stars in this color space (grey contours). The selection box (thick black polygon) selects those galaxies with strong [O II]-emission while minimizing contamination from stars and lower-redshift interlopers.

3.3.3   Sample Properties

The baseline ELG selection criteria for DESI are based on our analysis of the DEEP2/EGS survey data, which targeted galaxies more than half a magnitude fainter and with considerably higher spectroscopic signal-to-noise ratio than DESI. Because of this greater depth, we anticipate that any galaxies with sufficiently strong [O II] flux to yield a redshift with DESI also yielded a successful redshift measurement in DEEP2. We have also cross-verified our selection criteria and redshift distributions for ELGs using data from the 1.3 deg^2 COSMOS field [215] and from the 0.6 deg^2 VVDS-Deep field [216]; both of these samples give consistent results, within the expected variation due to both sample variance and systematic differences between the samples. Our selection, when applied to imaging with magnitude limits of $g_{AB} = 24$, $r_{AB} = 23.4$ and $z_{AB} = 22.5$ (i.e., the anticipated depth of DECam Legacy imaging), is sufficient to meet all DESI science requirements (although we do anticipate to refine the sample selection even further). The major properties of this sample are as follows.

Surface Density

In Figure 3.11 we show the surface density of candidate ELGs in our grz selection box (see Figure 3.10) as a function of the r-band magnitude limit. At a depth of $r_{AB} \approx 23.4$, we achieve our goal of 2400 targets per square degree. As we discuss below, we conservatively estimate that at least 65% of these will be bona fide ELGs in the redshift range $0.6 < z < 1.6$ with a strong enough [O II] emission-line doublet (in tandem with other nebular emission
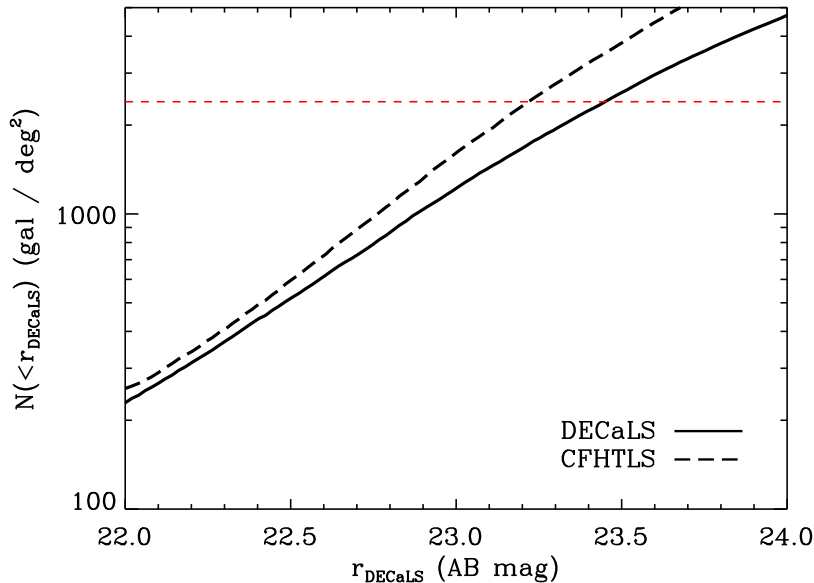
Figure 3.11: Surface density of ELGs as a function of limiting r-band magnitude. The solid black line shows the surface density of objects which lie within the target selection box shown in Figure 3.10 as a function of r_{AB} magnitude based on a 35 deg^2 region of DECaLS observed to the final survey depth. For comparison, the dashed line is the set of objects selected from CFHTLS-Deep photometry [200] which has been transformed and degraded to the anticipated depth of DECaLS. The horizontal dashed red line shows our goal density of 2400 targets deg^{-2}, which is achieved at a depth of $r_{AB} \lesssim 23.4$. We note that the differences in the two curves is most likely due to the scatter in the transformations between the CFHTLS and DECaLS photometric systems.

lines available at $z \lesssim 1$) to yield a secure redshift. Out of this sample, at most 270,000 ELGs over 500-1,500 deg^2 may be targeted by SDSS-IV/eBOSS, representing a sample that could be used for further validation of DESI targets.

Redshift Distribution

Figure 3.12 shows the anticipated redshift distribution of our candidate grz-selected sample of ELGs, determined based on those DEEP2/EGS objects which are both selected by our candidate cuts (after transforming to the DECaLS photometric system and degrading to the expected depth of the survey) and exhibit sufficient [O II] flux for DESI redshift measurements to succeed, reweighted to account for DEEP2 target selection rates.[4]

The ELG sample is designed to have a product of the number density and the power spectrum, $\bar{n}P$, that exceeds 1 over some scales. This is shown as the dashed blue line in Figure 3.12, which is the surface density for which $\bar{n}P = 1$ when evaluated at wave number $k = 0.14 \ h \, \mathrm{Mpc}^{-1}$ and orientation relative to the line-of-sight $\mu = 0.6$). Below this limit, shot noise will dominate errors in measuring the BAO signal (cf. §2.4.2). Our candidate ELG selection exceeds the $\bar{n}P = 1$ curve to redshift $z \sim 1.3$.

---

[4]DEEP2 does not cover [O II] at $z <\sim 0.8$ or $z \gtrsim 1.4$. We handle this at low redshift by assigning [O II] fluxes to galaxies at slightly higher redshift which have comparable (rest-frame) color and luminosity. For $z > 1.4$, we plot a power-law extrapolation of the redshift distribution measured at lower redshift, as DEEP2 would in general not obtain a redshift at all for objects where [O II] is past the red end of the spectrum. An analysis of COSMOS photometric redshifts for objects meeting our selection cuts suggests that this extrapolation if anything underestimates the number of objects at $1.4 < z < 1.6$.
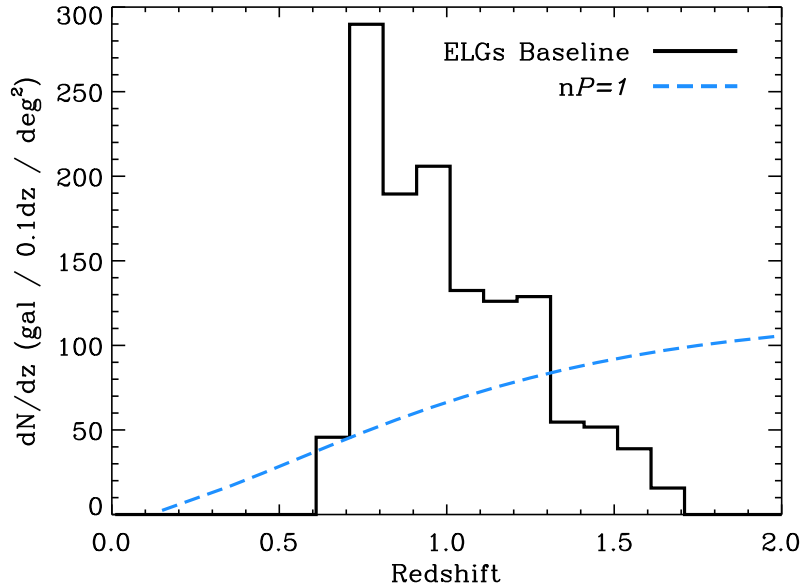
Figure 3.12: Expected redshift distribution of ELG targets based on our analysis of the DEEP2/EGS survey data (see Figure 3.10). The overall normalization of the distribution has been fixed to 1280 ELGs deg^{-2} (from a targeted sample of 2400 targets deg^{-2}) to reflect conservative estimates of the overall efficiencies of fiber assignment, target selection, and redshift measurement. The ELG redshift distribution drops to a level where shot noise dominates errors in BAO measurements (i.e., $\bar{n}P < 1$) only at $z \gtrsim 1.3$ (dashed blue line).

Redshift measurement method

The adopted grz color-cuts are designed to maximize the selection of galaxies at $z \approx 1$ with significant [O II] emission-line flux. In Figure 3.13 we plot [O II] flux as a function of redshift using the DEEP2/EGS sample. The red curve shows the limiting [O II] flux above which DESI simulations predict we will detect emission lines at $> 7\sigma$, resulting in secure redshifts. Galaxies at redshift $z > 1.0$ will have the [O II] doublet as the only strong spectroscopic feature, while those at lower redshifts will show Hβ (at $z < 0.5$) and [O III] (at $z < 1.0$).

Large-Scale Structure Bias

We estimate the linear clustering bias of our sample of ELGs relative to their dark matter halos using the DEEP2 data. Employing methods similar to those of [217] and [218], we have measured the clustering of ELGs at quasilinear scales of $1-10\ h^{-1}$ Mpc in three overlapping redshift bins centered at $z = 0.87$, 1.0 and 1.2. The observed galaxy clustering is constant within errors at all redshifts, even as the amplitude of matter clustering increases at lower redshift [219]. The observations can thus be described by a galaxy bias which is inversely proportional to the growth factor of dark matter fluctuations. Based on our measurements we adopt $b(z) = 0.84/D(z)$, where $D(z)$ is the growth factor at redshift z ($D(z) = 1$ today). This increase in the bias with redshift for star-forming galaxies is consistent with other studies of similar objects at z=0.5–2.2 [220, 221, 222].
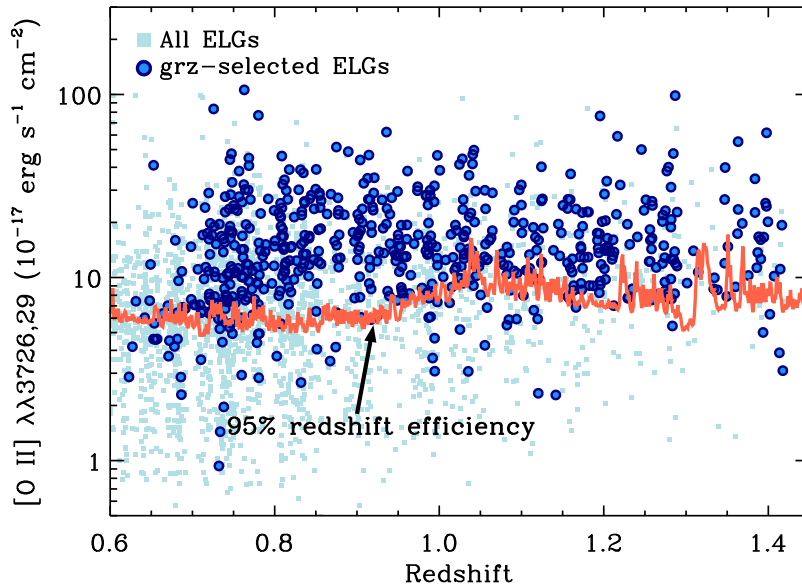
Figure 3.13: [O II] flux as a function of redshift for DEEP2/EGS galaxies. The light blue squares represent all galaxies in the sample, while the dark blue points are those objects targeted as DESI ELGs (see Figure 3.10). DESI will detect emission lines at 7σ for the bulk of the targeted sample, corresponding to those objects above the 95% efficiency line in red.

Target selection efficiency

Targets selected as ELGs could fall short in several ways: they could entirely fail to yield a redshift (e.g., if the galaxy is at $z \gtrsim 1.63$ then no strong emission lines will be detected by DESI); they could prove to be low-redshift galaxies, $z < 0.6$; they could be QSOs instead of galaxies (and hence useful for higher-redshift clustering analyses but likely outside the redshift range of the ELGs); or they could be stars. Based on the DEEP2/EGS sample, we estimate that $\sim 10\%$ of the objects targeted via the baseline selection criteria are expected to be stars, $\sim 5\%$ will be lower-redshift interlopers, and $\sim 5\%$ will be at $z \gtrsim 1.6$, while contamination from QSOs is expected to be negligible. Combining all these factors, the fraction of ELG targets which are in fact galaxies in the correct redshift range is approximately 80%. Among these objects, about 85% will have a high enough [O II] flux to securely measure a redshift more than 95% of the time (see Figure 3.13). Combining all these factors with the 78% fiber assignment rate expected for an input target density of 2400 targets deg^{-2}, we obtain an a final density of 1220 ELGs deg^{-2}.

Areas of risk

The primary source of risk in our ELG selection is the limitations of the datasets available for developing and assessing selection algorithms. DEEP2 is the only large current survey which resolves the [O II] doublet critical for obtaining secure redshifts at $z > 1$; however, due to the $z > 0.75$ color cut applied by DEEP2 in three of four survey fields, it can be used to assess the low-redshift tail of the ELG selection in only a limited area, the Extended Groth Strip used for all analyses here. Because of the limited area, the number of DEEP2 ELGs within our color box is relatively small, so both Poisson noise and sample/cosmic variance have a significant effect on our predicted redshift distributions. Furthermore, the

lack of DEEP2 coverage of [O II] at $z > \sim 1.4$ means that our assessments of performance in that regime are subject to some amount of uncertainty. Despite these shortcomings, even more assumptions and extrapolations would be necessary with any other existing dataset. The consistency of VVDS and COSMOS results—together with the initial SDSS-IV/eBOSS observations—with the DEEP2-based predictions builds confidence that these uncertainties are not substantial.

The second potential source of risk which would cause performance to fall short of our projections is that the redshift success rate for DESI ELGs could not simply be a function of signal-to-noise ratio, but may also depend in more subtle ways upon the instrumental resolution and the intrinsic galaxy velocity dispersions. For example, it would be difficult to directly discriminate between [O II] or another single-line feature at lower redshift for a population of ELGs with unusually large velocity dispersions $\sigma_v > 150$ km s^{-1} (though the rarity of low-luminosity objects with extremely high velocity dispersions, as would be implied by a false identification, may allow such cases to be resolved).

To conclude, the ELG selection methods used for our baseline plan will yield 2400 targets deg^{-2}. From these targets, DESI should securely measure redshifts for approximately 1220 ELGs deg^{-2} in the redshift range $0.6 < z < 1.6$ (see Table 3.1). This sample will enable constraints on cosmological parameters over a broad redshift range centered on $z \approx 1$, which can be directly compared to results from the independently observed samples of LRGs at $z < 1$ and quasars at $z > 1$.

3.4 Targets: QSOs

3.4.1 Overview of the sample

The highest-redshift coverage of DESI will come from quasars (a.k.a. quasi-stellar objects, or QSOs), extremely luminous extragalactic sources associated with active galactic nuclei. QSOs are fueled by gravitational accretion onto supermassive black holes at the centers of these galaxies. The QSO emission can outshine that of the host galaxy by a large factor. Even in the nearest QSOs, the emitting regions are too small to be resolved, so QSOs will generally appear as point sources in images. These are the brightest population of astrophysical targets with a useful target density at redshifts $z > 1$ where the population peaks [223, 224].

DESI will use QSOs as point tracers of the matter clustering mostly at redshifts lower than 2.1, in addition to using QSOs at higher redshift as backlights for clustering in the Ly-α forest. This enlarges the role of QSOs relative to the BOSS project, which only selected QSOs at $z > 2.15$ for use in the Ly-α forest, and enhances their role relative to eBOSS where QSOs are used in a similar fashion as in DESI although with lower densities. DESI will select 170 QSOs per deg^2 over its footprint, of which 50 per deg^2 will be at $z > 2.1$ and suitable for the Ly-α forest.

DESI pilot programs, [224] updated in [225], have answered the long-standing uncertainties in the faint end of the QSO luminosity function. The surface density for $z > 0.9$ QSOs derived from these studies is shown in Figure 3.14, along with previous estimates from [226] (25% lower) or from the LSST science book [227, 228] (40% higher). Brighter than magnitude $g = 23.0$ ($r = 23.0$ respectively), we infer that a *complete* QSO sample would contain about 185 (200, resp.) QSOs per deg^2 at $z < 2.1$ and about 75 (90, resp.) at $z > 2.1$. DESI will target and obtain redshifts for 120 and 50 QSOs per deg^2 in the redshift ranges $z < 2.1$
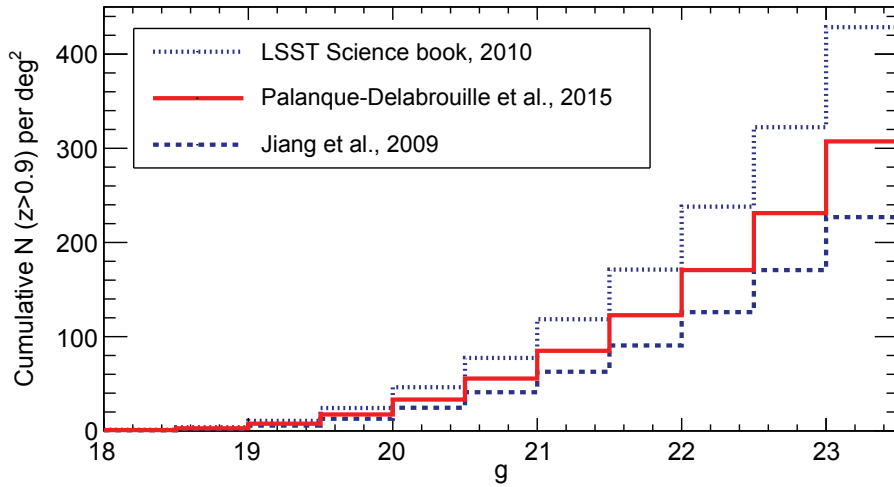
Figure 3.14: Cumulative surface density of quasars (objects per deg^2) as a function of g magnitude for $z > 0.9$, derived from different estimates of the QSO luminosity function.

and $z > 2.1$, respectively.

Because of their point-like morphologies and with *photometric* characteristics that mimic faint blue stars in optical wavelengths (Figure 3.16, middle plot), QSO selection is challenging. The photometric selection used by BOSS to target Ly-α QSOs at $z > 2.15$ has attained a 42% targeting efficiency (i.e., fraction of targets that prove to have the desired class and be in the desired redshift range), yielding 17 $z > 2.15$ QSOs per deg^2 down to the SDSS photometric limit of $g < 22.1$ [12]. The selection technique for DESI needs to achieve a minimum efficiency of about 65%; unlike for BOSS, however, QSOs at $z < 2.15$ are considered successes. A baseline scheme for QSO selection that achieves our goals for DESI is presented below.

3.4.2   Selection Technique

QSOs commonly exhibit hard spectra in the X-ray wavelength regime, bright Ly-α emission in the rest-frame UV, and a power-law spectrum behaving as $F_\nu \propto \nu^\alpha$ with $\alpha < 0$ in the mid-infrared bands [229] (c.f. Figure 3.15). In the mid-optical colors, QSOs at most redshifts are not easily distinguished from the much more numerous stars. Successful selection of a highly-complete and pure QSO sample must make use of either UV or infrared photometry; DESI relies upon optical and infrared photometry for its baseline selection.

The QSO target selection is a combination of optical-only and optical+IR selections. The greatest separation from the stellar locus in the optical comes from ugr colors where the "UV excess" in $u - g$ produces bluer colors than those of most stars (Figure 3.16 left). In the absence of u band in the baseline imaging plan, the bulk of the QSO targets are identified in an optical+IR selection (Figure 3.16 right), where the excess infrared emission from QSOs results in a clear segregation from stars with similar optical fluxes. Stellar SEDs indeed sample the rapidly declining tail of the blackbody spectrum at those wavelengths, where QSOs have a much flatter SED. We defined a color selection to depths $r = 23.0$ with cuts in $g-r$ vs. $r-z$ and in $r-W$ vs. $g-z$ shown in Figure 3.16, using DECaLS+*WISE* photometry from the DR2 data release. We restrain the selection to objects with stellar morphology, to avoid an almost 10-fold contamination by galaxies that otherwise enter our selection region.
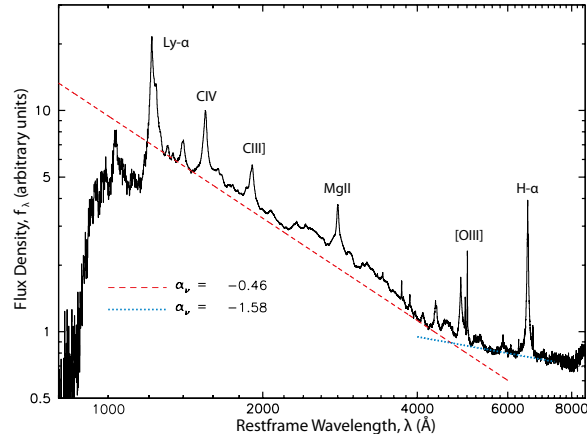
Figure 3.15: QSO spectrum exhibiting the main emission lines used in their identification.

The *WISE* data are available on the whole sky, and are photometered deeper than the public *WISE* catalogs using the Tractor-forced photometry (see section 3.8). Although *WISE* and optical data are not synchronous, the color difference between QSOs and stars is so large that QSO variability has minimal effect on the color selection. The *WISE* satellite has been reactivated, and will improve by a factor of two in signal-to-noise prior to DESI.

This baseline QSO target selection was tuned over the Stripe82 region where we led DESI pilot surveys (ancillary programs in BOSS and eBOSS, complemented by MMT observations) in order to build catalogs of spectroscopically identified QSOs at all redshift, which we use as truth tables. These pilot surveys selected highly complete samples of $g < 23$ or $r < 23$ QSOs from combined color and variability information (cf. section 3.4.5), using deep SDSS $ugriz$ and *WISE* near-infrared data sets. Our baseline selection was then tested on an independent region of Stripe82.
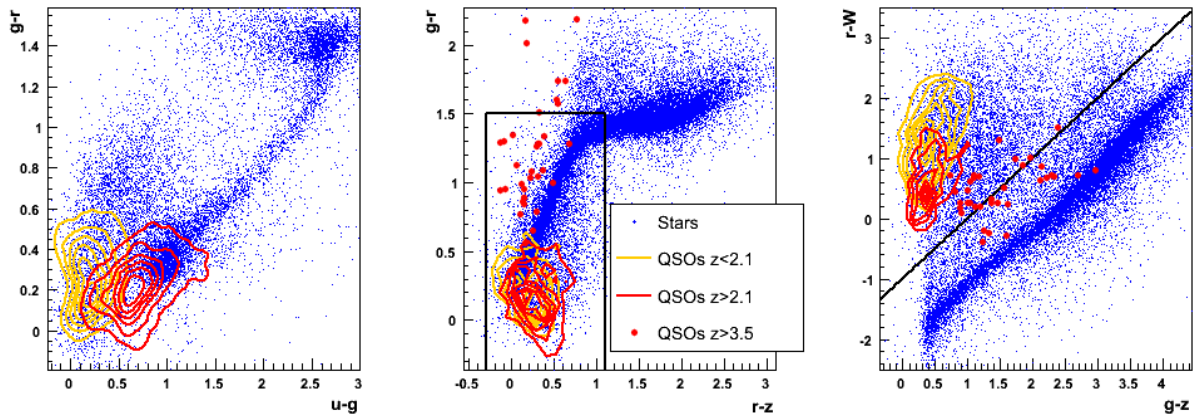
Figure 3.16: Colors in the optical ($ugrz$) or near-infrared (W is a linear combination of *WISE W1* and *W2* bands) of objects photometrically classified as stars (blue points) or spectroscopically classified as QSOs. Orange contours indicate the locus of tracer QSOs at $z < 2.1$, red contours of Ly-α QSOs at $z > 2.1$, and red dots are for $z > 3.5$ QSOs. Left panel is based on SDSS photometry, middle and right panels on DECaLS-DR2. Black lines mark the boundaries of the selection regions described in the text.

We also investigated an alternative algorithm based on a machine-learning algorithm called Random Forest. We trained it on all 47000 identified QSOs over the DECaLS-DR2 footprint, and used, for the star sample, a selection of 80000 unresolved objects in Stripe82, stripped of known QSOs and sources exhibiting QSO-like variations in their light curve. As for the previous selection, the algorithm relies solely on object colors and is restrained to unresolved sources with $r < 23$. It selects 97% of the known QSOs recovered by the more traditional color selection, but exhibits a better performance than the latter, in particular at redshifts above 2.1 or faint magnitudes.

Considering the completeness of the color cut or of the Random Forest approach as a function of redshift and magnitude, measured over truth regions, and applying it to the QSO luminosity function of [225], both selections result in over 170 QSOs per deg^2, among which over 40 per deg^2 (55 per deg^2 for the Random Forest) are at $z > 2.1$. The non-QSO targets are stellar contaminants (about 80 per deg^2 in the color-cut selection, and 60 per deg^2 in the Random Forest selection).

DESI may supplement its high-redshift QSOs with more sophisticated selection algorithms and other supplementary photometry as it becomes available. Time-domain data enable variability selection methods (as described in Section 3.4.5). UV (u-band) data improve QSO selection, and allow discrimination between low-redshift and high-redshift QSOs. Algorithmically, neural-network based algorithms [230] and an extreme deconvolution method that models the distributions of stars and quasars at the flux limit [231] have been in use by BOSS where they allowed an increase of up to 20% in selection efficiency over traditional selection algorithms [232]. They are also applied, and thus further tested, in eBOSS. A combination of these additional data and algorithms will allow DESI to target QSOs in excess to those currently planned, with a small impact on the overall fiber budget.

The main contaminants to a $grz+WISE$ QSO selection are very low-redshift star-forming galaxies with strong PAH emission, currently excluded using a star-galaxy separation based on ground-based optical imaging; a few high-redshift obscured galaxies, which are rare at bright optical magnitudes; and faint stars that artificially drift into the QSO locus because of poor optical photometry.

3.4.3 Sample Properties

Two selections using optical grz and near-infrared data achieved a performance at the level of our goals for the DESI sample. Application of additional data and more sophisticated selection algorithms may be used to boost, in particular, the high-redshift QSO densities. To be conservative, we consider below the color-cut selection as the baseline DESI QSO selection. The major properties of the baseline DESI QSO sample are :

• *Surface Density:* The current $grz+WISE$ color-box selection yields a total of 260 targets per deg^2 to a limit $r = 23$, of which about 140 per deg^2 are expected to be QSOs with $z < 2.1$ and about 40 per deg^2 are QSOs at $z > 2.1$, similar to the required densities of Table 3.1. Based on the QSO luminosity function of [225], this corresponds to about 60% of all QSOs in this magnitude range. The Random Forest selection increases this rate to 67%, with 55 $z > 2.1$ QSOs per deg^2. We anticipate that the deeper *WISE* data expected before the start of DESI will allow us to further increase the completeness and decrease the stellar contamination.

• *Redshift distribution:* The expected redshift distribution of the QSO sample is illustrated in Figure 3.17 as the thick red histogram, which is determined by assuming the QSO
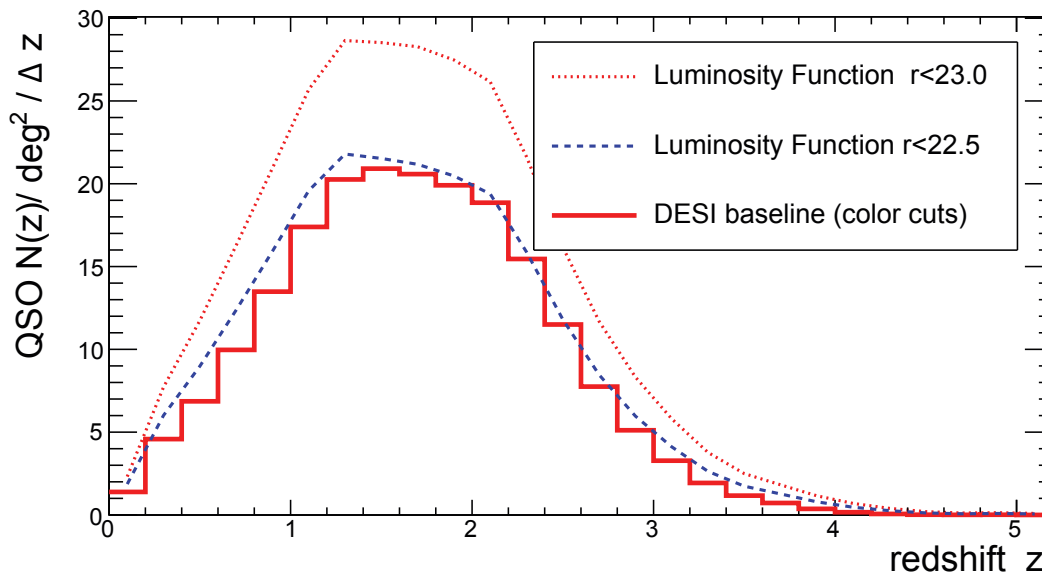
Figure 3.17: Expected distribution of QSO redshifts from DESI (thick red histogram) using the targeting efficiency measured for the baseline DECaLS-DR2 selection over truth regions. For comparison, we also show the QSO luminosity function to $r < 22.5$ (blue dashed line) and $r < 23.0$ (red dotted line).

completeness for QSOs brighter than $r < 23$ measured in the truth region for the color-cut selection. For comparison, we show on the same plot the QSO luminosity function to $r < 22.5$ (blue dashed line) and $r < 23$ (red dotted line).

• *Redshift measurement method:* The key features contributing to the classification and redshifts of QSOs are the Ly-α, CIV, CIII] and MgII emissions (c.f. Figure 3.15). From our experience with BOSS, eBOSS and MMT pilot programs, we estimate that in a single DESI visit we will fail to obtain redshifts for QSO targets about 10% of the time, mostly for objects at $g > 22.5$ [224, 225]. All QSO targets will be observed once early in the survey. Those confirmed to be QSOs at $z > 2.1$ will be re-observed in subsequent passes over the sky in order to obtain higher signal-to-noise spectra of the Ly-α.

• *Large-scale-structure bias:* QSO bias has been measured in BOSS via QSO-Ly-α cross-correlation studies to be 3.6 at $z = 2.4$ [233], in agreement with previous measurements [234, 235]. For QSOs at lower redshifts, we project a bias of the form $b(z) = 1.2/D(z)$, where $D(z)$ is the growth factor. At $z > 2.1$, clustering information is computed from the transmitted flux in the Ly-α forest and not directly from correlations between objects; the flux bias of Ly-α absorbers is estimated to be about -0.2 (it is negative because a larger matter density implies a higher absorption and thus a lesser transmitted flux) [236], and is strongly enhanced along the line of sight by redshift-space distortions.

• *Target selection efficiency:* From the first pass of targeting over the sky, we expect to identify 170 QSOs per deg^2 from a sample of 260 targets per deg^2, for a target selection efficiency (including redshift failures) of 65%. For the subsequent passes, the target selection efficiency will be near 100%, as only objects identified as $z > 2.1$ QSOs will be re-observed. After four passes, the average target selection efficiency is therefore of order 80%.

3.4.4 Recent and near-term developments for QSO target selection

During 2015, we focused on building large truth tables of QSOs against which to test current and improved selection algorithms. We developed comprehensive selections of quasars using the deep and multi-epoch SDSS photometry in the Southern Equatorial region called Stripe 82, where variability selections are notably efficient (cf. Sec. 3.4.5 and [237, 224]). These pilot programs led, in particular, to a sample of 18,000 spectroscopically-confirmed QSOs over 120 deg^2 to an extinction-corrected magnitude $g_c < 22.5$, as well as to a smaller but deep sample of 175 deg^{-2} QSOs to $g_c < 23$ over ~ 10 deg^2. They also allowed us to update the QSO luminosity function and make it more robust at faint magnitudes [225]. We are planning further dedicated programs to be run at MMT and AAT to extend the truth tables to $r_c < 23$ as required for DESI. We also applied for a program at MMT to test the current target selection algorithms relying solely upon DECaLS+*WISE* data, in a field where the *WISE* data already have the depth of the final 4-year survey, with the aim of providing the first validation the QSO selection for DESI.

In parallel, work has begun on machine-learning algorithms to take better advantage of the imaging data available for DESI. In BOSS, the XDQSO algorithm [231] led to nearly 20% improvement compared to color cuts and we can reasonably expect a similar increase in the yield of the QSO selection for DESI by the Random Forest algorithm that we are focusing on. These developments have started with DECaLS optical data and existing WISE infrared data. They will be iterated as additional depth is acquired on WISE.

3.4.5 Variability Data Improves Selection of High-Redshift QSOs

Time-domain photometric measurements can enhance QSO selection. They allow us to exploit the intrinsic variability of QSOs [238] to distinguish them from stars of similar colors. They therefore complement the color-selection techniques presented in Sec. 3.4.2. We have so far used variability information extensively to build truth tables against which to test QSO selection. In a second step, we will use variability to select additional high-redshift Ly-α QSOs, for which uniformity of selection across the sky is not required.

Because the accretion region around a quasar is highly compact, its luminosity can vary substantially on timescales ranging from days to years, with a pattern distinct from that seen in variable stars. The time variability of astronomical sources can be described using a measure of the amplitude of the observed magnitude variability Δm as a function of the time delay Δt between two observations. This "structure function" is modeled as a power law parameterized in terms of A, the mean variation amplitude on a one-year time scale (in the observer's reference frame) and γ, the logarithmic slope of the variation amplitude with respect to time: $\Delta m = A(\Delta t)^\gamma$.

We have tested variability techniques in DESI pilot surveys, both in Stripe 82 [237] that was the subject of repeated SDSS observations totaling about 50 epochs, and elsewhere on the sky, where time-domain information was derived from 5-10 epochs of PTF R-band data. As illustrated in Figure 3.18, the segregation between QSOs and stars is much reduced with poorer data, but variability remains competitive. This technique allowed us to identify 30% more QSOs in the Stripe 82 field than with time-averaged optical photometry only [237], and a combined color and variability selection from CFHT and PTF imaging data in the CFHTLS D3 field allowed us to achieve a record-high surface density of 207 QSOs per deg^2 to $g = 23$. The gain relative to the baseline QSO targeting with full *WISE* depth is likely
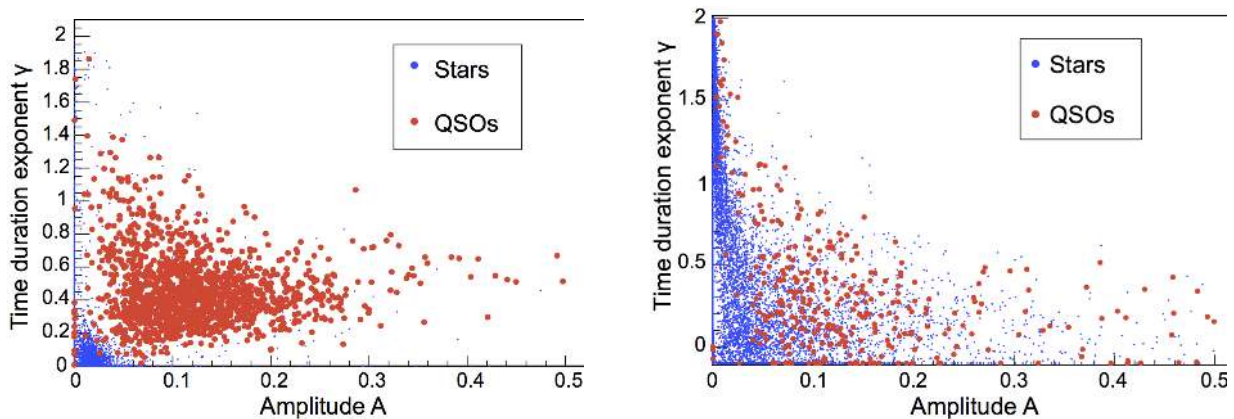
Figure 3.18: *Left panel:* Structure function parameters for 50-epoch *gri* light curves from SDSS in Stripe 82 (left), where the parameters are amplitude (A) and time duration exponent (Γ). *Right panel:* Structure function parameters for the 6-epoch *R* light curves from PTF, where the discriminating power is diminished but still valuable with fewer epochs and filters.

to be less dramatic, and will be evaluated as those data become available. Even with only four epochs of *WISE* data (two stacks per year, two years of observations), preliminary tests indicate that variability information from *WISE* can be used to reduce the contamination of the target sample by about 10%. The full 4-year survey *WISE* will allow 8-epoch light curves, and further gain over current estimates.

Imaging surveys that could provide useful time-domain information for variability selection include the PTF and follow-on iPTF surveys (in the deepest areas of their footprint), the DES survey or the *WISE* survey. Variability is not assumed in our baseline targeting plan, but it is expected to be valuable for selecting the Ly-α QSOs wherever coverage exists.

3.5 Calibration Targets

Target selection is also responsible for providing lists of standard stars for flux calibration, and lists of blank sky locations to be used for modeling the sky.

Main-sequence F stars will be used as the primary spectrophotometric standard stars. These stars are well-described by stellar atmosphere models, making them ideal targets for spectrophotometric calibration at optical wavelengths. A stellar template of appropriate temperature, surface gravity and metallicity will be derived for each star and used to derive the spectral response including the time-varying atmospheric absorption bands.

The selection will be similar to the color-magnitude selection of BOSS to identify low-metallicity targets through a selection in $(u-g), (g-r), (r-i)$, and $(i-z)$ colors. The restrictive BOSS selection yields 10 stars per deg^2; to obtain a larger number of potential targets using the new *grz* photometry, DESI will broaden this selection and include higher metallicity standard stars. With Gaia spectrophotometry of F stars that span a range of metallicity, and upcoming data from SDSS-IV/eBOSS in which a broader selection is applied, we plan to evaluate the value of a mix of lower and higher metallicity F stars to serve as flux calibration standards for DESI. Finally, we will perform a cross-calibration of low-metallicity and higher metallicity F-stars during the commissioning stages of DESI, thus providing validation of the standard star selection.

Blank sky locations will be determined as part of the object detection algorithms applied
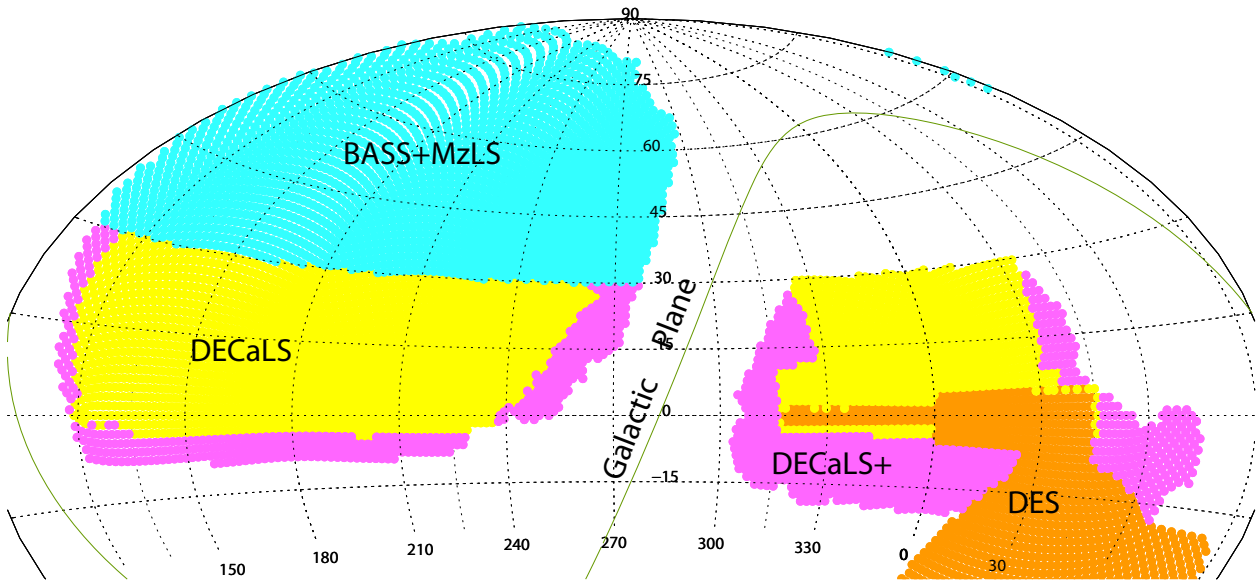
Figure 3.19: The primary imaging surveys that will result in targeting data for the DESI project. The footprint at DEC $\leq +34°$ will be covered using the Dark Energy Camera (DECam) on the Blanco 4m telescope at Cerro Tololo Inter-American Observatory. The Dark Energy Camera Legacy Survey (DECaLS, in yellow), the Dark Energy Survey (DES, in orange), and the extended DECaLS in the North Galactic Cap (DECaLS+, in purple on left) are underway. A proposal for the remaining extended DECaLS in the South Galactic Cap (DECaLS+, in purple on right) will be submitted. Imaging of the North Galactic Cap region at DEC $\geq +34°$ (cyan) will be covered with the 90Prime camera at the Bok 2.3-m telescope in $g-$ and $r-$bands (BASS: the Beijing-Arizona Sky Survey) and with the upgraded MOSAIC-3 camera on the Mayall 4m telescope in z-band (MzLS: the MOSAIC z-band Legacy Survey). Both the Bok and Mayall telescopes are located on Kitt Peak National Observatory.

to the input imaging, ensuring that there are no detectable sources within the fiber diameter in any of the input bands. These will be provided at a density such that every fiber (when possible) will have the option of a blank sky if it isn't otherwise assigned to a science target.

3.6 Baseline Imaging Datasets

The samples described above can be selected given highly-uniform optical imaging data in the g, r, and z bands, as well as all-sky imaging from the *WISE* satellite. The same imaging data for selected science targets will be used to identify calibration targets (standard stars and sky fibers). A combination of three telescopes will be used to provide the baseline targeting data for DESI: the Blanco 4m telescope at Cerro Tololo, the Bok 90-inch and the Mayall 4m telescope at Kitt Peak. The footprints of the primary surveys using these telescopes that will deliver the targeting data are shown in Figure 3.19 and the next three subsections discuss these surveys and their current status in more detail. The status of the *WISE* data is presented in § 3.6.4.

### 3.6.1 Blanco/DECam Surveys (DEC≤34°)

The Dark Energy Camera (DECam) on the Blanco 4m telescope, located at the Cerro Tololo Inter-American Observatory, will provide the optical imaging for targeting over 2/3 of the

DESI footprint, covering both the North and South Galactic Cap regions at Dec $\leq 34°$. Due to the combination of large field of view and high sensitivity from 400-1000 nm, DECam is the most efficient option for obtaining photometry in the g, r, and z bands.

DECam can reach the required depths for DESI targets in modest total exposure times of 100, 100 and 200 sec in g, r, z in median conditions. These data reach required 5σ depths of g=24.0, r=23.4 and z=22.5 for an ELG galaxy with half-light radius of 0.45 arcsec. For a 3-dither observing strategy, accounting for weather loss, DECam is capable of imaging 9000 deg^2 of the DESI footprint to this depth in 81 scheduled nights. These depth estimates have been vetted with grz photometry in the COSMOS field in Spring 2013 (Section 3.3.1).

A public survey, "The DECam Legacy Survey of the SDSS Equatorial Sky" (DESI collaborators D. Schlegel and A. Dey are PIs), has been approved to obtain optical imaging to the required depth over 6200 deg^2. This "DECaLS" survey has been allocated 64 nights spread out over 3 years (2014A to 2017B semesters) as part of the NOAO Large Surveys program. The survey began in August 2014 and has thus far had 30 scheduled nights and 6 Director's discretionary nights (near full moon), during which 23% of the $g + r$ and 49% of the z imaging has been completed. The current coverage is shown in Figure 3.20.

The DECaLS program is making use of other DECam data within the DESI footprint as those data become public. The most significant of these other data sets is from the Dark Energy Survey, which includes a 500 deg^2 contiguous area in the South Galactic Cap.
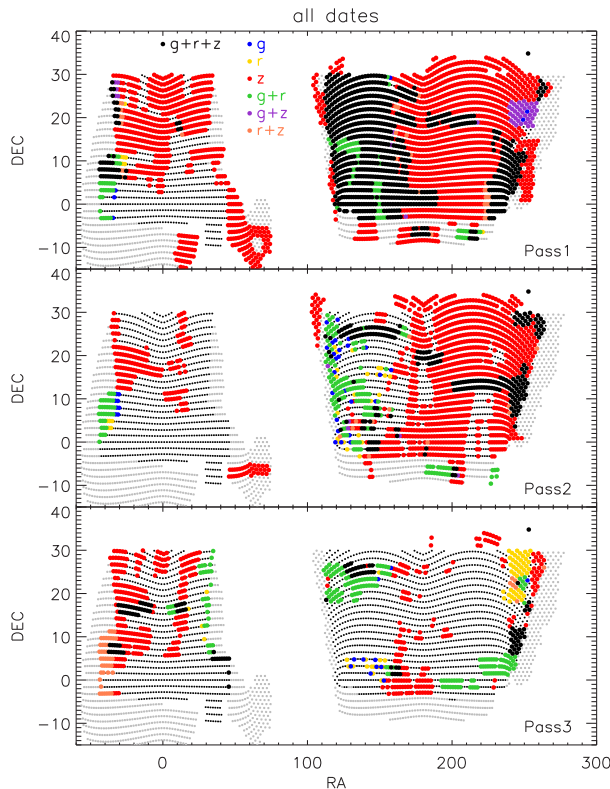
Figure 3.20: *Left panel:* Coverage map of the DECaLS survey through February 2016. The coverage in the g, r and z filters is indicated by the color as blue (g-only), yellow (r-only), green ($g+r$), purple ($g+z$), orange ($r+z$) or black ($g+r+z$). Each panel represents one of the 3 passes, where pass 1 is observed in the best weather conditions.

DECaLS is explicitly not re-imaging that area, and making use of those raw data as the proprietary period expires 12 months after the date of observation.

DECaLS will cover $\approx$2/3 of the planned DESI footprint at Dec $\leq$ 34°. The DECaLS team successfully applied for an 8-night extension (DECaLS+) that will obtain imaging for the remaining 800 deg^2 in the North Galactic Cap. An additional 500 deg^2 in the South Galactic Cap is being observed by the Dark Energy Survey, with those raw data publicly available 12 months after the date of observation. A proposal to observer the remainder of the DESI footprint in the South Galactic Sky will be submitted in future semesters. Data from these programs are treated the same and reprocessed uniformly to ensure consistency for DESI target selection.

The DECam data have been reduced to calibrated images at NOAO and catalogs constructed using the Tractor algorithm (see § 3.8). These catalogs have been used for the DESI target selection tests described elsewhere in this chapter.

3.6.2   Bok/90Prime Survey (DEC$\geq$34°)

The NGC footprint at Dec $\geq$ +34 deg will be observed by the Bok 2.3-m telescope in two optical bands (g and r) for DESI targeting. The Bok Telescope, owned and operated by the University of Arizona, is located on Kitt Peak, adjacent to the Mayall Telescope. The 90Prime instrument is a prime focus 8k×8k CCD imager, with four University of Arizona ITL 4k×4k CCDs that have been thinned and UV optimized with peak QE of 95% at 4000Å [239]. These CCDs were installed in 2009 and have been operating routinely since then. 90Prime delivers a 1.12 deg field of view, with 0.45″ pixels, and 94% filling factor. Typical delivered image quality at the telescope is 1.5″. The g and r-band survey over 5000 deg^2 is projected to require 180 nights of scheduled telescope time for average weather. The throughput and performance in these bands were demonstrated with data in September 2013.

The BASS survey tiles the sky in three passes, similar to the DECaLS survey strategy. At least one of these passes will be observed in photometric conditions (P1) and seeing conditions better than 1.7 arcsec.

The Bok survey (known as the Beijing-Arizona Sky Survey; Zhou Xu and Xiaohui Fan, PIs; see `http://batc.bao.ac.cn/BASS`) was awarded 56 nights in Spring 2015 and 100 nights in each of Spring 2016 and 2017. The Bok survey will target 5500 deg^2 in the NGC, including 500 deg^2 of overlap with the region covered by the DECam surveys in order to understand and correct for any systematic biases in the target selection. The existing Bok g-band filter is well-matched to the DECam g-band filter. The existing Bok r-band filter had a significantly different bandpass as compared to the DECam r-band filter, therefore we acquired a new r-band filter from Asahi that was delivered in April 2015.

The BASS survey began observations in Spring 2015. A number of instrument control software updates, new flexure maps, and new observing tools were implemented that greatly improve the pointing accuracy, focusing of the telescope, and observing efficiency. 15% of the g-band and 2% of the r-band tiles were observed in that semester. It was discovered that those data suffered from defective electronics in the read-out system that introduced A/D errors, gain variations and non-linearities. Those electronics were replaced in September 2015 followed by a recommissioning of the system in Fall 2015.

BASS has been scheduled for the 100 darkest nights in the 2016A semester (January-June), and expects to schedule a comparable number of nights in 2017A. Through February 17, 2016, the survey has completed 10, 10 and 0% of the pass 1, 2, 3 tiles in g-band, and

14, 13, 5% of the tiles in r-band (see Figure 3.21). The raw and calibrated images will be publicly served through the NOAO Science Archive. These data will be included in the Legacy Survey catalogs beginning with Data Release 3 in 2016.

3.6.3   Mayall/MOSAIC Survey (DEC≥34°)

The Mayall z-band Legacy Survey (MzLS) will image the DEC $\geq +34°$ region of the DESI North Galactic footprint. It will use the MOSAIC-3 camera at the prime focus of the 4-meter Mayall telescope at Kitt Peak National Observatory. MzLS will be scheduled for 230 nights during semesters 2016A and 2017A through an agreement between the National Science Foundation and the Department of Energy. 116 of these nights have been scheduled in the 2016A semester, with a survey start on February 2, 2016. The imaging camera has undergone a major upgrade in 2015 to improve its z-band efficiency. The KPNO 4m telescope control system and the imaging camera software have been upgraded for improved operational efficiency. NOAO has purchased a new z-band filter to match the DECam filter bandpass and to thereby minimize any differences between the DECam and MOSAIC z surveys.

The MOSAIC-3 camera is a new version of the prime focus imaging system. This upgrade has made use of the dewar from the MOSAIC-2 camera at CTIO and the MOSAIC-1.1 mechanical system and guider from KPNO. Yale University designed and built a new cold plate for the dewar which it populated with four super-thick (00μm-thick) fully-depleted 4096^2 pixel CCDs with the same 15-micron pitch. The readout system consists of four DESI controllers, one for each CCD that simultaneously reads the four quadrants of each device. These controllers were modified to synchronize to a single clock. The dewar was delivered to NOAO in September 2015 where it was integrated with the MOSAIC-1.1 mechanical enclosure, shutter, filter wheel and acquisition and guider system. This upgraded camera, christened MOSAIC-3, saw first light in October 2015 and underwent further on-sky commissioning runs in November and December 2015. The z-band efficiency has been measured to be improved by 60% as compared to the MOSAIC-1.1 camera.

The MzLS survey tiles the sky in three passes, similar to the DECaLS survey strategy. At least one of these passes will be observed in photometric conditions (P1) and seeing conditions better than 1.3 arcsec. Through March 8, 2016, the survey has completed 23, 19 and 8% of its pass 1, 2 and 3 tiles (see Figure 3.21).

The The MOSAIC z-band survey project will be run similarly to the DECaLS survey, with the initial processing being done using the NOAO pipeline and calibration and catalog construction being carried out at LBNL/NERSC. The raw and pipeline-processed images are public as they are available, typically at the end of each lunar cycle, through the NOAO Science Archive. These data will be included in the Legacy Survey catalogs beginning with Data Release 3 in 2016.

3.6.4   *WISE* All-Sky Survey

Infrared imaging from the Wide-field Infrared Survey Explorer (*WISE*) satellite are critical to the DESI targeting algorithm for LRGs and QSOs. During its primary 7-month mission from through August 2010, *WISE* conducted an all-sky survey in four bands centered at 3.4, 4.6, 12 and 22 μm (known as W1, W2, W3 and W4) [240] 99.99% of the sky was imaged at least 8 times, while regions near the ecliptic poles were observed more than 100
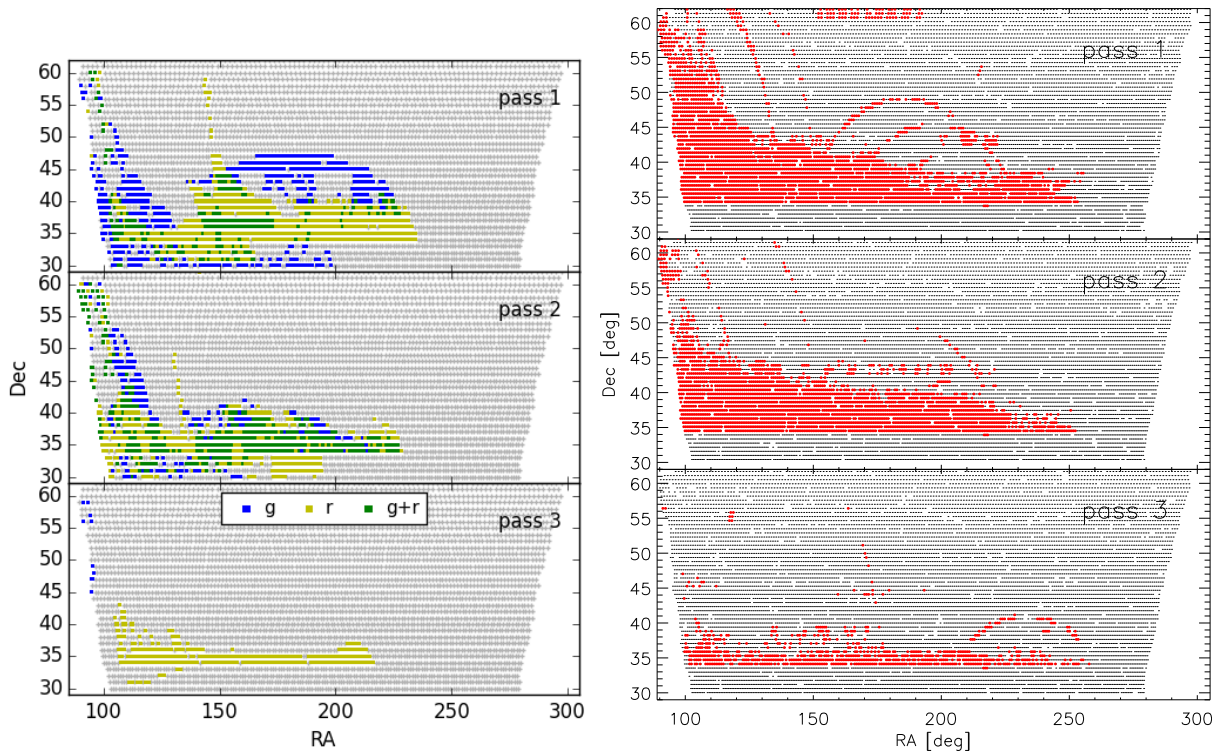
Figure 3.21: *Left panel:* Coverage map of the Bok/BASS survey based on data collected though March 6, 2016, and excluding data prior to the electronics fixes in September 2015. The coverage in the *g* and *r* filters is indicated by the color as blue (*g*-only), yellow (*r*-only) or green (*g*+*r*). Each panel represents one of the 3 passes, where pass 1 is observed in the best weather conditions. *Right panel:* Coverage map of the MzLS *z*-band survey based on data collected though March 6, 2016. The coverage is indicated in each of the three passes.

times. Following the primary 4-band mission, *WISE* continued survey operations in the three shortest bands for 2 months, then the two shortest bands for an additional 4 months for a total of a 13-month mission that completed in September 2011. NASA re-activated the satellite in Fall 2013 and is continuing two-band survey observations for an additional 3 years starting December 1, 2013, as the *NEOWISE* project. The first *NEOWISE* data release occurred on March 25, 2015, the second release will be March 23, 2016, and the final release will be in March 2017.

DESI target selection utilizes the two shortest-wavelength bands at 3.4 (W1) and 4.6 μm (W2). Photometry in these bands is measured using the *the Tractor* algorithm (see Section 3.8) measured on the re-stacked *WISE* and *NEOWISE* Level 1 imaging that retains the intrinsic resolution of the data and are appropriate for preserving the available signal-to-noise [241]. Data Release 1 of the Legacy Survey (DECaLS and *WISE*) made use of the initial 13-month data set, reaching 5-σ limiting magnitudes of 20.0 and 19.3 AB mag in W1 and W2. Data Release 2 made use of approximately twice as much *WISE* data with the first year of *NEOWISE*. The final Legacy Survey catalogs will use the full *WISE* and *NEOWISE* data sets, reaching 0.7 mag fainter than the Legacy Survey Data Release 1 or the *WISE* All-Sky Data Release.

3.7 Additional Imaging Data

Additional imaging data, if available, can supplement the target selection data and may be used, in particular, to improve the selection of the high-redshift Ly-α forest QSO sample. This is because the Ly-α forest analysis is based on the clustering of absorption systems along the line of sight, and therefore does not require a spatially uniform QSO sample. As a result, the QSO target selection can utilize datasets that may not be uniform (in depth, bandpass, or time sampling) over the DESI footprint. In this section, we summarize the key datasets that may contribute to this effort, if they prove to be available. These data sets are not assumed to be available for our baseline target selection plans, but rather should improve the efficiency of targeting higher-redshift ($z > 2.1$) QSOs beyond the baseline targeting strategy presented above.

3.7.1 SDSS

The Sloan Digital Sky Survey [242] has obtained multi-band ($ugriz$) photometry (in photometric conditions) over a 10,000 deg^2 extragalactic footprint in the North Galactic and South Galactic Caps. The Northern Cap and four stripes in the Southern Cap were imaged in 1998-2004. The bulk of the Southern Cap was imaged in 2008-2009, and the SDSS camera was then retired from service in December 2009. The median 5σ magnitude depths for the SDSS $ugriz$ bands are 22.15, 23.13, 22.70, 22.20, and 20.71, respectively, but with substantial variation in depth from seeing. SDSS may provide a reference photometric point for variability selection of high-redshift QSOs, allowing variability over long time baselines to be measured.

3.7.2 PanSTARRS-1

The PanSTARRS-1 (PS1) 3π survey [243] is a transient-sensitive survey designed to observe 30,000 deg^2 of sky over 12 epochs in each of the five $grizy$ filters. The multi-band photometry generated from the co-added exposures reaches depths that are comparable to SDSS in gr and potentially deeper in iz. These depths would potentially be adequate for the DESI BGS and LRG samples, but not the ELG or QSO samples. The PS1 survey completed observations in 2013. The PS1 time-domain photometry may be useful for enhancing the selection of Ly-α QSOs at the brighter magnitudes. The DECaLS survey is currently using a bright star catalog from PS1 to provide initial photometric and astrometric calibration across its footprint. The PS1 co-added imaging and catalogs are not available as of March 2016.

3.7.3 PTF, iPTF, and ZTF

The Palomar Transient Factory (PTF) [244] was a photometric survey designed to find transients via repeated imaging over 20,000 deg^2 in the Northern Hemisphere. In February 2013, the next phase of the program, iPTF (intermediate PTF) began. Both have used the CFH12K camera on the 1.2 m Oschin Telescope at Palomar Observatory, which covers 7.2 deg^2 of sky in a single pointing with a pixel scale of 1.01 arcsec.

Four years of survey operations have so far yielded a total of 5,000 deg^2 in R-band and 1,000 deg^2 in g-band to useful depths for QSO selection based on variability. LBNL is a partner in the PTF and iPTF collaborations, and DESI has access to these data.

An upgraded Zwicky Transient Factory (ZTF) has been funded through an NSF Mid-Scale Innovations Program in Astronomical Sciences. ZTF will utilize the same telescope with a new 46 square-degree imager, beginning operations in 2017. The ZTF survey will cover the entire sky at declinations Dec > -20 deg, including the full DESI footprint. ZTF will operate with a g-band similar to the DECam and Bok g-band, an R-band (Mould-R) that is broader, and potentially an i-band. These data, which will be available to DESI collaboration for the purposes of target selection, are expected to eventually achieve the DESI targeting depths in g and R bands, but likely not before the start of DESI spectroscopic operations. The time sampling of ZTF is planned to be highly non-uniform over the DESI footprint, with different areas of sky covered in different years. Therefore, ZTF is not viable for the baseline DESI target selection, but PTF, iPTF and ZTF may be used to supplement the high-redshift QSO selection for DESI.

3.7.4   CFHT

The Canada-France-Hawaii Telescope (CFHT) is a 3.6–m meter telescope on Mauna Kea, Hawaii. CFHT is a joint facility of the National Research Council of Canada, the Centre National de la Recherche Scientifique of France, and the University of Hawaii. The CFHT prime focus imager MegaCam, a very efficient instrument for imaging large areas of sky, consists of 36 2k×4k e2v CCDs, covering a field of view of 0.97 deg^2 with a pixel scale of 0.185 arcsec per pixel. MegaCam started operations in 2003 and has conducted a number of large imaging surveys, the largest being the CFHT Legacy Survey covering 155 deg^2.

The CFHT community is in discussions with the Euclid consortium and may play a role in providing *ugri* imaging data over the northern Euclid footprint. However, no plan is currently in place. There is an ongoing *u*-band survey ("CFHT-Luau: The CFHT Legacy Survey for the u-band all-sky universe"; A. McConnachie and R. Ibata, PIs) aimed at providing imaging over 4000 deg^2 of the high-Galactic-latitude northern sky, approximately split between the North and South Galactic caps. CFHT-Luau will complete in the 2016B semester (with data becoming public 1 year after observation). $(u - g)$ color selection is an efficient discriminator between low-redshift and high-redshift QSOs. Hence, the CFHT data may be used to supplement the high-redshift Ly-α forest QSO selection in DESI, especially in combination with variability data.

3.7.5   SCUSS

The South Galactic Cap U-band Sky Survey [245] is a survey of 4000 deg^2 in the South Galactic Cap using the 90Prime instrument on the Bok 2.3-m telescope. The survey was a joint project among the Chinese Academy of Sciences, its National Astronomical Observatories unit, and Steward Observatory [5]. The survey was conducted between September 2010 and October 2014 with typical exposure times of 5 minutes per field. The limiting magnitude reached by the data is $u \sim 23$ mag (5σ point source), with some variation due to varying seeing conditions. These data may be used to supplement the high-redshift Ly-α forest QSO selection in DESI, especially in combination with variability data.

---

[5]SCUSS survey http://batc.bao.ac.cn/Uband/

3.8   The Tractor Photometry for Target Selection

The DESI target selection combines photometry from optical imaging and from *WISE*. DESI Imaging Scientist Dustin Lang has developed *the Tractor* forward-modeling approach to perform source extraction on pixel-level data [246]. [6] This is a statistically rigorous approach to fitting the differing PSF and pixel sampling of these data, which is particularly important as the optical data have a typical PSF of ≈ 1 arcsec and the *WISE* PSF is ≈ 6 arcsec.

The Tractor takes as input the individual images from multiple exposures in multiple bands, with different seeing in each. A simultaneous fit is performed for sources to the pixel-level data of all images. Thus, if a source is determined to be a point source, it is photometered as a point source in every band and every exposure. If it is found to be a morphologically extended source, then the same light profile is consistently fit in all images. This produces object fluxes and colors that are consistently-measured across the wide-area imaging surveys input to DESI target selection

For bright objects that were cleanly detected by *WISE* alone, we find our pixel-level measurements to be consistent with catalog-level measurements (see Figure 3.22). However, we are also able to measure the fluxes of significantly fainter objects, as well as to study collections of objects that are blended in the *WISE* imaging but that are resolved in the optical images. Figure 3.23 compares a traditional optical-infrared color-magnitude diagram, based on matching sources between catalogs at different wavelengths, to the results of our *WISE* forced photometry, which requires no such matching. This demonstrates how *The Tractor* increases the color-space information available to DESI targeting.

In general, *The Tractor* improves target selection for all DESI classes by allowing information from low signal-to-noise measurements to be utilized. *The Tractor* is particularly important for QSO targeting. Up to 15% of QSO spectra exhibit broad absorption lines that potentially reduce the measured flux in broadband imaging. High-redshift (Ly-α) QSOs will drop out of some imaging bands completely. Finally, the 5σ optical limit at the extremes of DESI targeting corresponds to a $< 5\sigma$ limit in *WISE* for QSOs (c.f. Sec. 3.4.2). *The Tractor* successfully differentiates between the QSOs that are detected in *WISE*, and the QSOs that in general are not detected (c.f. Figure 3.16), whereas traditional "catalog-matching" approaches would not be successful.

Target selection of LRGs and QSOs for the SDSS-IV/eBOSS, which began observations in July 2014, utilized *The Tractor*. For eBOSS targets, *the Tractor* was applied to obtain forced photometry based upon galaxy profiles measured by the SDSS imaging pipeline. Those profiles were convolved with the *WISE* point-spread function, and then a linear fit was performed on the full set of *WISE* imaging data. The result was a set of flux estimates for all SDSS objects, constructed so that the sum of flux-weighted profiles best matched the *WISE* images. DESI will make use of this same fitting approach, using optical images from surveys being conducted with the DECam, Bok and Mayall telescopes (c.f. Sec. 3.6) in place of the SDSS images.

The Tractor has already been applied to the DECam survey imaging that will be used as part of DESI target selection. This survey, which is known as DECaLS, attained its second release (DR2) of imaging early in 2016. *Tractor* catalogs based on this DR2 data are publicly available[7]. DECaLS DR2 comprises all grz imaging conducted with DECam

---

[6]https://github.com/dstndstn/tractor
[7]http://legacysurvey.org
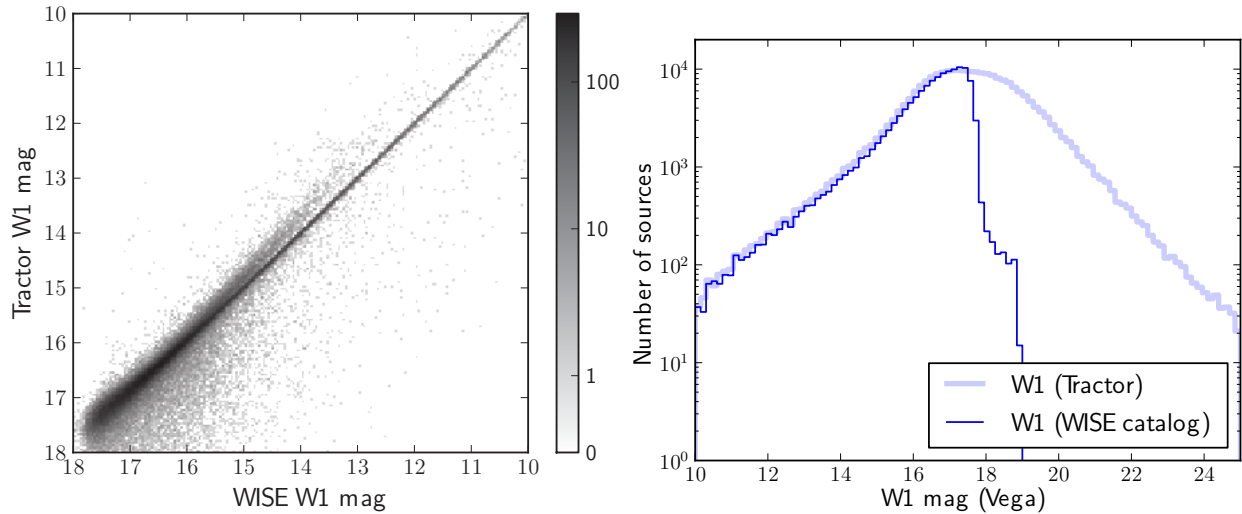
Figure 3.22: Forced photometry results from *the Tractor* code, using information from SDSS detections and light profiles to measure the flux from objects in the *WISE* images to below the *WISE* detection limit. *Left panel:* The results agree for bright objects that are detected in the *WISE* catalog. The widening locus below W1∼14 is due to our photometry treating larger objects as truly extended, in contrast to the point-source-only assumptions in the public *WISE* catalog. *Right panel:* A demonstration of the increased depth made possible from using *the Tractor*. By using optical imaging from SDSS to detect objects, photometry is measured for objects that are well below the *WISE* detection limit.
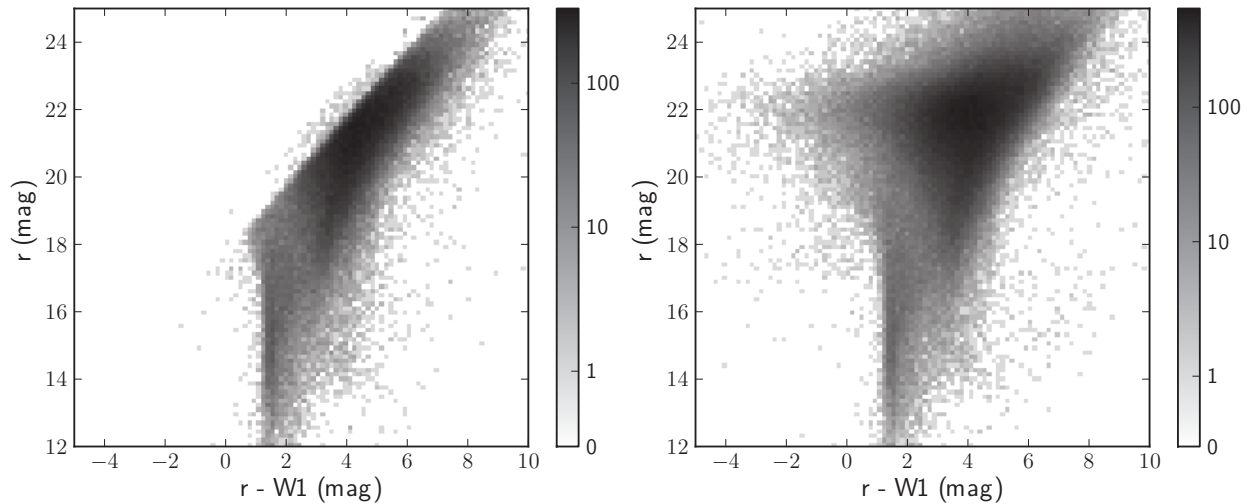
Figure 3.23: Forced photometry results from *the Tractor* code, contrasted with traditional "catalog-matching". *Left:* Color-magnitude diagram from matching SDSS to *WISE* catalogs. Many objects below the *WISE* catalog detection limits are lost. *Right:* Results from forced photometry of the *WISE* images based on SDSS detections. No matching is required, and objects that would be detected in *WISE* at only few-sigma significance can readily provide flux measurements.
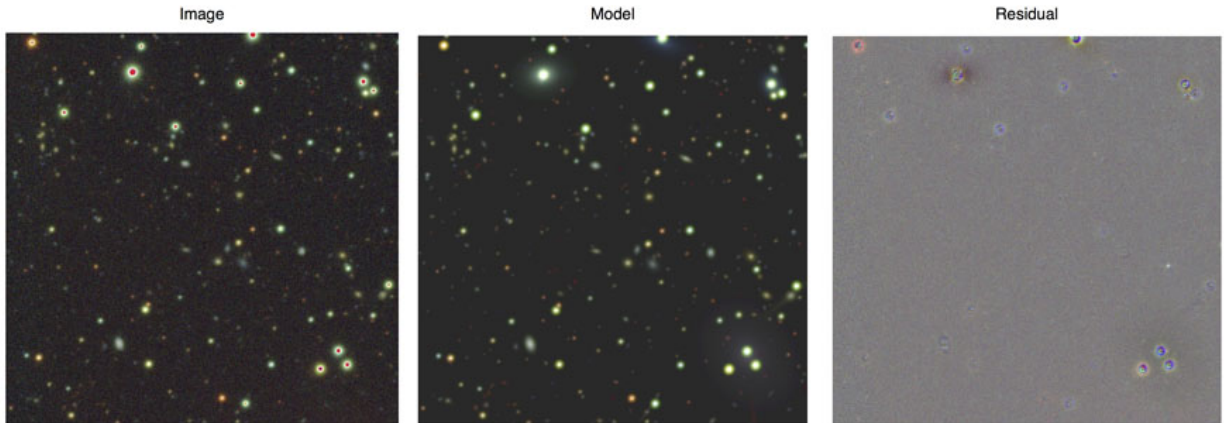
Figure 3.24: An example "brick" covering 0.25×0.25 deg^2 from the DECaLS survey. From left to right, the panels show the actual grz imaging data, the rendered model based on *the Tractor* catalog of the region, and the residual map. *The Tractor* catalog represents an inference-based model of the sky that best fits the observed data.

prior to June 2015 that lies within the DESI footprint. This includes both imaging conducted specifically for DECaLS and public raw imaging re-extracted using *the Tractor*. The co-added images and *Tractor* catalogs are presented in "bricks" of approximate size $0.25° \times 0.25°$ (see Figure 3.24) and DECaLS DR2 contains approximately 260 million unique sources spread over 97,554 bricks.

In total, DECaLS DR2 contains about 2000 deg^2 of imaging in both g- and r-band and roughly 5300 deg^2 in z-band only. 1800 deg^2 has been observed in all three optical filters. DECaLS is on schedule to observe its projected 6200 deg^2 of imaging over 3 years (c.f. Sec. 3.6.1). Based on formal errors from *The Tractor*, the median 5σ point source depths for areas in DECaLS DR2 with full coverage in each band are $g = 24.65$, $r = 23.61$, $z = 22.84$, meeting the depth requirements for DESI target selection. *WISE* fluxes based on forced photometry using *the Tractor* are available for all sources extracted as part of DECaLS DR2.

Catalogs generated by *the Tractor* will be vetted for DESI target selection using a series of image validation tests. Catalogs of galaxies are expected to be generated in a manner that is model-independent across all bands and that should achieve a 5σ, extinction-corrected depth of g=24.0, r=23.4 and z=22.5. 90% of the DESI footprint requires full-depth imaging, but 95% (98%) must be within 0.3 (0.6) magnitudes of full-depth. The photometric system produced by *the Tractor* must be uniform and stable, with $< 1\%$ systematic errors (RMS) in g- and r-band, $< 2\%$ in z-band, and $< 2\%$ from morphological mis-classifications. The z-band image quality must exceed $1.3''$ in at least one pass everywhere in the DESI footprint. The systematic and random errors in astrometry must be less than 30 mas and 90 mas RMS, respectively. In order to facilitate these imaging tests, which are ongoing, *The Tractor* catalogs will ultimately include source positions, fluxes, shape parameters, and morphological quantities that can be used to discriminate extended sources from point-sources, together with errors on these quantities.

4   Survey Design

4.1   Introduction

The DESI instrument will make largest spectroscopic survey to date. The design of the survey is optimized by selecting a footprint that is as large as possible from the Mayall telescope while staying clear of the Milky Way. The survey strategy will establish the order in which the observations will be made. The strategy will be modified in detail by atmospheric conditions, but the overall plan will be established to optimize the best science results for both the complete survey and results from intermediate years.

4.2   Survey Footprint

The DESI survey footprint is defined to be 14,000 square degrees that can be observed spectroscopically from Kitt Peak. This footprint will be one contiguous region selected from the North Galactic Cap (NGC) and one contiguous region in the South Galactic Cap (SGC). The instrumented area of the focal plane is 7.50 square degrees. 14,000 square degrees can be covered nearly completely with little overlap using 2,000 tiles, where each tile represents one DESI observation. We refer to the full 2000-tile coverage of the footprint as a "layer". Five layers with altogether 10,000 tiles covers each coordinate of the footprint with an average of 5.24 fibers. The DESI footprint is formally defined as any position on the sky within 1.605 deg of any of these selected tile centers.

The DESI spectroscopic survey will primarily select targets from catalogs derived from imaging with the Blanco/DECam camera, the Bok/90Prime camera, the Mayall/MOSAIC-2 camera and the Wide-field Infrared Survey Explorer (*WISE*). Although WISE imaging covers the entire sky, the imaging from DECam, the Bok Telescope, and the Mayall telescope impose an external constraint on the DESI footprint, as targets must be selected from large contiguous regions imaged with the same instruments. The Bok and Mayall will provide targeting in the NGC at Dec > +30 deg. The Blanco will provide targeting in both the NGC and SGC at Dec < +30 deg. An area of approximately 800 sq. deg. in the SGC at Dec > +30 (and $-32 < b < -15$) is "orphaned" and excluded from the DESI survey as it would be a small area observed with a different camera.

The footprint is constrained, as well, by the need to avoid regions that would require long exposures due to airmass or dust, by weather patterns at Kitt Peak, and by regions of high stellar density. The resulting footprint is shown in Figure 4.1.

4.3   Field Centers

We refer to "tiling" as the process by which field centers are assigned in a manner to cover the footprint with optimal coverage of each coordinate on the sky. The single-layer tiling of the sky mentioned in Section 4.2 is a preliminary solution that is achieved using the icosahedral tiling [247] with 5762 tile centers distributed on the full sphere[8]. This tiling is very-well matched to the DESI focal plane size. The first layer rotates the above tiling solution by 90 deg in RA. This rotation conveniently puts rows of tile centers along lines of approximately constant declination at the north and south boundaries of the DESI survey. Each of additional layers 2 through 5 have an additional rotation of the tile centers by 1.08

---

[8]`http://neilsloane.com/icosahedral.codes/`
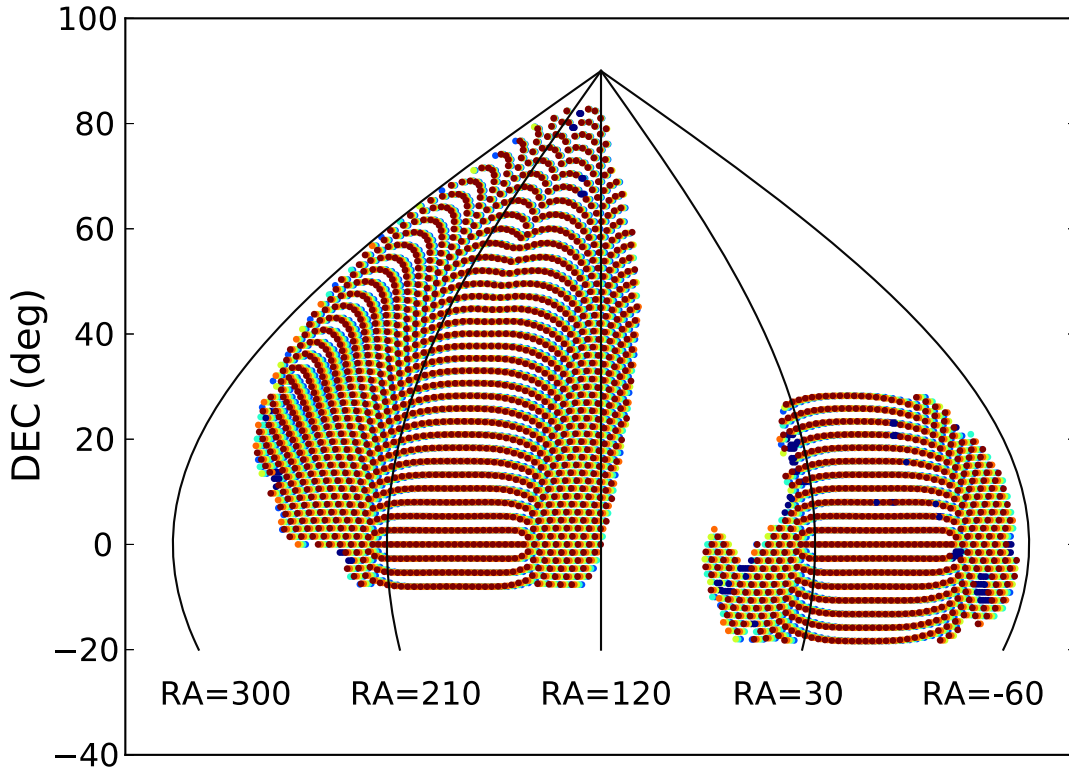
Figure 4.1: Tile centers for the DESI footprint in an equal-area projection. Declination limits are imposed at $-8.2 <$ Dec in the NGC (left), and $-18.4 <$ Dec $< +30$ in the SGC (right). Approximately 1% of tiles have exposure factors larger than 2.5 (shown in blue), but are included to avoid unwanted holes in the footprint. The five layers are shown in separate (but overlapping) colors. The spots indicate the centers of focal plane positions and overlap between layers. The symbols do not represent the size of the area in the sky subtended by the focal plane. Every location inside the footprint is within reach of a fiber, on average, 5.24 times during the survey.

deg in RA. This gives large dithers on most of the sky (except at the pole, which is not in the DESI footprint), thus filling the gaps in the focal plane with subsequent visits. Non-uniformity in coverage could artificially introduce structure in the targeting of LSS-tracers; alternative tilings based on the same first layer but with subsequent layers obtained with more disparate rotations will be further studied for possible improvements to the uniformity.

A descoped instrument has been considered which would conduct the DESI survey over 9000 square degrees rather than 14,000 square degrees. This descoped instrument would populate only six of the 10 wedges on the focal plane with 3000 instead of 5000 fibers. The populated wedges are best arranged in a "Pacman" format. A different tiling solution is necessary for covering a smaller survey area with the same mean coverage per survey area. First, 240 tile centers are placed on the celestial equator uniformly separated in RA. Stripes of tiles are then placed on lines of constant celestial latitude spaced every 2.765 deg. At each stripe, the number of tiles is reduced by the factor cos(Dec) from the 240 placed on the celestial equator. This results in a tiling solution with similar uniformity and coverage statistics as the baseline survey, with 4% more tiles than would be necessary under the assumption of a simple scaling with focal plane area.

The pattern of fiber positioners in the focal plane is shown in Figure 4.2. Combining

this with the tiling gives a purely geometric measure of the coverage for each position within the DESI footprint. The distribution of this coverage is shown in Figure 4.3 and in Table 4.1. The average coverage is about 5.1 fibers available per coordinate, with only 3.5% of the footprint having a coverage of less than 3 fibers. The mean relative to the value of 5.24 reported earlier is slightly reduced due to increase of edge effects over the smaller area tested. The edges of the footprint have the least coverage. The results of a similar study for the reduced "Pacman" focal plane are shown in the right hand panel of Figure 4.3.
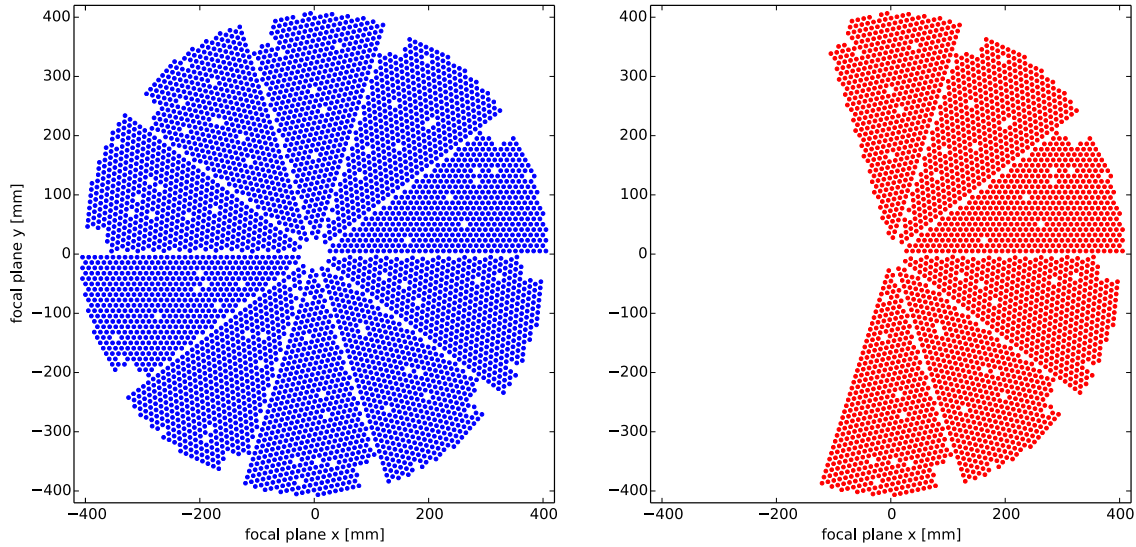
Figure 4.2: *Left:* Fiber positioner locations for the full DESI instrument. *Right:* The locations for the reduced instrument "pacman" configuration. "Missing" positioner locations are for the guide-focus arrays (square regions) and fiducial markers for the fiber view camera.
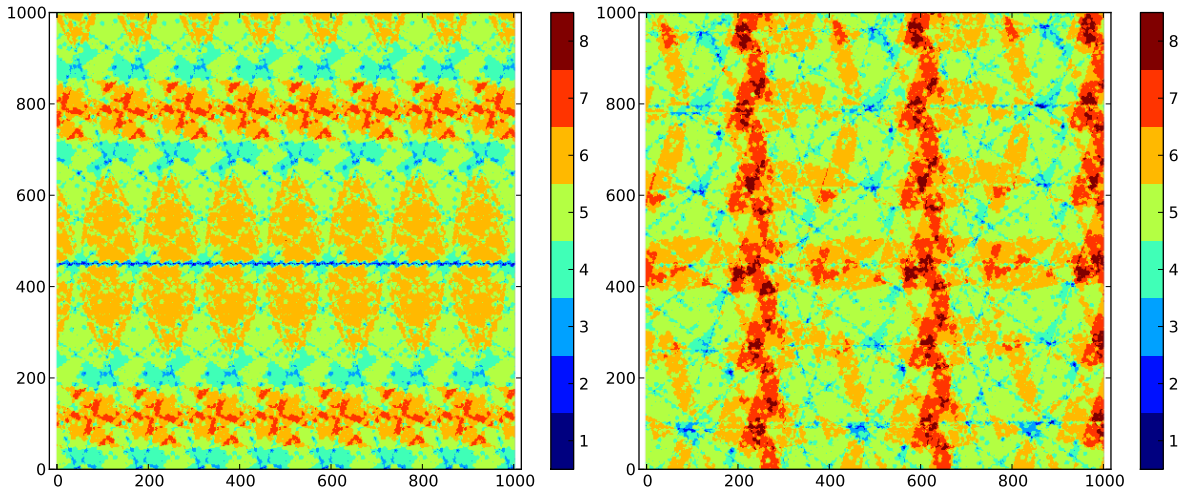
Figure 4.3: Coverage pattern on the sky after five layers over a 4 degree by 4 degree patch. This is shown for a region away from the edges of the footprint. *Left:* The fully-populated focal plane with 5000 fibers. *Right:* The reduced focal plane with 3000 fibers.

Table 4.1: The fraction of the footprint covered by 1, 2, 3, ... 8 fibers. The first row shows the results using all five layers in the baseline survey. The second row shows the results using just the four layers that include LRG and quasar targets. The mean is slightly decreased and the rms slightly increased by edge effects.

Coverage	1	2	3	4	5	6	7	8	Mean	RMS
All five layers	0.016	0.019	0.040	0.155	0.424	0.279	0.055	0.009	5.06	1.175
Four layers only	0.021	0.037	0.152	0.482	0.462	0.040	0.004	0.000	4.04	1.012

4.4   Observation Strategy

4.4.1   Sequence of Observations

The placement of field centers presented in Section 4.3 is designed to cover the footprint in five independent tilings. Given the 1940 hours of scheduled time each year, roughly 20% (390 hours) will occur under conditions when the moon is above the horizon and the remainder under dark conditions. Each year, 20% of the fields in a full independent tiling of 2000 field centers will be observed using the scheduled time in grey conditions. This layer is planned to include only ELG targets because their spectral features are predominantly found at redder wavelengths and redshift success rates are less susceptible to increased sky background from the moon. On the other hand, the darkest 80% of the scheduled time (1550 hours) will be used to observe the QSO and LRG targets at highest priority, leaving the remaining science fibers for ELG targets.

There remains additional freedom to determine the order in which the tiles over the four dark time layers are observed. Full simulations of the program will be used to determine the optimal approach. The simulations will factor in seeing, transparency and weather variations for each exposure via Monte Carlo simulations to predict the quality of spectra and the variations in final survey areal coverage. Each exposure will be tuned to a grid of targets parameterized by magnitude and redshift using an exposure time calculator that approximates the sensitivity of the instrument. Weather conditions will be mocked using monthly statistics at Kitt Peak and the results will be used to determine likely redshift success rates over all target classes. A description of these simulations is found in the document DESI-1658. The approach that optimizes intermediate and final cosmology results will be chosen.

We provide a baseline strategy in the accompanying document on long-term strategy. This program is assembled without consideration of weather and other variables. The survey is designed to get an early complete sample over 10% of the footprint as early as possible. The survey also provides distinct milestones for data products and cosmological analysis at the end of each year.

Finally, we will investigate the target strategies, exposure depths, quality of data, and expected spectroscopic completeness during a phase of survey validation. Survey validation will occur during the end of commissioning before the full survey begins. The baseline program for this phase of the project is presented in the accompanying document on survey validation.

4.4.2   Exposure Times and Margin

Over five years, DESI is projected to observe 14,000 sq. deg. of the footprint presented in Section 4.2. The exact subset of this footprint to be observed will be contiguous regions in each of the NGC and the SGC that best fit the expected allocation of time. We have simulated the choice of final tile centers and the average exposure times according to an observing schedule of 1940 hours of dark and grey time per year as defined in the Site Alternatives study (DESI-311). The simulation includes a two minute overhead between fields and variations in exposure time for each field due to airmass and Galactic dust extinction. All exposure times are split into two separate exposures (with one minute of read time). This split limits the number of cosmic rays in an individual exposure, and also effectively maximize the S/N in variable sky conditions. The split is not assumed in the baseline for spectroscopic depth and completeness, so the time per field is larger in these simulations than in the baseline design. The accumulated S/N will be measured by the exposure time calculator (see the DESI Performance Studies in the Instrument FDR). We project that 57% of the scheduled time will deliver usable data, where "usable data" is assumed in conditions when the dome is open and seeing is better than 1.5 arcsec. Although DESI will observe when the seeing is worse than 1.5 arcsec, those data have been ignored in these estimates of survey duration.

We simulate the full suite of observations accounting for airmass and Galactic dust extinction by choosing an hour angle for each field that maximizes the overall survey depth while fitting into the allocated time. Exposure times are estimated for each field to produce uniform depth in dust-extinction and atmosphere-extinction corrected spectra. In preliminary estimates, we assume the same dependence of S/N on airmass as was measured with BOSS, and degradation in S/N due to Galactic extinction for the sky-noise-limited case of the faintest targets. In future iterations, we will include a more sophisticated interpretation of redshift success rate for representative targets, thus accounting for the wavelength-dependent S/N estimates of each target class. For the 14,000 sq. deg. footprint observed with 10,000 tiles, we find an average exposure time of 1800 seconds. Scaling this to an observation taken at zenith with no Galactic dust extinction (as shown in the figure in the DESI Performance Studies in the Instrument FDR) produces an equivalent exposure time of 1226 seconds. In other words, each exposure will have a S/N equivalent to a 1226 second exposure taken at zenith, under photometric conditions, median sky brightness and median seeing. As explained in Simulations Section of the Instrument FDR this fiducial exposure time of 1226 seconds allows the 1000 second exposures that are predicted to produce the required redshift success rates for each DESI target class. This projection leaves a 22% margin in exposure time for worse-than-projected weather, throughput performance, instrument downtime, or other factors that could slow the pace of the survey.

Similarly, we have estimated the average and fiducial exposure times for the reduced focal plane of the DESI KPP survey. The "Pacman" tiling of Section 4.2 leads to an average exposure time of 1700 seconds for 10,600 tile centers covering 9,000 sq. deg. Even though the average exposure time is somewhat lower than the 14,000 sq. deg. survey, the fiducial exposure time of 1270 seconds is actually larger because the average field in a 9,000 sq. deg. program lies at lower airmass and lower Galactic extinction than the average field in a 14,000 sq. deg. program. The projected margin for the 9,000 sq. deg. KPP survey is 27%.

4.5 The Bright Galaxy and Milky Way Surveys

4.5.1 Introduction

A portion of DESI operations will be affected by increased sky brightness from the moon, so as to make conditions unsuitable for observing the targets above $z = 0.6$. DESI expects to observe in the darkest 21 nights of the month, but some of those nights are affected in part by moon, adding up to about 440 hours per year of time. Assuming the same average weather statistics used in planning for dark time, we expect 250 hours per year on average of open-dome bright time. During this time, the DESI collaboration will conduct a survey of bright galaxies which will increase performance for the cosmology goals. This Bright Galaxy Survey (BGS) will be the primary bright-time survey program. In addition, the density of fibers in the DESI focal plane will enable a simultaneous survey of Milky Way Stars (The Milky Way Survey; MWS) during bright time. The MWS will target some of the oldest stars in the Galaxy with the goal of understanding the mass distribution, formation and evolution of the Galaxy. We refer to these two combined programs as the Bright Time Survey (BTS).

4.5.2 Survey Footprint

The Bright Time Survey will use the same 14,000 square degree footprint as the dark time project. This will enable the BTS to benefit from the optimization of the dark time footprint for observability. The BGS targets will be selected from the same imaging data as the dark time targets. The MWS will use Gaia photometry and proper motions for target selection. The Gaia survey is all-sky, and so covers the DESI 14,000 square degree footprint.

4.5.3 Field Centers

The BTS will use the same tiling pattern as the DESI Key Project, but with only 3 layers totaling 6000 tiles. There are roughly 1400 galaxies per square degree to $r = 20.0$. With 4500 science fibers per tile, the BTS will place about 27 million fibers, more than the ~ 20 million BGS targets. However, the presence of clustering and Poisson fluctuations of bright galaxies implies that we must incur these extra layers if we want to achieve a higher completeness. For fiber assignment, BGS targets are divided into two priorities; brighter targets with $r < 19.5$ (~ 800 deg^{-2}) receive high priority, while fainter $19.5 < r < 20.0$ (~ 600 deg^{-2}) targets receive secondary priority. Preliminary simulations of DESI fiber assignments using this priority scheme yields 3-layer completeness values of 92% for the bright sample and 77% for the faint sample, for an overall fiber completeness of 86%, or roughly 17M targets.

There are about 600 stars with effective temperatures higher than 4700 K per square degree to $r = 18$ at Galactic latitude greater than 40 degrees from the equator. The DESI focal plane is 7.5 square degrees, so at each layer there will be many fibers available for the MWS.

4.5.4 Observation Strategy

Completing 6000 tiles in the 1250 hours of available open-dome time indicates an average time of 12.5 minutes per tile. Survey simulations accounting for the increased exposure time required as a function of airmass and extinction indicate that we would have 400 seconds available for a reference exposure at unit airmass and zero extinction. We are planning for

a 300 second reference exposure, therefore leaving a 33% margin. Our spectral simulations (§3.1 and Figure 3.3) indicate that a 5-minute exposure will yield a redshift success of 97% for galaxies down to $r = 19.5$, and 92% for the fainter $19.5 < r < 20.0$ sample.

For stars, 5 minute exposures will result in spectra with S/N per Angstrom of 14 at $\lambda > 650$ nm for stars of r magnitude 16.5-18, depending on their spectral energy distributions. Spectra of that quality are sufficient to yield radial velocity and chemical abundance information.

Because the BTS needs only three layers, it will be possible to combine multiple exposures for fainter objects for higher S/N. For example, it would be possible to re-expose many of the 5% of BGS targets that fail to achieve a redshift in the first two layers. We will perform fiber assignment simulations that combine the MWS and BGS samples to determine the optimal way to assign fibers that accounts for galaxy clustering and the variation in stellar density across the footprint, and which achieves maximum redshift and radial velocity completeness for faint targets.

With this basic strategy we expect to obtain spectra of roughly 10 million galaxies in the BGS and 10 million stars in the MWS. More simulations of the BTS are required to determine how to prioritize sky coverage versus completeness to enable early science. The BTS simulations will use the same survey simulation code as the dark time program, adapting it as required to account for scheduling around lunar phase and separation angle between the field and the moon.

Acknowledgements

References

[1]   S. Perlmutter et al. "Measurements of Omega and Lambda from 42 High-Redshift Super-novae". In: *Astrophys. J.* 517 (June 1999), pp. 565–586. eprint: `astro-ph/9812133`.

[2]   A. G. Riess et al. "Observational Evidence from Supernovae for an Accelerating Universe and a Cosmological Constant". In: *Astron. J.* 116 (Sept. 1998), pp. 1009–1038. eprint: `astro-ph/9805201`.

[3]   M. Levi et al. "The DESI Experiment, a whitepaper for Snowmass 2013". In: *ArXiv e-prints* (Aug. 2013). arXiv:`1308.0847 [astro-ph.CO]`.

[4]   A. Albrecht et al. "Report of the Dark Energy Task Force". In: *ArXiv Astrophysics e-prints* (Sept. 2006). eprint: `astro-ph/0609591`.

[5]   Daniel J. Eisenstein and Wayne Hu. "Baryonic features in the matter transfer function". In: *Astrophys.J.* 496 (1998), p. 605. arXiv:`astro-ph/9709112 [astro-ph]`.

[6]   L. Anderson et al. "The clustering of galaxies in the SDSS-III Baryon Oscillation Spectro-scopic Survey: baryon acoustic oscillations in the Data Releases 10 and 11 Galaxy samples". In: *Mon. Not. R. Astron. Soc.* 441 (June 2014), pp. 24–62. arXiv:`1312.4877`.

[7]   A. J. Cuesta et al. "The clustering of galaxies in the SDSS-III Baryon Oscillation Spectro-scopic Survey: baryon acoustic oscillations in the correlation function of LOWZ and CMASS galaxies in Data Release 12". In: *Mon. Not. R. Astron. Soc.* 457 (Apr. 2016), pp. 1770–1785. arXiv:`1509.06371`.

[8]   F. Beutler et al. "The 6dF Galaxy Survey: baryon acoustic oscillations and the local Hubble constant". In: *Mon. Not. R. Astron. Soc.* 416 (Oct. 2011), pp. 3017–3032. arXiv:`1106.3366 [astro-ph.CO]`.

[9]   C. Blake et al. "The WiggleZ Dark Energy Survey: joint measurements of the expansion and growth history at $z \leq 1$". In: *Mon. Not. R. Astron. Soc.* 425 (Sept. 2012), pp. 405–414. arXiv:`1204.3674 [astro-ph.CO]`.

[10] D. J. Eisenstein et al. "Improving Cosmological Distance Measurements by Reconstruction of the Baryon Acoustic Peak". In: *Astrophys. J.* 664 (Aug. 2007), pp. 675–679. eprint: `arXiv: astro-ph/0604362`.

[11] N. Padmanabhan et al. "A 2 per cent distance to $z = 0.35$ by reconstructing baryon acoustic oscillations - I. Methods and application to the Sloan Digital Sky Survey". In: *Mon. Not. R. Astron. Soc.* 427 (Dec. 2012), pp. 2132–2145. arXiv:`1202.0090 [astro-ph.CO]`.

[12] A. J. Ross et al. "The clustering of galaxies in the SDSS-III Baryon Oscillation Spectroscopic Survey: analysis of potential systematics". In: *Mon. Not. R. Astron. Soc.* 424 (July 2012), pp. 564–590. arXiv:`1203.6499 [astro-ph.CO]`.

[13] B. Leistedt and H. V. Peiris. "Exploiting the full potential of photometric quasar surveys: optimal power spectra through blind mitigation of systematics". In: *Mon. Not. R. Astron. Soc.* 444 (Oct. 2014), pp. 2–14. arXiv:`1404.6530`.

[14] Planck Collaboration et al. "Planck 2013 results. XVI. Cosmological parameters". In: *ArXiv e-prints* (Mar. 2013). arXiv:`1303.5076 [astro-ph.CO]`.

[15] Planck Collaboration et al. "Planck 2015 results. I. Overview of products and scientific results". In: *ArXiv e-prints* (Feb. 2015). arXiv:`1502.01582`.

[16] Planck Collaboration et al. "Planck 2015 results. XIII. Cosmological parameters". In: *ArXiv e-prints* (Feb. 2015). arXiv:1502.01589.

[17] D. Eisenstein and M. White. "Theoretical uncertainty in baryon oscillations". In: *Phys.-Rev. D* 70.10, 103523 (Nov. 2004), p. 103523. eprint: `arXiv:astro-ph/0407539`.

[18] H.-J. Seo et al. "Nonlinear Structure Formation and the Acoustic Scale". In: *Astrophys. J.* 686 (Oct. 2008), pp. 13–24. arXiv:0805.0117.

[19] M. Crocce and R. Scoccimarro. "Nonlinear evolution of baryon acoustic oscillations". In: *Phys. Rev. D* 77.2 (Jan. 2008), pp. 023533–+. eprint: `arXiv:0704.2783`.

[20] R. E. Smith, R. Scoccimarro, and R. K. Sheth. "Motion of the acoustic peak in the correlation function". In: *Phys. Rev. D* 77.4 (Feb. 2008), pp. 043525–+. eprint: `arXiv:astro-ph/0703620`.

[21] N. Padmanabhan and M. White. "Calibrating the baryon oscillation ruler for matter and halos". In: *Phys. Rev. D* 80.6, 063508 (Sept. 2009), p. 063508. arXiv:0906.1198 [astro-ph.CO].

[22] H.-J. Seo et al. "High-precision Predictions for the Acoustic Scale in the Nonlinear Regime". In: *Astrophys. J.* 720 (Sept. 2010), pp. 1650–1667. arXiv:0910.5005 [astro-ph.CO].

[23] K. T. Mehta et al. "Galaxy Bias and Its Effects on the Baryon Acoustic Oscillation Measurements". In: *Astrophys. J.* 734, 94 (June 2011), p. 94. arXiv:1104.1178 [astro-ph.CO].

[24] B. D. Sherwin and M. Zaldarriaga. "Shift of the baryon acoustic oscillation scale: A simple physical picture". In: *Phys. Rev. D* 85.10, 103523 (May 2012), p. 103523. arXiv:1202.3998 [astro-ph.CO].

[25] D. Tseliakhovich and C. Hirata. "Relative velocity of dark matter and baryonic fluids and the formation of the first structures". In: *Phys. Rev. D* 82.8, 083520 (Oct. 2010), p. 083520. arXiv:1005.2416 [astro-ph.CO].

[26] J. Blazek, J. E. McEwen, and C. M. Hirata. "Streaming velocities and the baryon-acoustic oscillation scale". In: *ArXiv e-prints* (Oct. 2015). arXiv:1510.03554.

[27] J. Yoo, N. Dalal, and U. Seljak. "Supersonic relative velocity effect on the baryonic acoustic oscillation measurements". In: *J. Cosmology Astropart. Phys.* 7, 018 (July 2011), p. 18. arXiv:1105.3732 [astro-ph.CO].

[28] Z. Slepian and D. J. Eisenstein. "On the signature of the baryon-dark matter relative velocity in the two- and three-point galaxy correlation functions". In: *Mon. Not. R. Astron. Soc.* 448 (Mar. 2015), pp. 9–26. arXiv:1411.4052.

[29] L. Anderson et al. "The clustering of galaxies in the SDSS-III Baryon Oscillation Spectroscopic Survey: Baryon Acoustic Oscillations in the Data Release 9 Spectroscopic Galaxy Sample". In: *ArXiv e-prints* (Mar. 2012). arXiv:1203.6594 [astro-ph.CO].

[30] C. L. Reichardt et al. "New Limits on Early Dark Energy from the South Pole Telescope". In: *Astrophys. J. Lett.* 749, L9 (Apr. 2012), p. L9. arXiv:1110.5328 [astro-ph.CO].

[31] U. Alam. "Constraining Perturbative Early Dark Energy with Current Observations". In: *Astrophys. J.* 714 (May 2010), pp. 1460–1469. arXiv:1003.1259 [astro-ph.CO].

[32] J.-Q. Xia and M. Viel. "Early dark energy at high redshifts: status and perspectives". In: *J. Cosmology Astropart. Phys.* 4, 002 (Apr. 2009), p. 2. arXiv:0901.0605 [astro-ph.CO].

[33] E. V. Linder and G. Robbers. "Shifting the Universe: early dark energy and standard rulers". In: *J. Cosmology Astropart. Phys.* 6, 004 (June 2008), p. 4. arXiv:0803.2877.

[34] M. Doran and G. Robbers. "Early dark energy cosmologies". In: *J. Cosmology Astropart.-Phys.* 6, 026 (June 2006), p. 26. eprint: `arXiv:astro-ph/0601544`.

[35] M. Doran, J.-M. Schwindt, and C. Wetterich. "Structure formation and the time dependence of quintessence". In: *Phys. Rev. D* 64.12 (Dec. 2001), p. 123520. eprint: `arXiv:astro-ph/0107525`.

[36] R. Lynds. "The Absorption-Line Spectrum of 4c 05.34". In: *Astrophys. J. Lett.* 164 (Mar. 1971), pp. L73+.

[37] P. McDonald. "Toward a Measurement of the Cosmological Geometry at z ∼ 2: Predicting Lyα Forest Correlation in Three Dimensions and the Potential of Future Data Sets". In: *Astrophys. J.* 585 (Mar. 2003), pp. 34–51. eprint: `arXiv:astro-ph/0108064`.

[38] A. Slosar et al. "The acoustic peak in the Lyman alpha forest". In: *J. Cosmology Astropart.-Phys.* 10 (Oct. 2009), pp. 19–+. arXiv:`0906.2414` [`astro-ph.CO`].

[39] U. Seljak. "Bias, redshift space distortions and primordial nongaussianity of nonlinear transformations: application to Ly-α forest". In: *J. Cosmology Astropart. Phys.* 3, 004 (Mar. 2012), p. 4. arXiv:`1201.0594` [`astro-ph.CO`].

[40] M. White. "The Ly-a forest". In: *The Davis Meeting On Cosmic Inflation. 2003 March 22-25, Davis CA., p.18.* Mar. 2003.

[41] P. McDonald and D. J. Eisenstein. "Dark energy and curvature from a future baryonic acoustic oscillation survey using the Lyman-α forest". In: *Phys. Rev. D* 76.6 (Sept. 2007), pp. 063009–+. eprint: `arXiv:astro-ph/0607122`.

[42] M. McQuinn and M. White. "On estimating Lyα forest correlations between multiple sightlines". In: *Mon. Not. R. Astron. Soc.* 415 (Aug. 2011), pp. 2257–2269. arXiv:`1102.1752` [`astro-ph.CO`].

[43] A. Slosar et al. "The Lyman-α forest in three dimensions: measurements of large scale flux correlations from BOSS 1st-year data". In: *J. Cosmology Astropart. Phys.* 9 (Sept. 2011), pp. 1–+. arXiv:`1104.5244` [`astro-ph.CO`].

[44] N. G. Busca et al. "Baryon acoustic oscillations in the Lyα forest of BOSS quasars". In: *Astron. Astrophys.* 552, A96 (Apr. 2013), A96. arXiv:`1211.2616` [`astro-ph.CO`].

[45] A. Slosar et al. "Measurement of baryon acoustic oscillations in the Lyman-α forest fluctuations in BOSS data release 9". In: *J. Cosmology Astropart. Phys.* 4, 026 (Apr. 2013), p. 26. arXiv:`1301.3459` [`astro-ph.CO`].

[46] D. Kirkby et al. "Fitting methods for baryon acoustic oscillations in the Lyman-α forest fluctuations in BOSS data release 9". In: *J. Cosmology Astropart. Phys.* 3, 024 (Mar. 2013), p. 24. arXiv:`1301.3456` [`astro-ph.CO`].

[47] T. Delubac et al. "Baryon Acoustic Oscillations in the Ly{\alpha} forest of BOSS DR11 quasars". In: *ArXiv e-prints* (Apr. 2014). arXiv:`1404.1801`.

[48] M. White et al. "Particle Mesh Simulations of the Lyα Forest and the Signature of Baryon Acoustic Oscillations in the Intergalactic Medium". In: *Astrophys. J.* 713 (Apr. 2010), pp. 383–393. arXiv:`0911.5341`.

[49] M. McQuinn et al. "The signatures of large-scale temperature and intensity fluctuations in the Lyman α forest". In: *Mon. Not. R. Astron. Soc.* 415 (July 2011), pp. 977–992. arXiv:`1010.5250` [`astro-ph.CO`].

[50]   M. McQuinn and G. Worseck. "The case against large intensity fluctuations in the z ∼ 2.5 He II Lyα forest". In: *Mon. Not. R. Astron. Soc.* 440 (May 2014), pp. 2406–2418. arXiv:1306. 4985.

[51]   A. Pontzen. "Scale-dependent bias in the baryonic-acoustic-oscillation-scale intergalactic neutral hydrogen". In: *Phys. Rev. D* 89.8, 083010 (Apr. 2014), p. 083010. arXiv:1402.0506.

[52]   S. Gontcho A Gontcho, J. Miralda-Escudé, and N. G. Busca. "On the effect of the ionizing background on the Lyα forest autocorrelation function". In: *Mon. Not. R. Astron. Soc.* 442 (July 2014), pp. 187–195.

[53]   M. M. Pieri. "The C IV Forest as a Probe of Baryon Acoustic Oscillations". In: *ArXiv e-prints* (Apr. 2014). arXiv:1404.4569.

[54]   P. McDonald and A. Roy. "Clustering of dark matter tracers: generalizing bias for the coming era of precision LSS". In: *J. Cosmology Astropart. Phys.* 8, 020 (Aug. 2009), p. 20. arXiv:0902.0991 [astro-ph.CO].

[55]   T. Baldauf et al. "Evidence for quadratic tidal tensor bias from the halo bispectrum". In: *Phys. Rev. D* 86.8, 083540 (Oct. 2012), p. 083540. arXiv:1201.4827 [astro-ph.CO].

[56]   P. McDonald. "Clustering of dark matter tracers: Renormalizing the bias parameters". In: *Phys. Rev. D* 74.10 (Nov. 2006), pp. 103512–+.

[57]   U. Seljak and P. McDonald. "Distribution function approach to redshift space distortions". In: *J. Cosmology Astropart. Phys.* 11, 039 (Nov. 2011), p. 39. arXiv:1109.1888 [astro-ph.CO].

[58]   Z. Vlah et al. "Distribution function approach to redshift space distortions. Part IV: perturbation theory applied to dark matter". In: *J. Cosmology Astropart. Phys.* 11, 009 (Nov. 2012), p. 9. arXiv:1207.0839 [astro-ph.CO].

[59]   T. Okumura, U. Seljak, and V. Desjacques. "Distribution function approach to redshift space distortions. Part III: halos and galaxies". In: *J. Cosmology Astropart. Phys.* 11, 014 (Nov. 2012), p. 14. arXiv:1206.4070 [astro-ph.CO].

[60]   R. Reyes et al. "Confirmation of general relativity on large scales from weak lensing and galaxy velocities". In: *Nature* 464 (Mar. 2010), pp. 256–258. arXiv:1003.2185 [astro-ph.CO].

[61]   Y.-S. Song et al. "Complementarity of weak lensing and peculiar velocity measurements in testing general relativity". In: *Phys. Rev. D* 84.8, 083523 (Oct. 2011), p. 083523. arXiv:1011. 2106 [astro-ph.CO].

[62]   N. Kaiser. "Clustering in real space and in redshift space". In: *Mon. Not. R. Astron. Soc.* 227 (July 1987), pp. 1–21.

[63]   A. Stril, R. N. Cahn, and E. V. Linder. "Testing standard cosmology with large-scale structure". In: *Mon. Not. R. Astron. Soc.* 404 (May 2010), pp. 239–246. arXiv:0910.1833 [astro-ph.CO].

[64]   D. Huterer et al. "Growth of Cosmic Structure: Probing Dark Energy Beyond Expansion". In: *ArXiv e-prints* (Sept. 2013). arXiv:1309.5385 [astro-ph.CO].

[65]   N. Hamaus, U. Seljak, and V. Desjacques. "Optimal weighting in galaxy surveys: Application to redshift-space distortions". In: *Phys. Rev. D* 86.10, 103513 (Nov. 2012), p. 103513. arXiv:1207.1102 [astro-ph.CO].

[66]   F. C. van den Bosch et al. "Cosmological constraints from a combination of galaxy clustering and lensing - I. Theoretical framework". In: *Mon. Not. R. Astron. Soc.* 430 (Apr. 2013), pp. 725–746. arXiv:1206.6890 [astro-ph.CO].

[67] J. L. Tinker et al. "Cosmological Constraints from Galaxy Clustering and the Mass-to-number Ratio of Galaxy Clusters". In: *Astrophys. J.* 745, 16 (Jan. 2012), p. 16. arXiv:`1104.1635 [astro-ph.CO]`.

[68] J. Yoo and U. Seljak. "Joint analysis of gravitational lensing, clustering, and abundance: Toward the unification of large-scale structure analysis". In: *Phys. Rev. D* 86.8, 083504 (Oct. 2012), p. 083504. arXiv:`1207.2471 [astro-ph.CO]`.

[69] R. Mandelbaum et al. "Cosmological parameter constraints from galaxy-galaxy lensing and galaxy clustering with the SDSS DR7". In: *Mon. Not. R. Astron. Soc.* 432 (June 2013), pp. 1544–1575. arXiv:`1207.1120 [astro-ph.CO]`.

[70] B. Jain et al. "Novel Probes of Gravity and Dark Energy". In: *ArXiv e-prints* (Sept. 2013). arXiv:`1309.5389 [astro-ph.CO]`.

[71] B. Jain, V. Vikram, and J. Sakstein. "Astrophysical Tests of Modified Gravity: Constraints from Distance Indicators in the Nearby Universe". In: *Astrophys. J.* 779, 39 (Dec. 2013), p. 39. arXiv:`1204.6044 [astro-ph.CO]`.

[72] B. A. Reid and M. White. "Towards an accurate model of the redshift-space clustering of haloes in the quasi-linear regime". In: *Mon. Not. R. Astron. Soc.* 417 (Nov. 2011), pp. 1913–1927. arXiv:`1105.4165 [astro-ph.CO]`.

[73] J. Carlson, B. Reid, and M. White. "Convolution Lagrangian perturbation theory for biased tracers". In: *Mon. Not. R. Astron. Soc.* 429 (Feb. 2013), pp. 1674–1685. arXiv:`1209.0780 [astro-ph.CO]`.

[74] Y.-S. Song et al. "Chasing unbiased spectra of the Universe". In: *Phys. Rev. D* 87.12, 123510 (June 2013), p. 123510. arXiv:`1301.3133 [astro-ph.CO]`.

[75] B. A. Reid and M. White. "Towards an accurate model of the redshift-space clustering of haloes in the quasi-linear regime". In: *Mon. Not. R. Astron. Soc.* 417 (Nov. 2011), pp. 1913–1927. arXiv:`1105.4165 [astro-ph.CO]`.

[76] Z. Vlah et al. "Distribution function approach to redshift space distortions. Part V: perturbation theory applied to dark matter halos". In: *ArXiv e-prints* (Aug. 2013). arXiv:`1308.6294 [astro-ph.CO]`.

[77] L. Samushia, W. J. Percival, and A. Raccanelli. "Interpreting large-scale redshift-space distortion measurements". In: *Mon. Not. R. Astron. Soc.* 420 (Mar. 2012), pp. 2102–2119. arXiv:`1102.1014 [astro-ph.CO]`.

[78] T. Okumura et al. "Large-Scale Anisotropic Correlation Function of SDSS Luminous Red Galaxies". In: *Astrophys. J.* 676 (Apr. 2008), pp. 889–898. arXiv:`0711.3640`.

[79] Y.-S. Song et al. "Measuring coherent motions in the universe". In: *J. Cosmology Astropart.-Phys.* 5, 020 (May 2011), p. 20. arXiv:`1006.4630 [astro-ph.CO]`.

[80] F. Beutler et al. "The 6dF Galaxy Survey: $z = 0$ measurements of the growth rate and σ_8". In: *Mon. Not. R. Astron. Soc.* 423 (July 2012), pp. 3430–3444. arXiv:`1204.4725 [astro-ph.CO]`.

[81] Y.-S. Song et al. "Cosmological Tests using Redshift Space Clustering in BOSS DR11". In: *ArXiv e-prints* (July 2014). arXiv:`1407.2257`.

[82] C. Blake et al. "The WiggleZ Dark Energy Survey: the growth rate of cosmic structure since redshift z=0.9". In: *Mon. Not. R. Astron. Soc.* 415 (Aug. 2011), pp. 2876–2891. arXiv:`1104.2948 [astro-ph.CO]`.

[83] B. A. Reid et al. "The clustering of galaxies in the SDSS-III Baryon Oscillation Spectroscopic Survey: measurements of the growth of structure and expansion rate at z = 0.57 from anisotropic clustering". In: *Mon. Not. R. Astron. Soc.* 426 (Nov. 2012), pp. 2719–2737. arXiv:1203.6641 [astro-ph.CO].

[84] F. Beutler et al. "The clustering of galaxies in the SDSS-III Baryon Oscillation Spectroscopic Survey: Testing gravity with redshift-space distortions using the power spectrum multipoles". In: *ArXiv:132.4611 (submitted)* (Dec. 2013). arXiv:1312.4611.

[85] L. Samushia et al. "The clustering of galaxies in the SDSS-III Baryon Oscillation Spectroscopic Survey: measuring growth rate and geometry with anisotropic clustering". In: *Mon. Not. R. Astron. Soc.* 439 (Apr. 2014), pp. 3504–3519. arXiv:1312.4899.

[86] E. A. Kazin et al. "The clustering of galaxies in the SDSS-III Baryon Oscillation Spectroscopic Survey: measuring H(z) and D_A(z) at z = 0.57 with clustering wedges". In: *Mon. Not. R. Astron. Soc.* (Aug. 2013). arXiv:1303.4391 [astro-ph.CO].

[87] A. G. Sánchez et al. "The clustering of galaxies in the SDSS-III Baryon Oscillation Spectroscopic Survey: cosmological implications of the full shape of the clustering wedges in the data release 10 and 11 galaxy samples". In: *Mon. Not. R. Astron. Soc.* 440 (May 2014), pp. 2692–2713. arXiv:1312.4854 [astro-ph.CO].

[88] W. J. Percival et al. "The clustering of Galaxies in the SDSS-III Baryon Oscillation Spectroscopic Survey: including covariance matrix errors". In: *Mon. Not. R. Astron. Soc.* 439 (Apr. 2014), pp. 2531–2541. arXiv:1312.4841 [astro-ph.CO].

[89] L. Samushia et al. "The clustering of galaxies in the SDSS-III DR9 Baryon Oscillation Spectroscopic Survey: testing deviations from Λ and general relativity using anisotropic clustering of galaxies". In: *Mon. Not. R. Astron. Soc.* 429 (Feb. 2013), pp. 1514–1528. arXiv:1206.5309 [astro-ph.CO].

[90] W. J. Percival et al. "The 2dF Galaxy Redshift Survey: spherical harmonics analysis of fluctuations in the final catalogue". In: *Mon. Not. R. Astron. Soc.* 353 (Oct. 2004), pp. 1201–1218. eprint: arXiv:astro-ph/0406513.

[91] L. Guzzo et al. "A test of the nature of cosmic acceleration using galaxy redshift distortions". In: *Nature* 451 (Jan. 2008), pp. 541–544. arXiv:0802.1944.

[92] S. de la Torre et al. "The VIMOS Public Extragalactic Redshift Survey (VIPERS) . Galaxy clustering and redshift-space distortions at z ∼ 0.8 in the first data release". In: *Astron. Astrophys.* 557, A54 (Sept. 2013), A54. arXiv:1303.2622.

[93] T. Okumura et al. "The Subaru FMOS galaxy redshift survey (FastSound). IV. New constraint on gravity theory from redshift space distortions at $z \sim 1.4$". In: *ArXiv e-prints* (Nov. 2015). arXiv:1511.08083.

[94] E. Komatsu et al. "Seven-year Wilkinson Microwave Anisotropy Probe (WMAP) Observations: Cosmological Interpretation". In: *Astrophys. J. Supp.* 192, 18 (Feb. 2011), p. 18. arXiv:1001.4538 [astro-ph.CO].

[95] A. Font-Ribera et al. "DESI and other Dark Energy experiments in the era of neutrino mass measurements". In: *J. Cosmology Astropart. Phys.* 5, 023 (May 2014), p. 23. arXiv:1308.4164.

[96] M. J. Drinkwater et al. "The WiggleZ Dark Energy Survey: survey design and first data release". In: *Mon. Not. R. Astron. Soc.* 401 (Jan. 2010), pp. 1429–1452. arXiv:0911.4246 [astro-ph.CO].

[97]   C. Alcock and B. Paczynski. "An evolution free test for non-zero cosmological constant". In: *Nature* 281 (Oct. 1979), pp. 358–+.

[98]   P. McDonald. "Toward a Measurement of the Cosmological Geometry at z ∼ 2: Predicting Lyα Forest Correlation in Three Dimensions and the Potential of Future Data Sets". In: *Astrophys. J.* 585 (Mar. 2003), pp. 34–51. eprint: `arXiv:astro-ph/0108064`.

[99]   H.-J. Seo and D. J. Eisenstein. "Improved Forecasts for the Baryon Acoustic Oscillations and Cosmological Distance Scale". In: *Astrophys. J.* 665 (Aug. 2007), pp. 14–24. eprint: `arXiv:astro-ph/0701079`.

[100] H. A. Feldman, N. Kaiser, and J. A. Peacock. "Power-spectrum analysis of three-dimensional redshift surveys". In: *Astrophys. J.* 426 (May 1994), pp. 23–37.

[101] N. Mostek et al. "The DEEP2 Galaxy Redshift Survey: Clustering Dependence on Galaxy Stellar Mass and Star Formation Rate at z ∼ 1". In: *Astrophys. J.* 767, 89 (Apr. 2013), p. 89. arXiv:1210.6694 [astro-ph.CO].

[102] N. P. Ross et al. "Clustering of Low-redshift (z <= 2.2) Quasars from the Sloan Digital Sky Survey". In: *Astrophys. J.* 697 (June 2009), pp. 1634–1655. arXiv:0903.3230 [astro-ph.CO].

[103] N. Mostek et al. "Mapping the universe with BigBOSS". In: *Society of Photo-Optical Instrumentation Engineers (SPIE) Conference Series*. Vol. 8446. Society of Photo-Optical Instrumentation Engineers (SPIE) Conference Series. Sept. 2012.

[104] R. Laureijs et al. "Euclid Definition Study Report". In: *ArXiv e-prints* (Oct. 2011). arXiv:1110.3193 [astro-ph.CO].

[105] D. Spergel et al. "Wide-Field InfraRed Survey Telescope-Astrophysics Focused Telescope Assets WFIRST-AFTA Final Report". In: *ArXiv e-prints* (May 2013). arXiv:1305.5422 [astro-ph.IM].

[106] A. G. Riess et al. "A 3% Solution: Determination of the Hubble Constant with the Hubble Space Telescope and Wide Field Camera 3". In: *Astrophys. J.* 730, 119 (Apr. 2011), p. 119. arXiv:1103.2976 [astro-ph.CO].

[107] X. Xu et al. "Measuring D_A and H at z=0.35 from the SDSS DR7 LRGs using baryon acoustic oscillations". In: *Mon. Not. R. Astron. Soc.* 431 (May 2013), pp. 2834–2860. arXiv:1206.6732 [astro-ph.CO].

[108] A. Font-Ribera et al. "Quasar-Lyman α forest cross-correlation from BOSS DR11: Baryon Acoustic Oscillations". In: *J. Cosmology Astropart. Phys.* 5, 027 (May 2014), p. 27. arXiv:1311.1767.

[109] M. Sullivan et al. "SNLS3: Constraints on Dark Energy Combining the Supernova Legacy Survey Three-year Data with Other Probes". In: *Astrophys. J.* 737, 102 (Aug. 2011), p. 102. arXiv:1104.1444 [astro-ph.CO].

[110] M. White. "Shot noise and reconstruction of the acoustic peak". In: *ArXiv e-prints* (Apr. 2010). arXiv:1004.0250 [astro-ph.CO].

[111] P. McDonald et al. "The Lyα Forest Power Spectrum from the Sloan Digital Sky Survey". In: *Astrophys. J. Supp.* 163 (Mar. 2006), pp. 80–109. eprint: `arXiv:astro-ph/0405013`.

[112] P. McDonald et al. "The Linear Theory Power Spectrum from the Lyα Forest in the Sloan Digital Sky Survey". In: *Astrophys. J.* 635 (Dec. 2005), pp. 761–783.

[113] P. McDonald et al. "Physical effects on the Lyα forest flux power spectrum: damping wings, ionizing radiation fluctuations and galactic winds". In: *Mon. Not. R. Astron. Soc.* 360 (July 2005), pp. 1471–1482.

[114] R. Mandelbaum et al. "Precision cosmology from the Lyman-α forest: power spectrum and bispectrum". In: *Mon. Not. R. Astron. Soc.* 344 (Sept. 2003), pp. 776–788.

[115] P. McDonald et al. "A Measurement of the Temperature-Density Relation in the Intergalactic Medium Using a New Lyα Absorption-Line Fitting Method". In: *Astrophys. J.* 562 (Nov. 2001), pp. 52–75.

[116] P. McDonald et al. "The Observed Probability Distribution Function, Power Spectrum, and Correlation Function of the Transmitted Flux in the Lyα Forest". In: *Astrophys. J.* 543 (Nov. 2000), pp. 1–23.

[117] T.-S. Kim et al. "The power spectrum of the flux distribution in the Lyman α forest of a large sample of UVES QSO absorption spectra (LUQAS)". In: *Mon. Not. R. Astron. Soc.* 347 (Jan. 2004), pp. 355–366. eprint: `arXiv:astro-ph/0308103`.

[118] V. Iršič et al. "Detection of Ly-β auto-correlations and Ly-α–Ly-β cross-correlations in BOSS Data Release 9". In: *ArXiv e-prints* (July 2013). arXiv:`1307.3403` [`astro-ph.CO`].

[119] A. Font-Ribera et al. "The large-scale quasar-Lyman α forest cross-correlation from BOSS". In: *J. Cosmology Astropart. Phys.* 5, 018 (May 2013), p. 18. arXiv:`1303.1937` [`astro-ph.CO`].

[120] N. Palanque-Delabrouille et al. "The one-dimensional Ly-alpha forest power spectrum from BOSS". In: *ArXiv e-prints* (June 2013). arXiv:`1306.5896` [`astro-ph.CO`].

[121] U. Seljak, A. Slosar, and P. McDonald. "Cosmological parameters from combining the Lyman-α forest with CMB, galaxy clustering and SN constraints". In: *Journal of Cosmology and Astro-Particle Physics* 10 (Oct. 2006), pp. 14–+.

[122] U. Seljak et al. "Cosmological parameter analysis including SDSS Lyα forest and galaxy bias: Constraints on the primordial spectrum of fluctuations, neutrino mass, and dark energy". In: *Phys. Rev. D* 71.10 (May 2005), pp. 103515–+.

[123] A. Kosowsky and M. S. Turner. "CBR anisotropy and the running of the scalar spectral index". In: *Phys. Rev. D* 52 (Aug. 1995), p. 1739. eprint: `arXiv:astro-ph/9504071`.

[124] S. Dodelson. *Modern cosmology.*, 2003.

[125] P.A.R. Ade et al. "Planck 2015 results. XX. Constraints on inflation". In: *ArXiv e-prints* (2015). arXiv:`1502.02114` [`astro-ph.CO`].

[126] A. R. Liddle and D. H. Lyth. *Cosmological Inflation and Large-Scale Structure.*, June 2000.

[127] R. Easther and H. V. Peiris. "Implications of a running spectral index for slow roll inflation". In: *J. Cosmology Astropart. Phys.* 9, 010 (Sept. 2006), p. 10. eprint: `arXiv:astro-ph/0604214`.

[128] D. J. Chung, G. Shiu, and M. Trodden. "Running of the scalar spectral index from inflationary models". In: *Phys. Rev. D* 68.6, 063501 (Sept. 2003), p. 063501. eprint: `arXiv:astro-ph/0305193`.

[129] P.A.R. Ade et al. "Planck 2015 results. XVII. Constraints on primordial non-Gaussianity". In: *ArXiv e-prints* (2015). arXiv:`1502.01592` [`astro-ph.CO`].

[130] Xingang Chen et al. "Observational signatures and non-Gaussianities of general single field inflation". In: *JCAP* 0701 (2007), p. 002. arXiv:`hep-th/0605045` [`hep-th`].

[131]   Justin Khoury and Federico Piazza. "Rapidly-Varying Speed of Sound, Scale Invariance and Non-Gaussian Signatures". In: *JCAP* 0907 (2009), p. 026. arXiv:`0811.3633 [hep-th]`.

[132]   Johannes Noller and Joao Magueijo. "Non-Gaussianity in single field models without slow-roll". In: *Phys.Rev.* D83 (2011), p. 103511. arXiv:`1102.0275 [astro-ph.CO]`.

[133]   Raquel H. Ribeiro. "Inflationary signatures of single-field models beyond slow-roll". In: *JCAP* 1205 (2012), p. 037. arXiv:`1202.4453 [astro-ph.CO]`.

[134]   Johannes Noller. "Constraining fast-roll inflation". In: *ArXiv e-prints* (2012). arXiv:`1205.5796 [astro-ph.CO]`.

[135]   Xingang Chen and Yi Wang. "Large non-Gaussianities with Intermediate Shapes from Quasi-Single Field Inflation". In: *Phys.Rev.* D81 (2010), p. 063511. arXiv:`0909.0496 [astro-ph.CO]`.

[136]   Xingang Chen and Yi Wang. "Quasi-Single Field Inflation and Non-Gaussianities". In: *JCAP* 1004 (2010), p. 027. arXiv:`0911.3380 [hep-th]`.

[137]   Sujata Gupta et al. "Non-Gaussian signatures in the cosmic background radiation from warm inflation". In: *Phys.Rev.* D66 (2002), p. 043510. arXiv:`astro-ph/0205152 [astro-ph]`.

[138]   Ian G Moss and Chun Xiong. "Non-Gaussianity in fluctuations from warm inflation". In: *JCAP* 0704 (2007), p. 007. arXiv:`astro-ph/0701302 [astro-ph]`.

[139]   R. Holman and Andrew J. Tolley. "Enhanced Non-Gaussianity from Excited Initial States". In: *JCAP* 0805 (2008), p. 001. arXiv:`0710.1302 [hep-th]`.

[140]   Pieter Daniel Meerburg, Jan Pieter van der Schaar, and Pier Stefano Corasaniti. "Signatures of Initial State Modifications on Bispectrum Statistics". In: *JCAP* 0905 (2009), p. 018. arXiv:`0901.4044 [hep-th]`.

[141]   Nishant Agarwal et al. "Effective field theory and non-Gaussianity from general inflationary states". In: *ArXiv e-prints* (2012). arXiv:`1212.1172 [hep-th]`.

[142]   David Langlois et al. "Primordial perturbations and non-Gaussianities in DBI and general multi-field inflation". In: *Phys.Rev.* D78 (2008), p. 063523. arXiv:`0806.0336 [hep-th]`.

[143]   Frederico Arroja, Shuntaro Mizuno, and Kazuya Koyama. "Non-gaussianity from the bispectrum in general multiple field inflation". In: *JCAP* 0808 (2008), p. 015. arXiv:`0806.0619 [astro-ph]`.

[144]   Sebastien Renaux-Petel. "Combined local and equilateral non-Gaussianities from multifield DBI inflation". In: *JCAP* 0910 (2009), p. 012. arXiv:`0907.2476 [hep-th]`.

[145]   David Langlois and Angela Lepidi. "General treatment of isocurvature perturbations and non-Gaussianities". In: *JCAP* 1101 (2011), p. 008. arXiv:`1007.5498 [astro-ph.CO]`.

[146]   David Langlois and Bartjan van Tent. "Hunting for Isocurvature Modes in the CMB non-Gaussianities". In: *Class.Quant.Grav.* 28 (2011), p. 222001. arXiv:`1104.2567 [astro-ph.CO]`.

[147]   David Langlois and Bartjan van Tent. "Isocurvature modes in the CMB bispectrum". In: *JCAP* 1207 (2012), p. 040. arXiv:`1204.5042 [astro-ph.CO]`.

[148]   E. Komatsu. "The Pursuit of Non-Gaussian Fluctuations in the Cosmic Microwave Background". In: *ArXiv Astrophysics e-prints* (June 2002). eprint: `arXiv:astro-ph/0206039`.

[149]   C. L. Bennett et al. "Nine-Year Wilkinson Microwave Anisotropy Probe (WMAP) Observations: Final Maps and Results". In: *ArXiv e-prints* (Dec. 2012). arXiv:`1212.5225 [astro-ph.CO]`.

[150] Planck Collaboration et al. "Planck 2013 Results. XXIV. Constraints on primordial non-Gaussianity". In: *ArXiv e-prints* (Mar. 2013). arXiv:1303.5084 [`astro-ph.CO`].

[151] N. Dalal et al. "Imprints of primordial non-Gaussianities on large-scale structure: Scale-dependent bias and abundance of virialized objects". In: *Phys. Rev. D* 77.12 (June 2008), pp. 123514–+. arXiv:0710.4560.

[152] A. Slosar et al. "Constraints on local primordial non-Gaussianity from large scale structure". In: *Journal of Cosmology and Astro-Particle Physics* 8 (Aug. 2008), pp. 31–+. arXiv:0805.3580.

[153] S. Ho et al. "Sloan Digital Sky Survey III Photometric Quasar Clustering: Probing the Initial Conditions of the Universe using the Largest Volume". In: *ArXiv e-prints* (Nov. 2013). arXiv:1311.2597 [`astro-ph.CO`].

[154] T. Giannantonio et al. "Improved primordial non-Gaussianity constraints from measurements of galaxy clustering and the integrated Sachs-Wolfe effect". In: *Phys. Rev. D* 89.2, 023511 (Jan. 2014), p. 023511. arXiv:1303.1349 [`astro-ph.CO`].

[155] N. Agarwal et al. "Characterizing unknown systematics in large scale structure surveys". In: *ArXiv e-prints* (Sept. 2013). arXiv:1309.2954 [`astro-ph.CO`].

[156] C. Pitrou, J.-P. Uzan, and F. Bernardeau. "The cosmic microwave background bispectrum from the non-linear evolution of the cosmological perturbations". In: *J. Cosmology Astropart. Phys.* 7, 003 (July 2010), p. 3. arXiv:1003.0481 [`astro-ph.CO`].

[157] N. Bartolo, S. Matarrese, and A. Riotto. "Non-Gaussianity and the Cosmic Microwave Background Anisotropies". In: *Advances in Astronomy* 2010 (2010). arXiv:1001.3957 [`astro-ph.CO`].

[158] A. Becker and D. Huterer. "First Constraints on the Running of Non-Gaussianity". In: *Physical Review Letters* 109.12, 121302 (Sept. 2012), p. 121302. arXiv:1207.5788 [`astro-ph.CO`].

[159] A. Becker, D. Huterer, and K. Kadota. "Constraining scale-dependent non-Gaussianity with future large-scale structure and the CMB". In: *J. Cosmology Astropart. Phys.* 12, 034 (Dec. 2012), p. 34. arXiv:1206.6165 [`astro-ph.CO`].

[160] U. Seljak. "Extracting Primordial Non-Gaussianity without Cosmic Variance". In: *Physical Review Letters* 102.2, 021302 (Jan. 2009), p. 021302. arXiv:0807.1770.

[161] P. McDonald and U. Seljak. "How to evade the sample variance limit on measurements of redshift-space distortions". In: *J. Cosmology Astropart. Phys.* 10, 007 (Oct. 2009), p. 7. arXiv:0810.0323.

[162] V. Desjacques, U. Seljak, and I. T. Iliev. "Scale-dependent bias induced by local non-Gaussianity: a comparison to N-body simulations". In: *Mon. Not. R. Astron. Soc.* 396 (June 2009), pp. 85–96. arXiv:0811.2748.

[163] D. Huterer, C. E. Cunha, and W. Fang. "Calibration errors unleashed: effects on cosmological parameters and requirements for large-scale structure surveys". In: *Mon. Not. R. Astron.-Soc.* 432 (July 2013), pp. 2945–2961. arXiv:1211.1015 [`astro-ph.CO`].

[164] B. Leistedt et al. "Estimating the large-scale angular power spectrum in the presence of systematics: a case study of Sloan Digital Sky Survey quasars". In: *Mon. Not. R. Astron.-Soc.* (Sept. 2013). arXiv:1306.0005 [`astro-ph.CO`].

[165] J. Lesgourgues et al. *Neutrino Cosmology.*, Feb. 2013.

[166] Gianpiero Mangano et al. "Relic neutrino decoupling including flavor oscillations". In: *Nucl.-Phys.* B729 (2005), pp. 221–234. arXiv:hep-ph/0506164 [`hep-ph`].

[167] J. Hamann et al. "Cosmology seeking friendship with sterile neutrinos". In: *Nuclear Physics B Proceedings Supplements* 217 (Aug. 2011), pp. 72–74.

[168] W. Fischler and J. Meyers. "Dark radiation emerging after big bang nucleosynthesis?" In: *Phys. Rev. D* 83.6, 063520 (Mar. 2011), p. 063520. arXiv:1011.3501 [astro-ph.CO].

[169] S. Bashinsky and U. Seljak. "Signatures of relativistic neutrinos in CMB anisotropy and matter clustering". In: *Phys. Rev. D* 69.8, 083002 (Apr. 2004), p. 083002. eprint: arXiv: astro-ph/0310198.

[170] E. Calabrese et al. "Limits on dark radiation, early dark energy, and relativistic degrees of freedom". In: *Phys. Rev. D* 83.12, 123504 (June 2011), p. 123504. arXiv:1103.4132 [astro-ph.CO].

[171] S. Ho et al. "Correlation of CMB with large-scale structure. I. Integrated Sachs-Wolfe tomography and cosmological implications". In: *Phys. Rev. D* 78.4, 043519 (Aug. 2008), p. 043519. arXiv:0801.0642.

[172] P. Zhang et al. "Probing Gravity at Cosmological Scales by Measurements which Test the Relationship between Gravitational Lensing and Matter Overdensity". In: *Physical Review Letters* 99.14 (Oct. 2007), pp. 141302–+. arXiv:0704.1932.

[173] J.R. Fergusson, M. Liguori, and E.P.S. Shellard. "General CMB and Primordial Bispectrum Estimation I: Mode Expansion, Map-Making and Measures of f_{NL}". In: *Phys.Rev.* D82 (2010), p. 023502. arXiv:0912.5516 [astro-ph.CO].

[174] M. Liguori et al. "Primordial non-Gaussianity and Bispectrum Measurements in the Cosmic Microwave Background and Large-Scale Structure". In: *Adv.Astron.* 2010 (2010), p. 980523. arXiv:1001.4707 [astro-ph.CO].

[175] P. Zhang. "The dark flow induced small-scale kinetic Sunyaev-Zel'dovich effect". In: *Mon. Not. R. Astron. Soc.* 407 (Sept. 2010), pp. L36–L40. arXiv:1004.0990 [astro-ph.CO].

[176] P. Zhang and A. Stebbins. "Confirmation of the Copernican Principle at Gpc Radial Scale and above from the Kinetic Sunyaev-Zel'dovich Effect Power Spectrum". In: *Physical Review Letters* 107.4, 041301 (July 2011), p. 041301. arXiv:1009.3967 [astro-ph.CO].

[177] Z. Li, P. Zhang, and X. Chen. "Anomalous Anisotropic Cross-correlations between WMAP CMB Maps and SDSS Galaxy Distribution and Implications on the Dark Flow Scenario". In: *Astrophys. J.* 758, 130 (Oct. 2012), p. 130. arXiv:1209.0520 [astro-ph.CO].

[178] S. Ho, S. Dedeo, and D. Spergel. "Finding the Missing Baryons Using CMB as a Backlight". In: *ArXiv e-prints* (Mar. 2009). arXiv:0903.2845 [astro-ph.CO].

[179] J. A. Newman. "Calibrating Redshift Distributions beyond Spectroscopic Limits with Cross-Correlations". In: *Astrophys. J.* 684 (Sept. 2008), pp. 88–101. arXiv:0805.1409.

[180] M. McQuinn and M. White. "On using angular cross-correlations to determine source redshift distributions". In: *Mon. Not. R. Astron. Soc.* 433 (Aug. 2013), pp. 2857–2883. arXiv:1302.0857 [astro-ph.CO].

[181] S. J. Schmidt et al. "Recovering redshift distributions with cross-correlations: pushing the boundaries". In: *Mon. Not. R. Astron. Soc.* 431 (June 2013), pp. 3307–3318. arXiv:1303.0292 [astro-ph.CO].

[182] J. Coupon, T. Broadhurst, and K. Umetsu. "Cluster Lensing Profiles Derived from a Redshift Enhancement of Magnified BOSS-survey Galaxies". In: *Astrophys. J.* 772, 65 (July 2013), p. 65. arXiv:1303.6588 [astro-ph.CO].

[183] M. Cacciato et al. "Cosmological constraints from a combination of galaxy clustering and lensing - III. Application to SDSS data". In: *Mon. Not. R. Astron. Soc.* 430 (Apr. 2013), pp. 767–786. arXiv:1207.0503 [astro-ph.CO].

[184] Y.-C. Cai and G. Bernstein. "Combining weak-lensing tomography and spectroscopic redshift surveys". In: *Mon. Not. R. Astron. Soc.* 422 (May 2012), pp. 1045–1056. arXiv:1112.4478 [astro-ph.CO].

[185] E. Gaztañaga et al. "Cross-correlation of spectroscopic and photometric galaxy surveys: cosmology from lensing and redshift distortions". In: *Mon. Not. R. Astron. Soc.* 422 (June 2012), pp. 2904–2930. arXiv:1109.4852 [astro-ph.CO].

[186] D. Kirk et al. "Optimising Spectroscopic and Photometric Galaxy Surveys: Same-sky Benefits for Dark Energy and Modified Gravity". In: *ArXiv e-prints* (July 2013). arXiv:1307.8062 [astro-ph.CO].

[187] R. de Putter, O. Doré, and M. Takada. "The Synergy between Weak Lensing and Galaxy Redshift Surveys". In: *ArXiv e-prints* (Aug. 2013). arXiv:1308.6070 [astro-ph.CO].

[188] T. Y. Lam et al. "Testing Gravity with the Stacked Phase Space around Galaxy Clusters". In: *Physical Review Letters* 109.5, 051301 (Aug. 2012), p. 051301. arXiv:1202.4501 [astro-ph.CO].

[189] R. de Putter, O. Doré, and M. Takada. "The Synergy between Weak Lensing and Galaxy Redshift Surveys". In: *ArXiv e-prints* (Aug. 2013). arXiv:1308.6070 [astro-ph.CO].

[190] M. Betoule et al. "Improved cosmological constraints from a joint analysis of the SDSS-II and SNLS supernova samples". In: *Astron. Astrophys.* 568, A22 (Aug. 2014), A22. arXiv:1401.4064.

[191] C. Conroy, R. H. Wechsler, and A. V. Kravtsov. "Modeling Luminosity-dependent Galaxy Clustering through Cosmic Time". In: *Astrophys. J.* 647 (Aug. 2006), pp. 201–214. eprint: arXiv:astro-ph/0512234.

[192] D. J. Eisenstein et al. "Spectroscopic Target Selection for the Sloan Digital Sky Survey: The Luminous Red Galaxy Sample". In: *Astron. J.* 122 (Nov. 2001), pp. 2267–2280. eprint: arXiv:astro-ph/0108153.

[193] D. J. Eisenstein et al. "Detection of the Baryon Acoustic Peak in the Large-Scale Correlation Function of SDSS Luminous Red Galaxies". In: *Astrophys. J.* 633 (Nov. 2005), pp. 560–574. eprint: arXiv:astro-ph/0501171.

[194] S. Ho et al. "Luminous Red Galaxy Population in Clusters at $0.2 \le z \le 0.6$". In: *Astrophys. J.* 697 (June 2009), pp. 1358–1368. arXiv:0706.0727.

[195] E. A. Kazin et al. "The Baryonic Acoustic Feature and Large-Scale Clustering in the Sloan Digital Sky Survey Luminous Red Galaxy Sample". In: *Astrophys. J.* 710 (Feb. 2010), pp. 1444–1461. arXiv:0908.2598 [astro-ph.CO].

[196] N. Padmanabhan et al. "The clustering of luminous red galaxies in the Sloan Digital Sky Survey imaging data". In: *Mon. Not. R. Astron. Soc.* 378 (July 2007), pp. 852–872. eprint: arXiv:astro-ph/0605302.

[197] T. L. John. "Continuous absorption by the negative hydrogen ion reconsidered". In: *Astron.-Astrophys.* 193 (Mar. 1988), pp. 189–192.

[198] M. Sawicki. "The 1.6 Micron Bump as a Photometric Redshift Indicator". In: *Astron. J.* 124 (Dec. 2002), pp. 3050–3060. eprint: arXiv:astro-ph/0209437.

[199] M. J. I. Brown et al. "An Atlas of Galaxy Spectral Energy Distributions from the Ultraviolet to the Mid-infrared". In: *Astrophys. J. Supp.* 212, 18 (June 2014), p. 18. arXiv:`1312.3029` [`astro-ph.CO`].

[200] S. D. J. Gwyn. "MegaPipe: The MegaCam Image Stacking Pipeline at the Canadian Astronomical Data Centre". In: *Proc. Astron. Soc. Pacific* 120 (Feb. 2008), pp. 212–223. arXiv:`0710.0370`.

[201] J. A. Newman et al. "The DEEP2 Galaxy Redshift Survey: Design, Observations, Data Reduction, and Redshifts". In: *Astrophys. J. Supp.* 208, 5 (Sept. 2013), p. 5. arXiv:`1203.3192` [`astro-ph.CO`].

[202] O. Ilbert et al. "Cosmos Photometric Redshifts with 30-Bands for 2-deg^2". In: *Astrophys. J.* 690 (Jan. 2009), pp. 1236–1249. arXiv:`0809.2101`.

[203] M. White et al. "The Clustering of Massive Galaxies at z $\sim$ 0.5 from the First Semester of BOSS Data". In: *Astrophys. J.* 728, 126 (Feb. 2011), p. 126. arXiv:`1010.4915` [`astro-ph.CO`].

[204] A. M. Hopkins and J. F. Beacom. "On the Normalization of the Cosmic Star Formation History". In: *Astrophys. J.* 651 (Nov. 2006), pp. 142–154. eprint: `arXiv:astro-ph/0601463`.

[205] G. Zhu, J. Moustakas, and M. R. Blanton. "The [O II] $\lambda3727$ Luminosity Function at z $\sim$ 1". In: *Astrophys. J.* 701 (Aug. 2009), pp. 86–93. arXiv:`0811.3035`.

[206] W. Rujopakarn et al. "The Evolution of the Star Formation Rate of Galaxies at 0.0 <= z <= 1.2". In: *Astrophys. J.* 718 (Aug. 2010), pp. 1171–1185. eprint: `1006.4359` (astro-ph.CO).

[207] J. Comparat et al. "Measuring galaxy [OII] emission line doublet with future ground-based wide-field spectroscopic surveys". In: *ArXiv e-prints* (Oct. 2013). arXiv:`1310.0615` [`astro-ph.IM`].

[208] D. J. Matthews et al. "Extended Photometry for the DEEP2 Galaxy Redshift Survey: A Testbed for Photometric Redshift Experiments". In: *Astrophys. J. Supp.* 204, 21 (Feb. 2013), p. 21. arXiv:`1210.2405` [`astro-ph.CO`].

[209] M. Davis et al. "Science Objectives and Early Results of the DEEP2 Redshift Survey". In: *Society of Photo-Optical Instrumentation Engineers (SPIE) Conference Series*. Ed. by P. Guhathakurta. Vol. 4834. Society of Photo-Optical Instrumentation Engineers (SPIE) Conference Series. Feb. 2003, pp. 161–172. eprint: `arXiv:astro-ph/0209419`.

[210] J. Comparat et al. "The 0.1 <z < 1.65 evolution of the bright end of the [O ii] luminosity function". In: *Astron. Astrophys.* 575, A40 (Mar. 2015), A40. arXiv:`1408.1523`.

[211] A. Raichoor et al. "The SDSS-IV extended Baryonic Oscillation Spectroscopic Survey: selecting Emission Line Galaxies using the Fisher Discriminant". In: *ArXiv e-prints* (May 2015). arXiv:`1505.01797`.

[212] J. Comparat et al. "Investigating emission-line galaxy surveys with the Sloan Digital Sky Survey infrastructure". In: *Mon. Not. R. Astron. Soc.* 428 (Jan. 2013), pp. 1498–1517. arXiv:`1207.4321` [`astro-ph.CO`].

[213] R. C. Kennicutt Jr. "Star Formation in Galaxies Along the Hubble Sequence". In: *Annu. Rev. Astron. Astrophys.* 36 (1998), pp. 189–232. eprint: `arXiv:astro-ph/9807187`.

[214] R. C. Kennicutt and N. J. Evans. "Star Formation in the Milky Way and Nearby Galaxies". In: *Annu. Rev. Astron. Astrophys.* 50 (Sept. 2012), pp. 531–608. arXiv:`1204.3552` [`astro-ph.GA`].

[215] O. Ilbert et al. "Mass assembly in quiescent and star-forming galaxies since $z \simeq 4$ from Ultra-VISTA". In: *Astron. Astrophys.* 556, A55 (Aug. 2013), A55. arXiv:1301.3157 [astro-ph.CO].

[216] O. Le Fèvre et al. "The VIMOS VLT Deep Survey final data release: a spectroscopic sample of 35 016 galaxies and AGN out to $z \sim 6.7$ selected with $17.5 \leq i_{AB} \leq 24.75$". In: *Astron.-Astrophys.* 559, A14 (Nov. 2013), A14. arXiv:1307.0545 [astro-ph.CO].

[217] A. L. Coil et al. "The DEEP2 Galaxy Redshift Survey: Color and Luminosity Dependence of Galaxy Clustering at z $\sim$ 1". In: *Astrophys. J.* 672 (Jan. 2008), pp. 153–176. arXiv:0708.0004.

[218] N. Mostek et al. "The DEEP2 Galaxy Redshift Survey: Clustering Dependence on Galaxy Stellar Mass and Star Formation Rate at z $\sim$ 1". In: *Astrophys. J.* 767, 89 (Apr. 2013), p. 89. arXiv:1210.6694 [astro-ph.CO].

[219] R. E. Smith et al. "Stable clustering, the halo model and non-linear cosmological power spectra". In: *Mon. Not. R. Astron. Soc.* 341 (June 2003), pp. 1311–1332. eprint: arXiv:astro-ph/0207664.

[220] J. E. Geach et al. "HiZELS: a high-redshift survey of Hα emitters - I. The cosmic star formation rate and clustering at z = 2.23". In: *Mon. Not. R. Astron. Soc.* 388 (Aug. 2008), pp. 1473–1486. arXiv:0805.2861.

[221] C. Blake et al. "The WiggleZ Dark Energy Survey: small-scale clustering of Lyman-break galaxies at $z \leq 1$". In: *Mon. Not. R. Astron. Soc.* 395 (May 2009), pp. 240–254. arXiv:0901.2587 [astro-ph.CO].

[222] M. Sumiyoshi et al. "Photometric H alpha and [O II] Luminosity Function of SDF and SXDF Galaxies: Implications for Future Baryon Oscillation Surveys". In: *ArXiv e-prints* (Feb. 2009). arXiv:0902.2064.

[223] G. T. Richards et al. "Efficient Photometric Selection of Quasars from the Sloan Digital Sky Survey. II. $\sim$1,000,000 Quasars from Data Release 6". In: *Astrophys. J. Supp.* 180 (Jan. 2009), pp. 67–83. arXiv:0809.3952.

[224] N. Palanque-Delabrouille et al. "Luminosity function from dedicated SDSS-III and MMT data of quasars in $0.7 < z < 4.0$ selected with a new approach". In: *Astron. Astrophys.* 551, A29 (Mar. 2013), A29. arXiv:1209.3968 [astro-ph.CO].

[225] N. Palanque-Delabrouille et al. "The Extended Baryon Oscillation Spectroscopic Survey: Variability Selection and Quasar Luminosity Function". In: *ArXiv e-prints* (Sept. 2015). arXiv:1509.05607.

[226] L. Jiang et al. "A Spectroscopic Survey of Faint Quasars in the SDSS Deep Stripe. I. Preliminary Results from the Co-added Catalog". In: *Astron. J.* 131 (June 2006), pp. 2788–2800. eprint: arXiv:astro-ph/0602569.

[227] P. F. Hopkins, G. T. Richards, and L. Hernquist. "An Observational Determination of the Bolometric Quasar Luminosity Function". In: *Astrophys. J.* 654 (Jan. 2007), pp. 731–753. eprint: arXiv:astro-ph/0605678.

[228] LSST Science Collaboration et al. "LSST Science Book, Version 2.0". In: *ArXiv e-prints* (Dec. 2009). arXiv:0912.0201 [astro-ph.IM].

[229] D. Stern et al. "Mid-Infrared Selection of Active Galaxies". In: *Astrophys. J.* 631 (Sept. 2005), pp. 163–168. eprint: arXiv:astro-ph/0410523.

[230] C. Yèche et al. "Artificial neural networks for quasar selection and photometric redshift determination". In: *Astron. Astrophys.* 523, A14 (Nov. 2010), A14.

[231] J. Bovy et al. "Think Outside the Color Box: Probabilistic Target Selection and the SDSS-XDQSO Quasar Targeting Catalog". In: *Astrophys. J.* 729, 141 (Mar. 2011), p. 141. arXiv:1011.6392 [astro-ph.CO].

[232] N. P. Ross et al. "The SDSS-III Baryon Oscillation Spectroscopic Survey: Quasar Target Selection for Data Release Nine". In: *Astrophys. J. Supp.* 199, 3 (Mar. 2012), p. 3. arXiv:1105.0606 [astro-ph.CO].

[233] A. Font-Ribera et al. "The large-scale quasar-Lyman α forest cross-correlation from BOSS". In: *J. Cosmology Astropart. Phys.* 5, 018 (May 2013), p. 18. arXiv:1303.1937 [astro-ph.CO].

[234] N. P. Ross et al. "Clustering of Low-redshift ($z <= 2.2$) Quasars from the Sloan Digital Sky Survey". In: *Astrophys. J.* 697 (June 2009), pp. 1634–1655. arXiv:0903.3230 [astro-ph.CO].

[235] M. White et al. "The clustering of intermediate-redshift quasars as measured by the Baryon Oscillation Spectroscopic Survey". In: *Mon. Not. R. Astron. Soc.* 424 (Aug. 2012), pp. 933–950. arXiv:1203.5306 [astro-ph.CO].

[236] A. Slosar et al. "The Lyman-α forest in three dimensions: measurements of large scale flux correlations from BOSS 1st-year data". In: *J. Cosmology Astropart. Phys.* 9, 001 (Sept. 2011), p. 1. arXiv:1104.5244 [astro-ph.CO].

[237] N. Palanque-Delabrouille et al. "Variability selected high-redshift quasars on SDSS Stripe 82". In: *Astron. Astrophys.* 530, A122 (June 2011), A122. arXiv:1012.2391 [astro-ph.CO].

[238] K. B. Schmidt et al. "Selecting Quasars by Their Intrinsic Variability". In: *Astrophys. J.* 714 (May 2010), pp. 1194–1208. arXiv:1002.2642 [astro-ph.CO].

[239] G. G. Williams et al. "90prime: a prime focus imager for the Steward Observatory 90-in. telescope". In: *Ground-based Instrumentation for Astronomy.* Ed. by A. F. M. Moorwood and M. Iye. Vol. 5492. Society of Photo-Optical Instrumentation Engineers (SPIE) Conference Series. Sept. 2004, pp. 787–798.

[240] E. L. Wright et al. "The Wide-field Infrared Survey Explorer (WISE): Mission Description and Initial On-orbit Performance". In: *Astron. J.* 140, 1868 (Dec. 2010), pp. 1868–1881. arXiv:1008.0031 [astro-ph.IM].

[241] D. Lang. "unWISE: Unblurred Coadds of the WISE Imaging". In: *Astron. J.* 147, 108 (May 2014), p. 108. arXiv:1405.0308 [astro-ph.IM].

[242] K. N. Abazajian et al. "The Seventh Data Release of the Sloan Digital Sky Survey". In: *Astrophys. J. Supp.* 182, 543 (June 2009), pp. 543–558. arXiv:0812.0649.

[243] PanSTARRS. *PanSTARRS Survey Website.* http://pan-starrs.ifa.hawaii.edu/public. 2010.

[244] N. M. Law et al. "The Palomar Transient Factory: System Overview, Performance, and First Results". In: *Proc. Astron. Soc. Pacific* 121 (Dec. 2009), pp. 1395–1408. arXiv:0906.5350 [astro-ph.IM].

[245] SCUSS. *South Galactic Cap U-Band Sky Survey.* http://batc.bao.ac.cn/Uband. 2010.

[246] D. Lang. " " in preparation. 2016.

[247] R. H. Hardin, N. J. A. Sloane, and W. D. Smith. *Tables of Spherical Codes with Icosahedral Symmetry.* Florham Park: AT&T Shannon Lab., 2001.

Author Institutions

[1] 2137 Frederick Reines Hall, Irvine, CA 92697, USA

[2] Aix Marseille Univ, CNRS, LAM, 13388 Marseille, France

[3] Aix Marseille Univ, CNRS, OHP, 04870 Saint-Michel-l'Observatoire, France

[4] Aix Marseille Université, CNRS/IN2P3, CPPM UMR 7346, 13288, Marseille, France

[5] Alphabet Inc., 1650 Charleston Rd. Mountain View, CA 94043, USA

[6] AMNH, Department of Astrophysics, American Museum of Natural History, New York, NY 10024, USA

[7] APC, Université Paris Diderot-Paris 7, CNRS/IN2P3, CEA, Observatoire de Paris, 10, rue Alice Domon & Lonie Duquet, Paris, France

[8] Argonne National Laboratory, High-Energy Physics Division, 9700 S. Cass Avenue, Argonne, IL 60439, USA

[9] Astronomy Department, Yale University, P.O. Box 208101 New Haven, CT 06520-8101, USA

[10] Brookhaven National Laboratory, Upton NY 11973, USA

[11] Carreterra México-Toluca S/N, La Marquesa, Ocoyoacac, Edo. de México C.P. 52750, México

[12] CEA Saclay, IRFU F-91191 Gif-sur-Yvette, France

[13] Center for Cosmology and AstroParticle Physics, The Ohio State University, 191 West Woodruff Avenue, Columbus, OH 43210, USA

[14] Centre for Advanced Instrumentation, Department of Physics, Durham University, South Road, Durham, DH1 3LE, UK

[15] Centre for Astrophysics & Supercomputing, Swinburne University of Technology, P.O. Box 218, Hawthorn, VIC 3122, Australia

[16] Centre for Extragalactic Astronomy, Department of Physics, Durham University, South Road, Durham, DH1 3LE, UK

[17] Centre for Theoretical Cosmology, Department of Applied Mathematics and Theoretical Physics, Wilberforce Road, Cambridge CB3 0WA, UK

[18] Cerro Tololo Inter-American Observatory (CTIO), Colina El Pino s/n, Casilla 603, La Serena, Chile

[19] CIEMAT, Avenida Complutense 40, E-28040 Madrid, Spain

[20] Clippinger Laboratories, Room 333, Ohio University, Athens, OH 45701, USA

[21] Departamento de Física, Universidad de Guanajuato - DCI, C.P. 37150, Leon, Guanajuato, México

[22] Departamento de Física, Universidad de los Andes, Cra. 1 No. 18A-10, Edificio Ip, Bogotá, Colombia

[23] Department of Astronomy & Astrophysics, University of Toronto, 50 St. George Street, Toronto, ON, Canada M5S 3H4

[24] Department of Astronomy and Astrophysics, University of California, Santa Cruz, 1156 High Street, Santa Cruz, CA 95065, USA

[25] Department of Astronomy and Space Science, Sejong University, Seoul 143-747, Republic of Korea

[26] Department of Astronomy, The Ohio State University, 4055 McPherson Laboratory, 140 W 18th Avenue, Columbus, OH 43210, USA

[27] Department of Astronomy, University of California, Berkeley, CA 94720-3411, USA

[28] Department of Astronomy, University of Michigan, 1085 S. University Avenue, Ann Arbor, MI 48109-1107, USA

[29] Department of Astronomy, Yale University, Steinbach Hall, 52 Hillhouse Avenue, New Haven, CT 06511, USA

[30] Department of Physics & Astronomy and Pittsburgh Particle Physics, Astrophysics, and Cosmology Center (PITT PACC), University of Pittsburgh, Pittsburgh, PA 15260, USA

[31] Department of Physics & Astronomy, Ohio University, Athens, OH 45701, USA

[32] Department of Physics & Astronomy, University of Wyoming, 1000 E. University, Dept. 3905, Laramie, WY 82071, USA

[33] Department of Physics & Astronomy, University College London, Gower Street, London, WC1E 6BT, UK

[34] Department of Physics and Astronomy, Siena College, 515 Loudon Road, Loudonville, NY 12211, USA

[35] Department of Physics and Astronomy, The University of Utah, 115 South 1400 East, Salt Lake City, UT 84112, USA

[36] Department of Physics and Astronomy, University College London, 3rd Floor, 132 Hampstead Road, London, NW1 2PS, UK

[37] Department of Physics and Astronomy, University of California, 4129 Frederick Reines Hall, Irvine, CA 92697, USA

[38] Department of Physics and Center for Cosmology and Particle Physics, New York University, New York, NY 10003, USA

[39] Department of Physics and JINA Center for the Evolution of the Elements, University of Notre Dame, Notre Dame, IN 46556, USA

[40] Department of Physics and Michigan Center for Theoretical Physics, University of Michigan, Ann Arbor, MI 48109, USA

[41] Department of Physics, Carnegie Mellon University, 5000 Forbes Avenue, Pittsburgh, PA 15213, USA

[42] Department of Physics, Harvard University, 17 Oxford Street, Cambridge, MA 02138, USA

[43] Department of Physics, Kansas State University, 116 Cardwell Hall, Manhattan, KS 66506, USA

[44] Department of Physics, Southern Methodist University, 3215 Daniel Avenue, Dallas, TX 75275, USA

[45] Department of Physics, The Ohio State University, 191 West Woodruff Avenue, Columbus, OH 43210, USA

[46] Department of Physics, University of Arizona, 1118 E. Fourth Street, PO Box 210081, Tucson, AZ 85721, USA

[47] Department of Physics, University of California, Berkeley, 366 LeConte Hall MC 7300, Berkeley, CA 94720-7300, USA

[48] Department of Physics, University of Michigan, 450 Church St., Ann Arbor, MI 48109, USA

[49] Department of Physics, University of Warwick, Gibbet Hill Road, Coventry, CV4 7AL, UK

[50] Ecole Polytechnique Fédérale de Lausanne, CH-1015 Lausanne, Switzerland

[51] European Space Astronomy Centre (ESAC), 38205 Villanueva de la Cañada, Madrid, Spain

[52] Fermi National Accelerator Laboratory, PO Box 500, Batavia, IL 60510, USA

[53] Harvard-Smithsonian Center for Astrophysics, Harvard University, 60 Garden Street, Cambridge, MA 02138, USA

[54] HCTLab Research Group, Escuela Politecnica Superior, Universidad Autónoma de Madrid, C/Francisco Tomas y Valiente 11, 38049, Spain

[55] Institució Catalana de Recerca i Estudis Avançats (ICREA), Pg. de Lluís Companys 23, 08010 Barcelona, Spain

[56] Institut de Cìencies de l'Espai, IEEC-CSIC, Campus UAB, Carrer de Can Magrans s/n, 08913 Bellaterra, Barcelona, Spain

[57] Institut de Fisica dAltes Energies (IFAE), The Barcelona Institute of Science and Technology, Campus UAB, 08193 Bellaterra Barcelona, Spain

[58] Institute for Astronomy, ETH Zürich, Wolfgang-Pauli-Strasse 27, CH-8093 Zürich, Switzerland

[59] Institute for Astronomy, University of Edinburgh, Royal Observatory, Edinburgh EH9 3HJ, UK

[60] Institute for Computational Cosmology, Department of Physics, Durham University, South Road, Durham DH1 3LE, UK

[61] Institute of Astronomy, University of Cambridge, Madingley Road, Cambridge, CB3 0HA, UK

[62] Institute of Cosmology & Gravitation, University of Portsmouth, Dennis Sciama Building, Portsmouth PO1 3FX, UK

[63] Instituto de Astrofisica de Andalucía, Glorieta de la Astronomía, s/n, E-18008 Granada, Spain

[64] Instituto de Astrofísica de Canarias, C/ Va Láctea, s/n, 38205 San Cristóbal de La Laguna, Santa Cruz de Tenerife, Spain

[65] Instituto de Astronomia, Universidad Nacional Autónoma de México, Apartado Postal 70264, 04510 México D.F., México

[66] Instituto de Cìencias del Cosmoc, (ICCUB) Universidad de Barcelona (IEEC-UB), Martí i Franquès

1, E08028 Barcelona

[67] Instituto de Física Teórica (IFT) UAM/CSIC, Universidad Autónoma de Madrid, Cantoblanco, E-28049, Madrid, Spain

[68] Instituto de Fíisica, Universidad Nacional Autónoma de México, Cd. México C.P. 04510

[69] Kavli Institute for Astronomy and Astrophysics at Peking University, PKU, 5 Yiheyuan Road, Haidian District, Beijing 100871, P.R. China

[70] Kavli Institute for Cosmology, Cambridge, University of Cambridge, Madingley Road, Cambridge CB3 0HA, UK

[71] Kavli Institute for Particle Astrophysics and Cosmology and SLAC National Accelerator Laboratory, Menlo Park, CA 94305, USA

[72] Key Laboratory of Optical Astronomy, National Astronomical Observatories, Chinese Academy of Sciences, Beijing 100012, P.R. China

[73] Korea Astronomy and Space Science Institute, 776, Daedeokdae-ro, Yuseong-gu, Daejeon 34055, Republic of Korea

[74] Laboratoire dAstrophysique, Ecole Polytechnique Fédérale de Lausanne (EPFL), Observatoire de Sauverny, CH-1290 Versoix, Switzerland

[75] Laboratório Interinstitucional de e-Astronomia, Rua Gal. Jose Cristino 77, Rio de Janeiro, RJ 20921-400, Brazil

[76] Lawrence Berkeley National Laboratory, 1 Cyclotron Road, Berkeley, CA 94720, USA

[77] Lawrence Livermore National Laboratory, P.O. Box 808 L-211, Livermore, CA 94551, USA

[78] Ludwig-Maximilians University Munich, University Observatory, Scheinerstr. 1, 81679 Munich, Germany

[79] McWilliams Center for Cosmology, Carnegie Mellon University, 5000 Forbes Avenue, Pittsburgh, PA 15213, USA

[80] National Astronomical Observatories, Chinese Academy of Sciences, A20 Datun Rd. 100012, Beijing, P.R. China

[81] National Optical Astronomy Observatory, 950 N. Cherry Avenue, Tucson, AZ 85719, USA

[82] Observatorio Nacional, R. Gal. Jose Cristino 77, Rio de Janeiro, RJ 20921-400, Brazil

[83] Physics Department, Stanford University, Stanford, CA 93405, USA

[84] Physics Department, Yale University, P.O. Box 208120, New Haven, CT 06511, USA

[85] Physics Dept., Boston University, 590 Commonwealth Avenue, Boston, MA 02215, USA

[86] School of Mathematics and Physics, University of Queensland, 4101, Australia

[87] School of Physics, Korea Institute for Advanced Study, 85 Hoegiro, Dongdaemun-Gu, Seoul 02455, Republic of Korea

[88] Sorbonne Universités, UPMC Universit Paris 06, Université Paris-Diderot, CNRS-IN2P3 LPNHE 4 Place Jussieu, F-75252, Paris Cedex 05, France

[89] Space Sciences Laboratory, University of California, Berkeley, 7 Gauss Way, Berkeley, CA 94720, USA

[90] Steward Observatory, University of Arizona, 933 N. Cherry Avenue, Tucson, AZ 85721, USA

[91] SUPA, School of Physics and Astronomy, University of St Andrews, St Andrews, KY16 9SS, UK

[92] University of California Observatories, 1156 High Street, Sana Cruz, CA 95065, USA

[93] University of Science and Technology, Daejeon 34113, Republic of Korea